Coordination Chemistry Reviews 493 (2023) 215257

Contents lists available at ScienceDirect

Coordination Chemistry Reviews

journal homepage: www.elsevier.com/locate/ccr

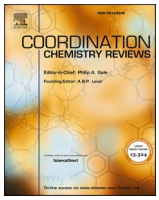

Review

Metal organic framework composites for reduction of CO_2

Kuan-Guan Liu [a,*], Fahime Bigdeli [b], Akram Panjehpour [b], Afsanehsadat Larimi [c], Ali Morsali [b,*], Amarajothi Dhakshinamoorthy [d,e,*], Hermenegildo Garcia [f,*]

[a] School of Materials and New Energy, Ningxia Key Laboratory of Photovoltaic Materials, Ningxia University, Yin-Chuan 750021, PR China
[b] Department of Chemistry, Faculty of Sciences, Tarbiat Modares University, P.O. Box 14115-175, Tehran, Iran
[c] Department of Chemical and ProcessEngineering, Niroo ResearchInstitute, Tehran, Iran
[d] Departamento de Química, Universitat Politècnica de València, Camino de Vera, s/n, Valencia 46022, Spain
[e] School of Chemistry, Madurai Kamaraj University, Madurai, Tamil Nadu 625021, India
[f] Instituto Universitario de Tecnología Química, Consejo Superior de Investigaciones Científicas.-Universitat Politecnica de Valencia, Universitat Politecnica de Valencia, Av. De los Naranjos s/n, Valencia 46022, Spain

ARTICLE INFO

Keywords:
Heterogeneous catalysis
CO_2 utilization, metal-organic framework composites
Electrocatalysis
Photocatalysis
CO_2 hydrogenation

ABSTRACT

Global warming due to greenhouse gases is a major current environmental threat. In today's world those applicable technologies which convert CO_2 into valuable and environmentally friendly fuels and chemicals are of great importance. Thanks to functional sites or guests embedded in the structure, metal organic frameworks (MOFs) show a superb potential for such a conversion that is even further enhanced in MOF composites. The present review discusses the use of MOF composites, with an emphasis on their constituent components, as catalysts for CO_2 reduction, converting it into various value-added and environmentally friendly chemicals such as saturated and unsaturated hydrocarbons, carboxylic acids and carboxylates, and carbon monoxide. The present review covers four major approaches for CO_2 reduction, including electroreduction, photoreduction, photoelectroreduction, and hydrogenation. All reports on the design and development of appropriate MOF composites to be used in the above-mentioned CO_2 reductions have been considered. Finally, the future outlook on the use of MOF composites in CO_2 reduction is provided, giving some ideas for further design highly efficient MOF composites capable of converting CO_2 to value-added products.

1. Introduction

CO_2 gas is generated in nature in several ways including volcanic gases, spontaneous combustion of organic compounds, respiration of aerobic organisms, as well as fermentation and cellular respiration of micro-organisms. In addition to the above-mentioned natural ways, CO_2 is also produced through different human activities on the planet, for example burning wood and fossil fuels.

The concentration of atmospheric CO_2 increases annually due to the massive human combustion of fossil fuels to generate energy. This appears to be an ascending trend which certainly poses a serious threat for our planet. Therefore, it is necessary to implement measures to minimize the CO_2 emissions to the atmosphere by converting it into environmentally friendly and valuable materials. Chemical reduction of CO_2 is one of the approaches used for this purpose. Chemical reduction of CO_2 can be performed using various enerfy types for activation of the reaction, resulting in electrochemical reduction [1], photochemical reduction [2], photoelectrochemical reduction [3], and hydrogenation [4], the process yielding valuable products such as alcohols, carboxylic acids, hydrocarbons, etc. It is noteworthy that electrochemical, photochemical and photoelectrochemical methods for reduction of CO_2 have attracted special attention because of their usage of renewable energy in driving the reaction. As CO_2 is a thermodynamically stable molecule, such reactions require an energy of 805 KJ/mol to break the double bond between carbon and oxygen atoms in CO_2 [5]. Therefore, a catalyst reducing the energy barrier is needed. Various catalysts have been applied for this purpose including carbon materials, metal organic frameworks (MOFs), metal oxides and metal nanoparticles (NPs), etc. However, MOF composites have drawn the most attention due to their unique structural features of MOF including synthetic tailorability, large accessible surface area, high porosity, and reaction to light and heat and their compatibility with many other active components [6-15].

* Corresponding authors.
E-mail addresses: liukuanguan@nxu.edu.cn (K.-G. Liu), morsali_a@modares.ac.ir (A. Morsali), admguru@gmail.com (A. Dhakshinamoorthy), hgarcia@qim.upv.es (H. Garcia).

https://doi.org/10.1016/j.ccr.2023.215257
Received 29 January 2023; Accepted 20 May 2023
Available online 22 June 2023

Although there are several reviews published on the use of MOFs as catalysts in the above-mentioned processes for CO_2 reduction,[16-18] all of them mostly focus exclusively on MOFs to achieve the catalytic activity. In comparison, the present review describes the activity of MOF composites to shedding light on how the constituting MOF composite components contribute to the CO_2 reduction reaction, providing some concepts for the logical designing of MOF composites for catalytic purposes.

Thus, the present review emphasizes the properties of MOF composites acting as catalysts in reduction of CO_2 through four different methods (electroreduction, photoreduction, photoelectroreduction, and hydrogenation), placing particular emphasis on the constituting components of MOFs and describing the effect of each component on several variables within the above-mentioned methods. Some of these variables are: absorption of visible light, charge separation, absorption and activation of CO_2 for photoreduction, conductivity for electroreduction, etc.

In these composites, MOFs play and important role contributing to the overall catalytic activirty. As it is general in heterogeneous catalysis, all these processes benefit from materials having very large surface area accessible to substrates and reagents. In this regard, MOFs are currently among the solids with largest specific surface area, easily over 1000 m^2/g and with some reports indicating values well over 3000 m^2/g, which are nowadays the record for any material in specific surface area. In addition to surface area, another positive requirement in MOFs is the presence of a large density of active sites. Given the composition of MOFs and the general catalytic activity of transition metal ions, most frequently over 30% of weight in the MOF, the density of actoive sites in MOFs is frequently much higher than in other alternative catalysts. In addition, it is not uncommon that the secondary building units constituted by metal ion clusters have exchangeable coordination positions not compromised in the construction of lattice that are available for interaction with substrates. Worthnoting also is the large vaiety of transition and main metal ions that can be used for the preparation of MOFs. In catalysis, these metal ions can participate in electron transfer processes taking place in electrochemical and photoelectrochemical reductions, but also in the most common photochemical mechanisms involving photoinduced charge separation. Besides redox reactions, the activity of metal ions as Lewis acids is important in conventional thermal catalysis and in this way, MOFs offer a wide range of possibilities regarding the type of energy (electrical fields, photons or heat) that can be used to promote the CO_2 reduction. In a certain way, MOFs can be envisioned as an ordered array of transition metal complexes held in the positions of an open porous framework. Immobilization of the metal complexes is beneficial for their stability in catalysis since the most common deactivation mechanisms of these molecular complexes consists in their dimerization and aggregation, becoming insoluble and inactive during the reactio. The high empty volume and large porosity of MOFs is also a beneficial factor compared to other possible porous catalysts, such as zeolites or structured aluminosilicates, since MOFs present much larger pore volumes.

The present review also presents various discussions on the product (s) obtained from reduction reactions according to the specified factors in the mentioned four approaches, for example turnover frequency (TOF), turnover number (TON), and the ratio of net absorption of CO_2 to the rate of product evolution (AQF) for photoreduction; current density, Faradaic efficiency and overpotential for electroreduction; etc. Regarding product analysis, one remark that is extremely important is how to ensure that the products derived from CO_2 reduction and not from MOF ligand decomposition or any other organic component or impurity present in the system. This issue is particularly relevant since in most of the cases, TONs are low and the amount of product that is formed is commensurate with the catalyst weight. The safest way to address the product origin consists in performing adequate ^{13}C isotopic labelling experiments in which the feed used in the test reaction is $^{13}CO_2$ and the products are analyzed by mass spectrometry or ^{1}H NMR spectroscopy to determine their isotopic composition. These isotopic experiments have to be performed rigorously to be convincing. Thus, in the case of mass spectrometry, it is necessary or very convenient to previously separate the products by gas chromatography. Otherwise, some framgments from $^{13}CO_2$, particularly ^{13}CO or from H_2O (*m/z*: 18) can be confused with ^{13}CO or $^{13}CH_4$ as products. In the case of ^{1}H NMR spectroscopy, the ^{13}C-H coupling constant of about 200 Hz should make the product signal split into doublets, while the peak corresponding to unlabelled product should be absent. A comment in this regard is that there are in the literature several examples in which these isotopic labelling experiments either have not been performed or have been performed for mixtures resulting in unconclusive support data.

Most of the MOFs do not have sufficient stability in some CO_2 reduction reaction requiring strong acidity or basicity, aqueous environment, and high electrochemical potential [16]. However, there are examples like ZIF MOFs exhibiting high structural stability in aqueous media under harsh coditions [2]. MOFs often provide thermal and optical stability in composites by supramolecular interactions with the framework [17]. On the other hand, with the rational design of MOFs, structures with high stability can be prepared, for example, by having metal nodes with high positive charge or using hydrophobic alkyl groups on organic linkers, the resulting MOFs exhibiting water-stable framework [18]. To improve physico-chemical properties of MOFs, they can be coupled in a controlled way with suitable materials such as carbon substrates, metal nanoparticles (NPs) and polymers in composite structures in such a way that it leads to the production of frameworks with high stability and many active sites for reduction of CO_2 [2,7,16].

In addition to their structural identification, composite characterization methods can help in understanding the reaction mechanism and subsequently in the design of subsequent framework generations with better performance. Here, some of the most important characterization methods of composites will be presented. For characterization of the metal distribution methods such as EDS, X-ray photoelectron spectroscopy (XPS) and inductively coupled plasma-optical emission spectroscopy (ICP-OES) are applied. Cyclic voltammetric (CV) is used to study the oxidation-reduction properties of redox active species [19]. ATR and DRIFT spectroscopy can be used to investigate the interaction between CO_2 and MOF composites. By comparing the spectra before and after the interaction with CO_2 and the position and appearance of the peaks, the number of interaction sites can be determined [20]. SEM is used to study the structural arrangement of the composite and size and morphology of particles, and atomic force microscope (AFM) is used to measure the thickness of the layers [21]. N_2 adsorption and desorption isotherm plot show the distribution and nature of pores, which is important for mass transfer and distribution of substrates in the composite structure. Chemical stability of the structures can be investigated by powder X-ray diffraction (PXRD) measurements [22].

We have collected all attempts made to design and develop the appropriate MOF composites and their use in the above-commented CO_2 reduction methods. Herein, a comprehensive review aimed at summarizing the recent progress in the applications of MOF-based composites for CO_2 reduction covering various methods, like electroreduction, photoreduction, photoelectroreduction, and hydrogenation, is provided. Further, the advantages and disadvantages of MOFs as well as the performance of each component in the composite in CO_2 reduction are also presented. Finally, the last section provides conclusions on the current state of the art and the future outlook of using MOF composites in CO_2 reduction have been provided.

2. Reduction of CO_2 by MOF composites

2.1. Electroreduction of CO_2 by MOF composites

MOFs and some special species can be merged to form certain MOF composites which are appropriate to play the role of catalysts in electrochemical CO_2 reduction. Electrochemical CO_2 reduction offers the possibility to use directly renewable, green electricity to activate the

process. The electrochemical reduction of CO_2 is performed within an electrochemical cell comprising two electrodes (anode and cathode), a divider and an electrolyte. The electrolyte is a water solution with a high electrical conductivity. The current consumed in the cell is, in part, the result of oxidation in anode and reduction in cathode. When such reactions are carried out, the electron density in anode makes the electron flow in the wire traveling toward the cathode. Two compartments of anode and cathode are separated from each other by an ion-conductive membrane to prevent the products of CO_2 reduction from re-oxidation. Fig. 1 schematically illustrates an electrochemical cell used for electroreduction of CO_2.

Herein, all endeavors made to design and apply MOF composites to serve as catalysts in CO_2 reduction reaction have been collected and presented. Electrocatalytic CO_2 reduction reaction comprises various pathways leading to various products, such as carbon monoxide, formic acid, formaldehyde, methanol, methane, ethylene, ethanol and etc. Among the products listed above, CO appears to be the major product in the electrolyte based on water solvent.

In the rate determining step, first the electron is transferred to $*CO_2$ which has been absorbed on surface and consequently the $*CO_2^{\bullet-}$ anion radical is generated. The atom which binds to the surface of electrode specifies the subsequent step. As illustrated in Fig. 2, when the oxygen atom of $*CO_2^{\bullet-}$ binds to the electrode surface, the carbon atom forms *OCHO through protonization. Then, the next electron and proton transfer gives rise to the generation of formic acid or formate as product. On the other hand, when the carbon atom of $*CO_2^{\bullet-}$ binds to the surface of the electrode, (a) CO; (b) CH_4, CH_3OH; (c) C_2H_4, C_2H_5OH can be produced (Fig. 3). As shown in Fig. 4, the formate product is formed when CO_2 is inserted into a metal-H bond.

Current density, overpotential, and Faradaic efficiency are three factors required to appraise the activity of an electrocatalyst in an electrochemical reaction.

The current density is defined as electrical current normalized on the surface of an electrocatalyst, represented by j with SI unit of ampere per square meter (A/m^2).

Overpotential is the difference between a theoretically or thermodynamically determined reduction potential and the real potential at which the redox is experimentally observed, represented by η with SI unit of volt(v).

The selectivity of electrochemical reaction products is defined by Equation (1) exhibiting Faradaic efficiency (FE):

$$Faradaic\ Efficiency = enF/Q \quad (1)$$

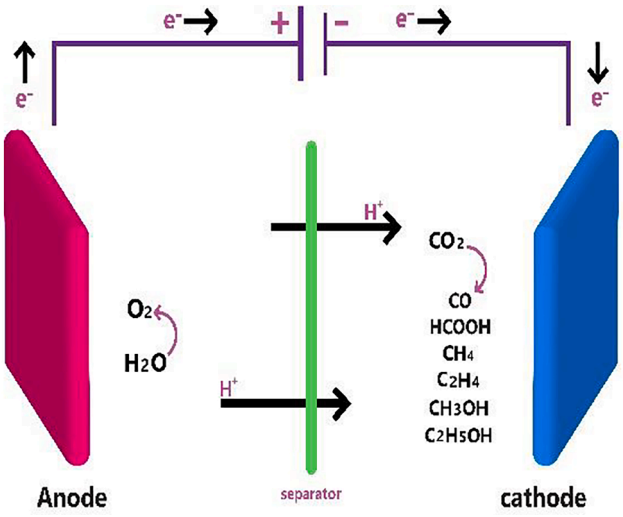

Fig. 1. The structure of an electrochemical cell used for electroreduction of CO_2.

Where F is Faraday constant representing the electric charges carried by one mole, or Avogadro constant multiplied by elementary charge (e) which is usually taken to be 96,485C mol^{-1},

n denotes the number of electrons transferred to form the associated product,

Q is the total charge obtained during the reaction, and e represents the number of electrons transmitted.

Table 1 shows that the main product of electrochemical reaction with MOF composites as electrode is CO, and in the literature often $KHCO_3$ electrolyte has been used. Also, Table 1 compiles the electrochemical parameters related to various MOF composites including the applied potential and faradaic efficiency.

2.1.1. MOF-Supported metal NPs

C1 products such as CO, HCOOH and CH_4 are the most products in the CO_2 electroreduction process by MOFs, in their pristine form. This probably results from the distance between isolated active sites in the framework, which prevents efficient C-C coupling, whereas C-C bond formation is more likely if the active sites are in close proximity. Incorporation of metal nanostructures into the framework of MOFs can be an effective way to impart desired functionalities (such as conductivity, photoactivity, and catalytic activity) to MOFs [44].

Metallic NPs are known as catalysts for CO_2 reduction reaction; however the agglomeration of these particles reduces their catalytic properties. Thanks to large surface area as well as notable porosity, MOFs can prevent agglomeration and improve catalytic properties of NPs encapsulated within MOFs. Ag is one of the most widely investigated metals for the electrochemical CO_2 reduction, affording CO as the main product, due to the weak CO adsorption on the silver surface. Both the electroreduction of CO_2 to CO and the competitive H_2 reaction occur simultaneously on Ag NPs. As an example of Ag-MOF composites, Jiang et al.[45] investigated Ag/ZIF-7 MOF composite as catalyst for CO_2 electroreduction. They found that the new MOF composite exhibits greater CO faradaic efficiency and current density (80.5% and 26.2 mA cm^{-2} at 1.2 V vs) compared to base materials. The improved performance is assignable both to the large accessible surface and the synergistic effect between Ag NPs and ZIF-7 MOF. Other metal NPs embedded within MOF pores behave similarly. Thus, Zhao and coworkers constructed Pt/Au@Pd@CoMOF from CoMOF= $\{Co_2(oba)_4(3\text{-bpdh})_2\}$ $4H_2O$ [oba = 4,4′ -oxybis(benzoic acid); 3-bpdh: N,N'-bis-(1-pyridine-3-yl-ethylidene)-hydrazine] at the center of which Au@Pd core-shell was encapsulated and on the surface Pt NPs were dispersed [44]. This MOF composite improves CO_2 reduction toward the formation of CO and such improvement is ascribed to the synergism of Au@Pd and Pt NPs as well as the role of CoMOF immobilizing these NPs in a structured manner.

To carry out the CO_2RR process, a tandem pathway intervening different active sites can create a suitable substrate to produce $>2e^-$ products. The accommodated metals within the MOF structure can effectively facilitate the charge distribution and conduction path to progress the CO_2RR reaction [21]. In 2022, Deng et al.[46] constructed AuNN@PCN-222(Cu) [AuNN = Au nanoneedles] containing metalloporphyrin Cu centers and AuNN impregnated therein. When utilized as catalyst in electrochemical CO_2 reduction, AuNN@PCN-222(Cu) shows higher efficiency and selectivity than PCN-222(Cu) and AuNP@PCN-222(Cu) in producing ethylene (FE 52.5 %). This high selectivity and efficiency of AuNN@PCN-222(Cu) MOF composite in ethylene production arises from a tandem mechanism through which the CO generated from AuNNs is combined with *CHO on metalloporphyrin. The charge transfer from the ligand to the metal, due to the proper LUMO position in Cu^{2+}, can reduce Cu^{2+} ions. Therefore, copper centers in PCN-222(Cu) can easily accept electrons and dissociate from the porphyrin ring, producing particles and clusters. In contrast, by supporting Au, the frontier orbitals of the composite move towards Au and lead to charge conduction from Au to metalloporphyrin centers to drive proton-coupled electron transfer process for hydrogenation. Such ability of electron transfer by Au protects the catalytic centers and leads to

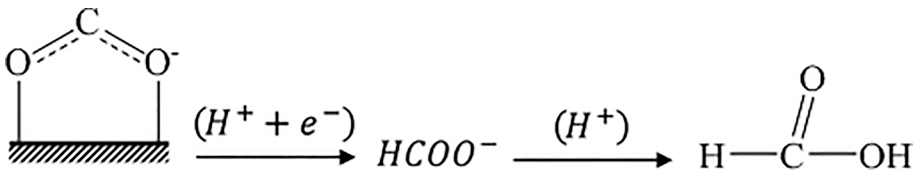

Fig. 2. Paths for producing formate and formic acid from CO_2 electroreduction reaction.

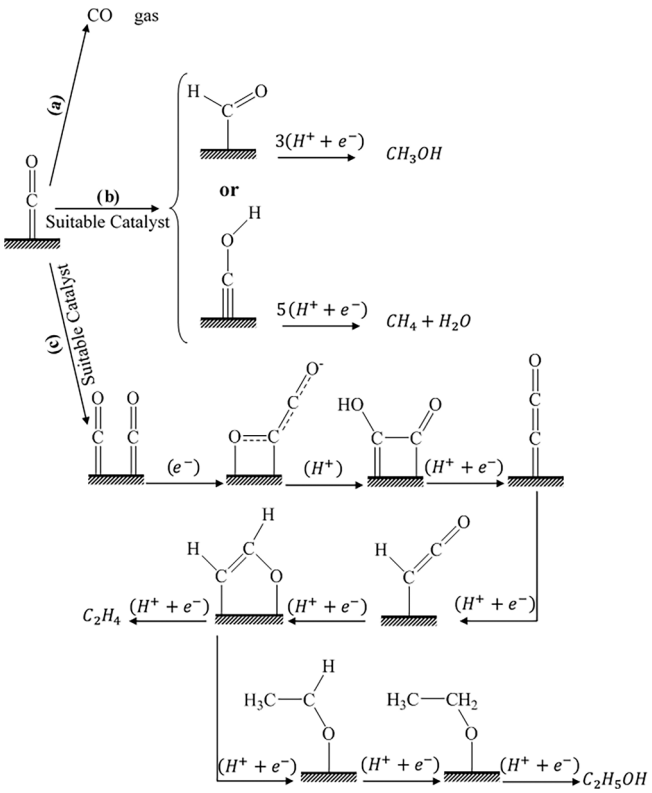

Fig. 3. Paths for producing (a) CO, (b) CH_4, CH_3OH, and (c) ethylene and ethanol from CO_2 electroreduction reaction.

greater stability of the catalyst.

Sargent et al. used the advantages of the tandem process in MOFs for the electrocatalytic CO_2 reduction. That catalysis is carried out in the framework of MOF in such a way that the product of one catalytic center becomes a reactant in another catalytic center. For example, the product of CO_2 reduction at the surface of the first catalytic center is CO, and then other valuable products are produced in the neighbor centers. MOF/electrocatalyst hybrids provide the substrate for this process and MOF pores are suitable reaction cavities for performing electrocatalytic reactions. In this way, these authors constructed MOF/AuNME composites by growing MOF thin films on Au nanostructured microelectrodes (AuNMEs) [47]. Afterwards, the resulting system was utilized as electrocatalyst in CO_2 electroreduction. The results indicated that MOF thin films suppress CO formation, resulting instead in methane and ethylene products.

According to reports, in the electrochemical conversion of CO_2, copper can break the C-O bond in CO_2 and convert CO into species such as hydrocarbons and alcohols. Based on this finding, in 2019, Albo et al. [48] applied Cu/Bi-based MOF (HKUST-1/CAU-17) supported on gas diffusion electrodes in a filter-press electrochemical cell for reduction of CO_2. The results revealed the desirable production of methyl alcohol and ethyl alcohol. The highest rate and FE (faradaic efficiencies) for CH_3OH and C_2H_5OH were respectively 29.7 $\mu molm^{-2}s^{-1}$, FE: 8.6% and 48.8 $\mu molm^{-2}s^{-1}$, FE: 28.3% at j:20 $mAcm^{-2}$. This favorable result is ascribed to the synergistic effect between Cu and bismuth MOF associated with an excellent interplay between the active sites and reaction intermediates which finally leads to methanol formation and C-C coupling reaction toward ethanol.

Another example of MOF composites that support metal NPs for their improved electrocatalytic performance was reported by Hupp et al.[19] They implanted Cu NPs in zirconium MOF (UN-1000). The resulting MOF composite showed the catalytic performance in two phases (liquid & gas): CO was produced in gas phase and formate was produced as the main product in the liquid phase (with production rate of 4 $\mu mol/cm^{-1}$ at potential 0.5 V vs. RHE (reversible hydrogen electrode). The improvement observed in photocatalytic properties of this MOF composite may be ascribed to synergistic effect of large surface area and NPs.

2.1.2. MOFs on conductive supports

One of the weak points of MOFs is their low electrical conductivity which restricts their electrochemical application. Incorporating MOFs on conductive supports such as graphene oxide, carbon black and other conductive materials forms some MOF composites whose catalytic characteristics have been improved, thanks to their enhanced electrical conductivity. One of these conductive materials is the carbon nanotubes family. Carbon nanotubes, when completely integrated into a composite structure, demonstrate high conductivity. Therefore, by combining such materials with some MOFs which act as catalysts in electrochemical reactions one may achieve electrocatalysts with more enhanced performance. This higher efficiency arises from the improved electrical conductivity of resulting MOF composite compared to the original MOF. For example, Dong et al. [36] constructed a MOF composite, [PCN-222(Fe)/CNTs] from PCN-222(Fe) and carbon nanotubes (CNTs) by solvothermal method in which iron porphyrin-centere PCN-222(Fe) is loaded onto CNTs. The resulting MOF composite with best ratio (m(Fe-TCPP):m(CNTs) = 1:30) shows excellent performance in electroreduction of CO_2 (FE is 90% for CO, overpotential of −0.6 V and a TOF of 448.76 h^{-1}). This boosted performance is attributed to the presence of CNT as conductive support in the structure of the MOF composite which in turn boosts the electrical conductivity.

Copper compounds as heterogeneous catalysts may be ideal options for eCO_2RR because they can produce hydrocarbon products. Grace

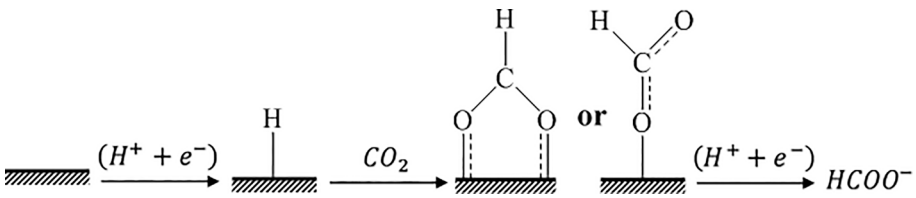

Fig. 4. Path for producing formate by inserting CO_2 into a metal− H bond.

Table 1
Various MOF composites as electrocatalysts reported for CO_2 reduction.

MOF composite	Electrolyte, Potential[a)]	Main carbon products	Faradaic efficiency (%)	Ref.
Ag_2O/layered ZIF	0.25 M K_2SO_4,−1.2 V	CO	80.5	[23]
Cu_2O@Cu-MOF	0.1 M $KHCO_3$, −1.71 V	CH_4, C_2H_4	63.2 (CH_4); 16.2 (C_2H_4)	[24]
Cu-SIM NU-1000	0.1 M $NaClO_4$, −0.82 V	$HCOO^-$	28	[25]
MOF@Au NME	0.1 M $KHCO_3$, −0.5 V	CO	18 ± 2	[26]
Ag@Al-PMOF	0.1 M $KHCO_3$, −1.1 V	CO	55.8 ± 2.8	[27]
$CoCp_2$@MOF-545-Co	0.5 M $KHCO_3$, −0.7 V	CO	97	[28]
HKUST-1/CAU-17	0.5 M $KHCO_3$, −0.21 V	CH_3OH, C_2H_5OH	8.6(CH_3OH), 28.3(C_2H_5OH)	[29]
AuNN@PCN-222(Cu)	0.1 M $KHCO_3$, −1.2 V	C_2H_4	52.5	[30]
PCN-222(Fe)/CNTs	0.1 M $KHCO_3$, −0.6 V	CO	90	[31]
Cu-MOF/GO	0.1 M TBAB/DMF, −0.6 V	HCOOH	58	[32]
Re-SURMOF/FTO	0.1 M TBAH/MeCN/5%TFE, −1.6 V	CO	98–93	[33]
Cu_2FCuTCPP/FTO	0.5 M $EMIMBF_4$/1MCH_3CN, −1.55V)[b)]	$HCOO^-$	68.40	[34]
Cu_2FCuTCPP/FTO	0.5 M $EMIMBF_4$/1MCH_3CN, (-1.4 to −1.65)V [b)]	CH_3COO^-	85, 2–38, 8	[34]
$Al_2(OH)_2$TCPP-Co	0.5 M K_2CO_3, −2V[b)]	CO	76	[35]
PCN-222(Cu)/C	0.5 M $KHCO_3$,(−0.87 to −1.17)V	HCOOH	44.30	[36]
PCN-224(Cu)/C	0.5 M $KHCO_3$, (-0.87 to −1.17)V	HCOOH	34.10	[36]
Co-PMOF	0.5 M $KHCO_3$, −0.8 V	CO	99	[37]
Fe-MOF-525	1 M $TBAPF_6$/DMF, −2 V	CO	50	[38]
2Bn-Cu@UiO-67	1 M KOH, −1.5 V	CH_4	81	[39]
Bi_2O_3/Zr-TATB MOL	0.5 M $KHCO_3$, (−0.87 to −1.17)V	$HCOO^-$	85	[40]
MOF-NS-Co	0.1 M $KHCO_3$, −0.6 V	CO	98.7	[41]
CuO/Cu-MOF	0.1 M $KHCO_3$, −1.1 V	C_2H_4	50	[42]
H-POM@PCN222(Co)	0.5 M $KHCO_3$, −0.8 V	CO	96.20	[43]

a) Versus RHE, b) Versus Ag/AgCl.

et al.[49] constructed Cu-MOF/GO (Cu−benzene-1,3,5-tricarboxylic acid) where GO is graphene oxide. The resulting MOF composite was applied in electroreduction of CO_2 as catalyst. This MOF composite exhibited excellent performance in electroreduction of CO_2 toward formic acid in comparison with Cu-MOF when utilized alone. Thanks to the presence of GO as conductive support, FE is 58% for Cu-MOF/GO, while it was 38% for Cu-MOF.

In another study, Ye and et al. applied fluorine doped tin oxide (FTO) as a conductive support [50]. Facile charge transfer created by well-oriented layered sheets of the resulting MOF yielded the FE of (93–98)% for CO production.

Wu et al. [51] applied Cu_2FCuTCPP nanosheet on FTO as a cathode. This system shows good selectivity and efficiency for CO_2RR which is attributed to the use of FTO as conductive support. The products of reduction reaction are formate (Faradaic efficiency of 68.4% at a potential of −1.55 V versus standard potential of Ag/Ag^+) and acetate (FE of 38.8% to 85.2% at a range of −1.40 V to −1.65 V versus standard potential of Ag/Ag^+).

Moreover, Yang and coworkers constructed an aluminum porphyrin MOF-55 containing Co-porphyrin as an active site by depositing an aluminum oxide layer (as a conductive support) on the Co-MOF composite for CO_2 reduction to CO [52]. The optimized thickness of catalyst (5 nm) provides the CO product with a FE of 76% for 7 h and a TON of 1400. So, this MOF composite exhibits a higher efficiency in electroreduction of CO_2 to CO in comparison to base materials, which is attributed to high conductivity of the oxide layer.

In 2020, Liu et al.[53] prepared two types of PCN-222(Cu)/C and PCN-224(Cu)/C MOF composites by assembling PCN-222(Cu) and PCN-224(Cu) as conductive support and then compared them in terms of their catalytic activity in electrochemical CO_2 reduction. They utilized the resulting MOF composites as electrode in electrochemical CO_2 reduction reaction and found that each new MOF composite shows a higher efficiency and selectivity within a particular voltage range. Within the voltage interval of 0.7–0.9 v, PCN-222(Cu)/C because of its higher Brunauer-Emmett-Teller surface area, CO_2 absorption, and large diameter of pores exhibits higher activity and selectivity (over potential = 450 mV, FE_{HCOOH} = 44.3%, current density = 3.2 mA cm^{-2}) than PCN-224(Cu)/C (over potential = 450 mV, FE_{HCOOH} = 34.1%, current density = 2.4 mA cm^{-2}) to produce HCOOH. On the other hand, PCN-224 (Cu)/C shows higher performance than PCN-222(Cu)/C within the interval of −0.4—-0.6 v (vs.RHE) thanks to the enhanced heat of adsorption, Qst, and a big attraction for CO_2 molecule, boosting the confinement of CO_2 in the active sites.

2.1.3. MOF-supported active catalysts

As mentioned before, since the reduction of CO_2 is a very energetic and challenging process, the presence of a catalyst is necessary to facilitate the progress of the reaction. The incorporation of molecular catalyst in MOF holes appears to be a useful technique to redesign MOF composites for obtaining an improved catalytic activity, because in this way the highly porous MOFs offer larger surface area required for the high distribution of active sites.

As nanocrystals are powerful catalysts for chemical reactions, hybridizing nanocrystal catalysts with appropriate MOFs can improve their catalytic properties. For example, Buonsanti and coworkers constructed Ag@Al-PMOF from silver nanocrystals (NCs) and Al-PMOF ([$Al_2(OH)_2$(TCPP)], TCPP = tetrakis(4-carboxyphenyl)porphyrin) [27]. Ag@Al-PMOF is applied as electrocatalyst for CO_2 reduction reaction because silver NCs maintain their electrical association with the conductive substrate in spite of being implanted in the MOF composite. Ag@Al-PMOF enhances CO_2 electroreduction reaction but suppresses HER reaction in comparison with the case when Ag NCs is used individually. This enhanced activity is attributed to electronic effects and partial mass transfer caused by MOF composite. Al-PMOF matrix increases the morphological stability of Ag NCs during the reduction reaction. This increased stability was confirmed by XPS, SEM, TEM and ICP-OES (inductively coupled plasma–optical emission spectrometry) analyses. In contrast, the bare Ag NCs form dendrites during the reduction process of CO_2.

Similarly, Lan and coworkers designed a new group of so-called polyoxometalate metalloporphyrin organic frameworks (m-PMOFs) where m: Co,Ni,Fe,Zn [54], and compared the activities of the resulting MOF composites with each other. Among them, Co-PMOF shows the highest Faradaic efficiency equaling 99% and a TOF of 1656 h^{-1} for CO production as well as a good catalysis stability (>36 h). DFT calculations indicate that the presence of cobalt in m-PMOF reduces the energy required for creating *CO and *COOH intermediates compared to the other three metals (Ni,Fe,Zn) and improves CO_2RR, consequently. MOFs with a two-dimensional monolayer structure and ultrathin nature (metal organic layer (MOLs)) can be suitable for electrocatalysis because it leads to improved conductivity so that the distances of electrons and ions pass becomes very short.

It is also possible to control the environment around the catalytic center by modifying the functional groups to improve the catalytic performance. Given these benefits and structural advantages of MOLs, Wang and coworkers [55] synthesized a catalytic pocket from cobalt protoporphyrin (CoPP) and catalytic sites of pyridine/pyridinium (py/pyH^+) on metal organic layer as electrocatalyst in order to investigate the CO_2 electroreduction reaction. When pyridine is removed from this catalytic pocket a selectivity of 2.7 for CO/H_2 is observed, while the selectivity reaches 11.8 in the presence of pyridine. This MOF shows enhanced electrocatalytic properties upon adding pyridine.

It has been found that systems containing molecular catalysts in homogeneous solution have several advantages that include spectroscopic identification of reaction intermediates is relatively easy and the details of the mechanism of the catalytic process can be determined, and the modification of the catalyst structure can be achieved according to the goals of the reaction process. However, homogeneous catalysts are electrically activated only at or near the surface of a conductive electrode. While heterogeneous electrocatalysis does not have these disadvantages. Therefore, the use of heterogeneous catalysts prevents the aggregation of catalytic species and the chemical environment around the catalyst center becomes suitable for the catalytic reaction, and it is possible to use solvents even with poor solubility for the catalyst. In 2015, Hod et al. [38] used heterogeneous catalysts (Fe-MOF-525) with a high surface concentration for electroreduction of CO_2. They merged Fe-porphyrin into MOF-525 which caused it to earn high effective area for electrochemically catalytic sites (10^{15} sites cm^{-2}), leading to the production of CO with a FE of 50%.

In another study, Chen and Lan et al.[28] constructed MCp_2@MOF-545-Co composites (Cp: cyclopentyl) through encapsulating metallocene [MCp_2 (M = Fe, Co, Ni)] into the pores of metalloporphyrin-based MOF-545-Co by using vapor deposition method. Among these composites, $CoCp_2$@MOF-545-Co converted CO_2 to CO with a high selectivity and a FE for Co equaling 97% at − 0.7 V versus RHE. The high performances might be ascribed to the powerful binding interaction between metallocene and metalloporphyrin that can largely reduce the adsorption energy of CO_2 as revealed by DFT calculations.

The selectivity of CO_2 electrocatalytic product to hydrocarbon valuable products is very important. Catalysts based on copper compounds, catalysts with a high reaction rate, are one of the most promising candidates to produce hydrocarbons, especially CH_4 and C_2H_4. Cu_2O is one of the widely used catalysts. Yu et al.[56] constructed Cu_2O@Cu-MOF and utilized it as catalyst in electrochemical CO_2 reduction reaction, finally leading to the production of CH_4 and C_2H_4 with a Faradic efficiency of 79.4%. The enhanced efficiency is attributed to high CO_2 adsorption and synergistic effects between Cu-MOF and Cu_2O.

Similarly, Silva et al.[20] constructed Cu/Cu_2O-Cu(BDC) (BDC: 1,4,-benzenedicarboxylic acid) electrode and applied it as catalyst in electrochemical CO_2 reduction reaction. In their work, the reduction of CO_2 to CH_3OH was observed to be approximately 20 times as much as when Cu/Cu_2O is used as electrocatalyst in the absence of MOF. This enhancement is attributed to high porous surface area provided by the MOF component.

An example of a copper-based catalyst was provided by Wang et al. [57] They constructed (2Bn-Cu@UiO-67) MOF composite with N-heterocyclic carbene-ligated Cu SAS (single atom site) as the active sites, and applied it in electrochemical CO_2 reduction reaction. The resulting system shows an excellent efficiency in reduction of CO_2 to methane, yielding a significant FE of 81% at −1.5 V vs.RHE with a j = of 420 mA cm^{-2}. This outstanding efficiency is attributed to the porousness of catalyst which facilitates the diffusion of CO_2 to 2-Bn-Cu and consequently increases the accessibility of catalytic centers, as well as the sigma donation of N-heterocyclic carbene that boosts the electron density of copper single atoms on the surface and improves the adsorption of CHO* intermediates. This enhanced adsorption in turn helps to improve the CO_2 reduction reaction toward methane.

Using MOLs instead of 3D MOFs can be a good method for optimal electrocatalytic activity in MOFs because they have fully accessible active surfaces, while maintaining structural flexibility. In 2021, Liu et al.[22] constructed Bi_2O_3/Zr-TATB MOL by growing Bi_2O_3 on Zr-TATB MOL [TATB: 4,4′,4′′-s-triazine-2,4,6-triyl-tribenzoate] and utilized the resulting composite as catalyst in electrochemical CO_2 reduction reaction. The results indicated its high activity for producing formate from CO_2 reduction (a FE of over 85% with a broad potential ranging −0.87 to −1.17v). This enhanced activity is attributed to the improved flexibility in the structure as well as the completely exposed active sites of the applied 2D MOF, providing a new insight for developing this group of catalysts.

In 2021, Wang et al.[21] showed that a series of MOF composites, when used as electro-catalyst in electrochemical CO_2 reduction, lead to better selectivity and actitivity with the help of visible light. They constructed the MOF composites (MOF-NS-M) [NS: nanosheet, M = Cu,Co, Fe] through anchoring atoms of metal on MOFs with nanosheet structure. Among them, the FE_{CO} of MOF-NS-Co appears to be more than 90% within the potential range of −0.5 to −1 V versus RHE reaching 98.7% with 100 mV positive shift, which demonstrates an enhanced yield compared with the result measured under dark. This improvement is attributed to the abundant active sites being available thanks to the nature of nanosheet and the rearranged path for transmitting the electron which is provided by the porphyrin photoswitch.

Copper(II) oxide NPs have received interest as active catalysts for various reactions. For example, in 2020, Sun et al. [58] prepared a MOF composite by immobilizing CuO NPs on Cu-MOF to be applied in electrochemical CO_2 reduction through solvothermal method. The resulting MOF composite shows a higher efficiency (FE of 50%) than base materials (the Faradaic efficiencies for CuO and MOF-Cu are respectively 25.5% and 37.6%) in electrochemical reduction of CO_2 and its conversion into ethylene. This improved electrocatalytic proficiency is ascribed to the special two-dimensional configuration of MOF-Cu causing more absorption and activation of CO_2 molecules, and therefore leading to more availability of metal sites.

2.1.4. MOF composites with porous materials

Because of the organic structural units in MOFs, the conductivity of most MOFs is very low and electron transfer to the active centers inside the channels is not easy. Therefore, to increase the conductivity and activate the catalytic centers, some materials are always added to the MOF framework to help transfer electrons. A particular type of MOF composite includes those generated by combining MOFs with porous materials such as other MOFs with different apertures, or polyoxometalates (POMs), or covalent organic frameworks (COFs). This type of MOF composite has different applications, one of which is the ability to play the role of a catalyst in photocatalytic CO_2 reduction reactions.

POMs are one of the strongly electron-donating compounds and can participate in rapid and reversible electron transfer reactions. By incorporating POM to MOFs channels, electron transfer from electrodes to the active centers of the catalyst is easily carried out and therefore, it leads to high efficiency of CO_2RR reactions. During recent years, POM@MOF composite has attracted much attention for some special properties including ultrahigh porosity, large specific surface area, and excellent redox transformation [59-62]. For instance, Lan and coworkers reported the preparation of a directional electron transfer channel at a molecular level by synthesizing a series of mixed–valence H-POM@PCN-222(X) [X = Co,Fe,Mn,Ni] composites via a post–modification method [63]. Among them, H-POM@PCN222(Co) shows an enhanced performance in CO_2 electroreduction reaction toward CO with a FE of 96.2% and a good stability of 10 h. DFT calculations attributed this improvement to the introduction of the POM accelerating electron transfer to active single metal sites of Co and therefore the reduced energy barrier for the rate determining step.

A new type of MOF composite can be produced by using a MOF in the role of a shell spread on the surface of another MOF (MOF@MOF). This

type of composite is fabricated in several methods and in several structures including core-shell, yolk-shell, etc.[64] For example, in 2019, Xu et al. [65] constructed such a MOF composite [Au@Pd@UiO-67/Pt@UiO-n n = 66,67,68] and applied that as a catalyst in CO_2 reduction reaction. In this composite, Au NPs are utilized as cores for Pd shells and Au@Pd core-shell is embedded in the center of Au@Pd@UiO-67 spheres (Fig. 5). Au@Pd core-shell regulates the structure and morphology of UiO-67 and increases the selectivity of carbon monoxide. Platinum NPs are then spread over the surface of the Au@Pd@UiO-67 spheres to create Au@Pd@UiO-67/Pt. These NPs accelerate CO_2RR. In the next step, the obtained composite is coated with UiO-n and this part of the final molecule regulates the reverse water–gas shift reaction.

2.2. Photoreduction of CO_2 by MOF composites

The intelligent choice of the type of MOF is the first important step to have an efficient photocatalyst [66,67]. Multi-factor MOFs formed by combining heterogeneous bonds in one crystal can be an option with high selectivity for CO_2 absorption [68]. CO_2 selectivity, capacity and CO_2 absorption can also be increased through the improvement of open and active metal sites by using precious metals such as platinum [69]. In addition to the issue of surface modification, the analysis of the dynamic behavior of CO_2 in a wide range of temperature and pressure, in the presence of MOFs, is very important [70]. MOFs can improve CO_2 reduction performance by unique CO_2 absorption in photocatalytic process. In addition, MOFs can play an effective role in the photocatalytic process of CO_2 reduction via a photosensitizer role. However, the efficiency of MOFs in the photocatalytic reaction of CO_2 reduction is still very low, which is often due to the poor absorption of visible light and the lack of active electrons. Combining MOFs with various compounds such as molecular catalysts, molecular photocensitizers, carbon materials, etc., by promoting the absorption of light and the separation of charge, improves the photocatalytic properties of the created compound compared to its constituent components.

This review has summarized all attempts aiming at building MOF composites for CO_2 photoreduction. Photocatalytic reaction starts by generating electron-hole pairs stimulated by photon. Photon-stimulated holes on valence band (VB) migrate to the surface of photocatalyst and the oxidation reaction happens. Photon-stimulated electrons on conduntion band (CB) contribute to the reduction of CO_2 to produce valuable products as shown in Fig. 6.

There are some factors affecting the total efficiency of photocatalytic reduction of CO_2, such as band gap (Eg), valence band position, conduction band position, and reaction kinetics.

Phase (1) in Fig. 5 exhibits the electrons and the holes generated by photon radiation. Decrease of Eg which is simultaneous with an increase in light absorption enhances the efficacy of this phase.

Phase (2) illustrates the electron-hole separation due to light radiation. In order to boost the efficiency of this charge-hole separation, two approaches including developing photocatalysts with heterostructures and inducing defects are applied.

Phase (3) indicates charge carrier recombination and phase (4) illustrates the CO_2 reduction reaction to various products.

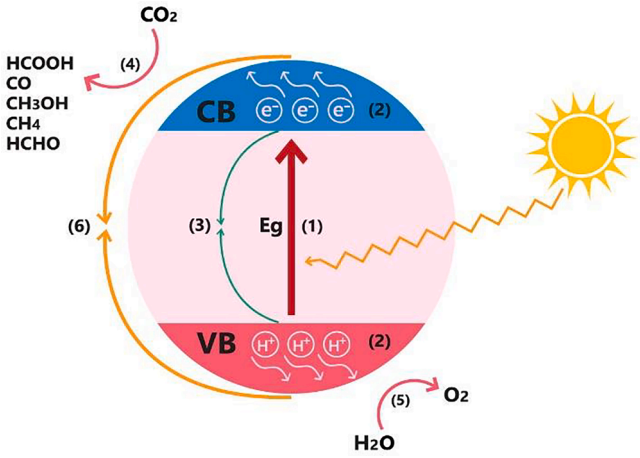

Fig. 6. The photocatalytic reduction of CO_2 over heterogeneous catalysts. Different phases of the process are illustrated in (1) through (6).

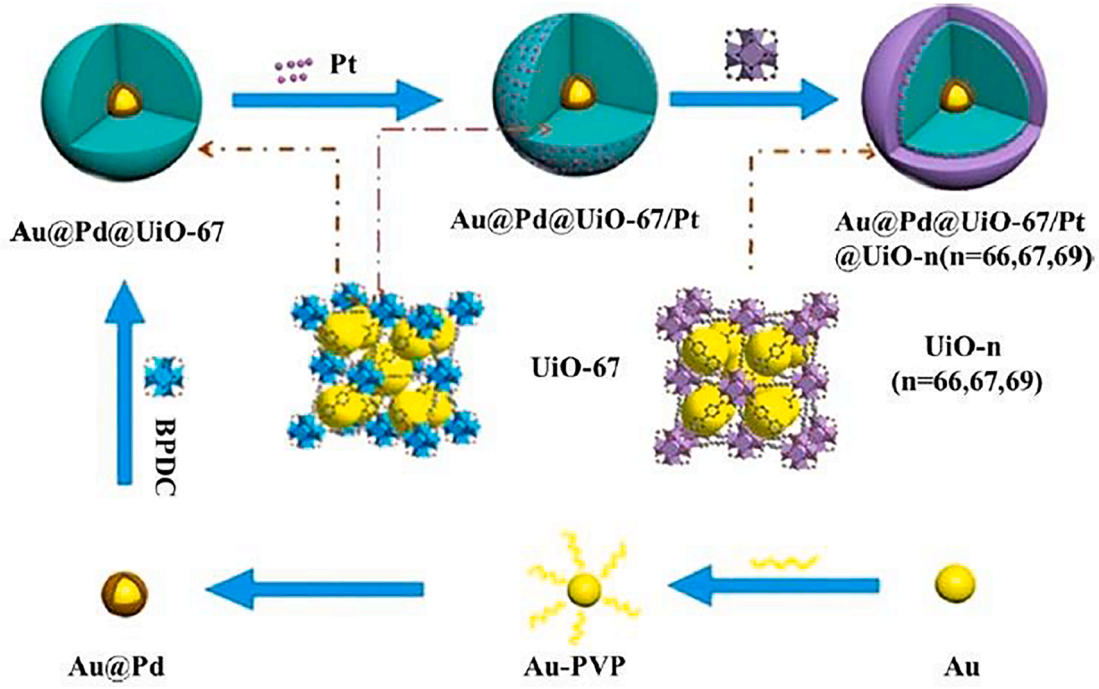

Fig. 5. Synthetic pathway for sandwich Au@Pd@UiO-67/Pt@UiO-n NPs and their nanocomposites [65]. With permission from the American Chemical Society, copyright 2019.

Phase (5) exhibits water oxidation process and phase (6) shows the surface recombination procedure.

In general, three different factors are utilized to evaluate the efficiency of the photocatalytic reaction, including TON, TOF and apparent quantum efficiency (AQE).

TON is defined as the amount of substrate (mole) converted by a photocatalyst (mole) in a specified period of time introduced by Eq. (2).

$$TON = \frac{n}{n_{catalyst}} \tag{2}$$

In Eq. (2), n is defined as the number (mole) of product in a specified period of time and $n_{catalyst}$ is defined as the number (mol) (of the catalyst.

Furthermore, AQE, known as the ratio between the numbers of electrons transferred to the products and the photons hitting the surface from the light source is utilized to evaluate the efficiency of a photocatalyst, exhibited by Eq. (3).

$$AQE = (nN\_Ahc)/AIt\lambda \times 100\% \tag{3}$$

In Eq. (3), n is defined as the number (mole) of product, h denotes the Planck constant, c indicates the speed of light, I denote the intensity of light, t is the reaction time, λ denotes the light wavelength, A is irradiation area, and NA is the Avogadro's constant.

TOF is generally measured according to the specific surface area or the number of active sites on a photocatalyst, as indicated in Eq. (4).

$$TOF = \frac{n}{tn_{catalyst}} \tag{4}$$

In Eq. (4), n is defined as the number (mole) of a specific product, t denotes the reaction time and ncatalyst indicates the number of active sites on a catalyst.

It has been proven that metal-organic frameworks are semiconductors with a band gap energy in the range of 1–5.5 eV, which is calculated from the difference between the highest occupied molecular orbital and the lowest unfilled molecular orbital. Studies on the photocatalytic behavior of MOFs is a relatively new topic. When the linking ligands of MOF are exposed to light, they act as antennas and receive the light energy and activate the metal centers through charge transfer from the ligand to the metal [71].

CO_2 photocatalytic conversion and regeneration is a chemical process that needs to be optimized. Therefore, operating conditions such as temperature, pressure, concentration, reaction time, radiation intensity, etc. must be optimized with great precision. In this way, it should not be forgotten that the goal of this research is to develop CO_2 absorption and conversion technology on an industrial scale, so all operating conditions and the general process should be reasonable and possible on an industrial scale [72].

In this regard, the research of Yangje Fu et al. is one of the pioneering measures in the field of photocatalytic conversion of CO_2. In this research, MOF functionalized by NH_2 was used for the degradation of CO_2 under visible light for the first time. According to past experiences in using MOFs in water decomposition and dye degradation, this research group decided to use MOF for CO_2 degradation. They used NH_2-MIL-125(Ti) as a catalyst in their research. The main rationale behind such a choice is the high potential of Ti in the photocatalytic conversion of CO_2. In addition, the purpose of functionalization by NH_2 is to create sensitivity to visible light. NH_2 does not affect the structure of MOF and in addition to increasing sensitivity to light, it improves CO_2 absorption. The dominant product in this process and in the presence of triethanolamine as a sacrificial species according to Fig. 7 is formate anion ($HCOO^-$). In the following, formate can have wide industrial applications, especially in fuel cells [73]. Considering that the efficiency of this catalyst was not satisfactory, but it showed the potential of MOFs for CO_2 regeneration. The findings of this research stimulated many researchers to design and investigate more effective MOFs for CO_2 photocatalytic reduction [74].

Dengrang Sun et al. investigated the performance of NH_2-UiO-66(Zr) catalyst for the photocatalytic reduction of CO_2 under visible light. They observed a significant improvement in the activity of MOF functionalized with NH_2 compared to MOF without NH_2. In addition, CO_2 uptake increased for NH_2-UiO-66(Zr) catalyst compared to UiO-66(Zr) (Fig. 8A). Because aromatic molecules functionalized with polar molecules such as OH, NH_2 and COOH show more interactions with CO_2, this result is reasonable. According to Fig. 8B, formate production in the presence of triethanolamine (TEOA) is significantly increased under visible light for UiO-66(Zr) catalyst functionalized with NH_2. In addition, they found that replacing the organic linker of 2-aminoterephthalate anion with 2,5-diaminoterephthalate in NH_2-UiO-66(Zr) can improve the photocatalytic performance of the reduction of dioxygen. The mechanism of this process is according to Fig. 9 [75].

In another study, Liu et al presented a creative and intelligent method for CO_2 conversion for the first time. They proposed the production of carboxylic acids through the activation of the C-H bond of alkyne CO_2 bases. Carboxylic acids are used in medical chemistry and synthesis of organic substances. In this research, they converted CO_2 into carboxylic acids through Ag@MIL-101(Cr) as a MOF doped with silver at a pressure of one atmosphere and a temperature of 50 °C as shown in Fig. 10. Such photocatalysts have a very high potential for simultaneous absorption and reaction of CO_2 (with 96.5% yield). Although this study affords good activity but there were several problems with it. MIL-101

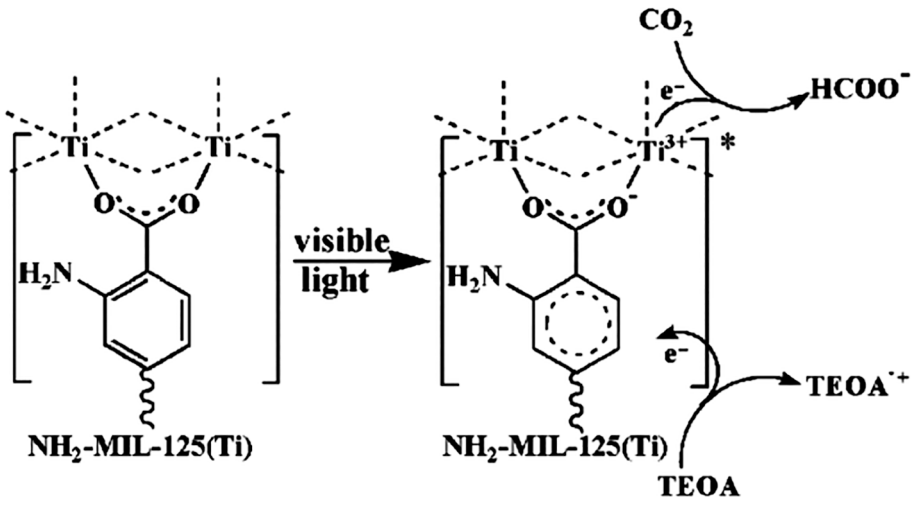

Fig. 7. The photocatalytic conversion mechanism of CO_2 on NH_2-MIL-125(Ti) [73]. With permission from Science, copyright 2013.

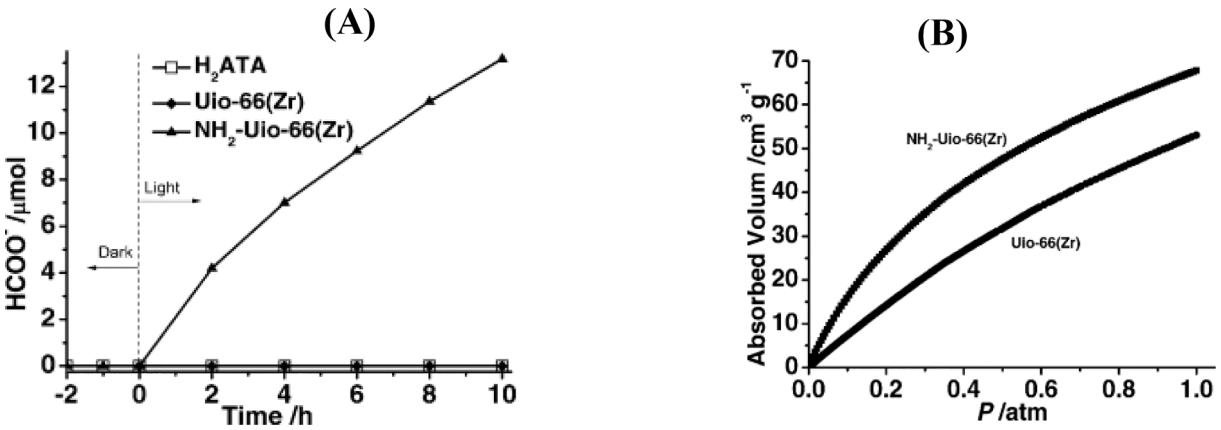

Fig. 8. (A) CO_2 adsorption isotherm on UiO-66(Zr) and NH_2-UiO-66(Zr), (B) $HCOO^-$ production according to irradiation time for UiO-66(Zr) and NH_2-UiO- 66(Zr) [75]. With permission from the American Chemical Society, copyright 2015.

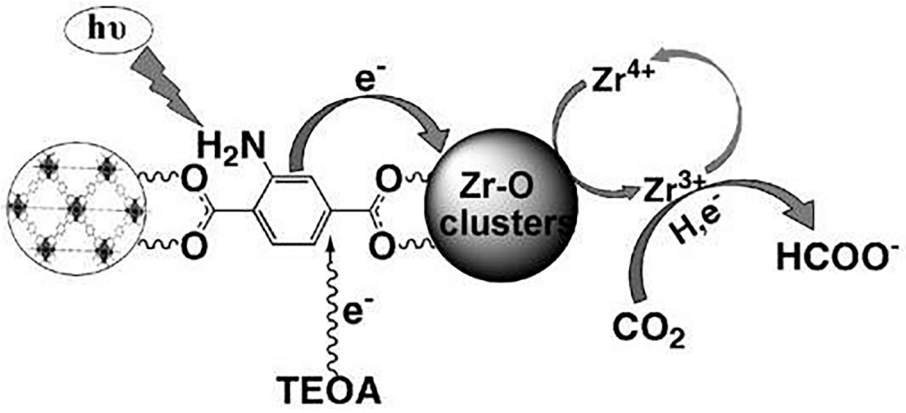

Fig. 9. The photocatalytic conversion mechanism of CO_2 on NH_2-UiO-66(Zr) [75]. With permission from the American Chemical Society, copyright 2015.

(Cr) contains a significant amount of Cr(III), which is environmentally hazardous.

In addition, hydrofluoric acid is used in the preparation of MIL-101 (Cr), which is a harmful substance. As a result, Liu et al decided at that time to investigate another MOF for this process and accordingly selected Ag@MIL-100(Fe) and Ag@UiO-66(Zr) as alternative catalysts. This MOF was safer, and their synthesis was easier compared to MIL-101 (Cr). The activity of Ag@MIL-100(Fe) was like that of Ag@MIL-101(Cr) with 94.6% yield, while the photocatalytic activity of Ag@UiO-66(Zr) (with 97.7% yield) was higher than that of Ag@MIL-101(Cr). The mechanism related to CO_2 conversion on Ag@MIL-101(Cr) and Ag@MIL-100(Fe) is as shown in Fig. 10 [76].

Dengek et al. worked on a series of iron-based MOFs. The advantages of using iron are its abundance and safety. They observed that MIL-101 (Fe), MIL-53(Fe) and MIL-88B have photocatalytic activity to convert CO_2 in the presence of TEOA as a sacrificial species under visible light irradiation to produce formate as a reaction product. According to the mechanism shown in Fig. 11, excitation of Fe-O clusters causes electron transfer from O^{2-} to Fe^{3+} to form Fe^{2+}. The amount of $HCOO^-$ produced of MIL-101(Fe), MIL-53(Fe) and MIL-88B(Fe) are 59.0, 29.7 and 9.0 μmol, respectively. Among these three samples, MIL-101(Fe) showed the highest photocatalytic performance due to having coordination

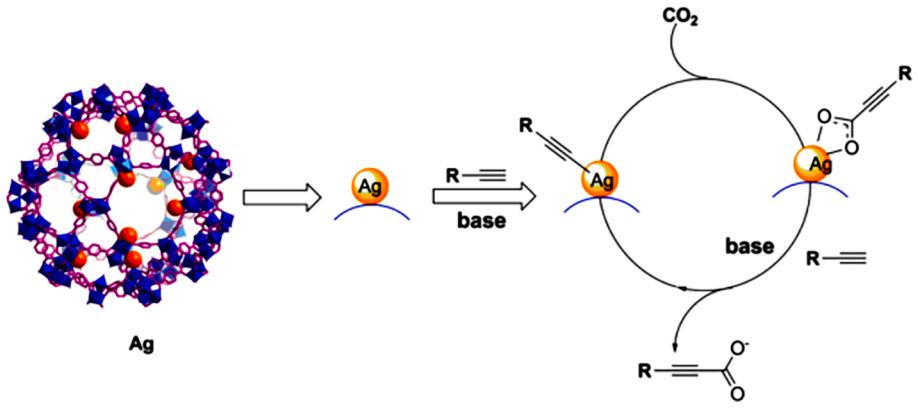

Fig. 10. The photocatalytic conversion mechanism of CO_2 on Ag@MIL-101(Cr) [76]. With permission from the American Chemical Society, copyright 2017.

unsaturated active centers. Similar to the previous results, functionalizing the MOF with NH_2 groups leads to better performance [26].

As stated earlier, MIL and UiO are the most important MOFs in the photocatalytic conversion of CO_2. Zhou et al proposed a different idea which was to use PCN-222 as a photocatalyst. PCN-222 (porous MOF based on Zr-iron porphyrin) prevents electron-hole recombination due to its high electron trapping power. As a result, PCN-222 has higher product yield. The reaction was carried out under visible light irradiation and in the presence of TEOA as a sacrificial species, which produced formate according to the mechanism presented in the reaction shown in Fig. 12 [25].

In another study, for the first time, Chambers et al. used rhodium-based catalysts for CO_2 conversion. In this process, molecular rhodium was placed in the structure of a MOF called pentamethylcyclopentadiamine (Cp* = Cp*Rh@UiO-67), which played the role of active reaction centers. Although the activity of heterogeneous and homogeneous reaction systems is the same, but this type of heterogenization process increases the stability and selectivity compared to homogeneous reaction systems. According to Fig. 13, the main product of the process was in the presence of TEOA as a formate sacrificial species [37].

According to Fig. 14, the format had the highest production rate at an estimated loading of 10% by weight of the catalyst with a renewal number of 45. According to the results obtained at low concentrations of rhodium as reactive active centers in the cavities of the MOF, a higher selectivity was obtained for formate production, while at high loadings, selectivity decreased due to side reactions. It decreased compared to this product. The two important achievements of this research were: (1) the high potential of linking homogeneous molecules of photosensitizers as active phase in MOFs to create composite solid catalysts. (2) Very high importance of the density of active reaction centers in composite solid catalysts [37].

The idea of introducing molecular catalysts into the MOF proposed by Chambers was used a year later by Geneva et al. They dispersed single unsaturated cobalt atoms in MOF-525. The developed MOF had the ability to absorb and photoreduce CO_2 molecules under visible light irradiation. Cobalt single atoms caused efficient electron-hole separation in the MOF. Using unsaturated cobalt active centers ensures their contact with CO_2 molecules and prevents their clumping. According to Fig. 15, in the presence of TEOA, CO and CH_4 were the products of this process, and their production was 3.13 and 5.96 times higher than that of the unmodified MOF [77].

Based on previous research, it has been determined that semiconductors such as TiO_2 have a high potential for photocatalytic reduction of CO_2. Combining good materials can lead to extraordinary results, as was done by Crick et al. They developed a dual-purpose material for absorbing and converting CO_2 by combining TiO_2 nanosheets and an organic framework. In fact, they used the high absorption capability of the MOF NH_2-UiO-66 along with the good photocatalytic properties of TiO_2 in one set. In such systems, the organic-metallic framework increases the absorption of CO_2 and accelerates their access to the active reaction centers through its cavity space. According to Fig. 16, the only product of this solid-gas system in the presence of hydrogen as a sacrificial species and under ultraviolet-visible light irradiation was CO. As described earlier, Sun et al showed that NH_2-UiO-66 has a high potential for CO_2 conversion (Fig. 16). But this process was done in the solid-gas system and in this respect, it is different from Sun's work that used the liquid-gas system. Therefore, the role of NH_2-UiO-66 in CO_2 conversion has been very insignificant compared to TiO_2 in this process. The advantages of using MOFs with high available specific surface are prevention of TiO_2 clumping, increase of active reaction centers, strong absorption and separation of charges along with better absorption of light, which causes absorption of light in the visible region. In this research, nanocomposites containing an average of 20% NH_2-UiO-66 were about one and a half times more active than pure TiO_2. In optimal conditions, with equal amounts of both components, the activity of nanocomposite is 1.9 times higher than pure TiO_2, which is considered a good result [78].

Elah et al investigated the improvement of MIL-53 absorption by incorporating multi-walled carbon nanotubes (MWCNTs) and carbon nanofibers (CNFs) into the MOF. According to Fig. 17, they achieved a significant improvement in CO_2 absorption. The rationale behind these observations is to increase the specific surface area using CNTs and CNFs. Their only goal in this process was to absorb CO_2 without converting it. Anyway, this idea can be a suitable method for use in CO_2 recovery systems [79].

2.2.1. MOF/Metal NPs composites

Metallic NPs have been of special interest to researchers due to their unique properties. Some reports of the application of MOF/metal NPs composites for photocatalysis of CO_2 reduction reaction are summarized in Table 2. In the domain of photocatalytic reactions, plasmonic metal NPs such as Au, Ag, and Pt have recently attracted much attention. The reason is that such NPs can increase solar energy absorption by using optical antenna effect and consequently enhance the catalytic activity. Many efforts have been made during past years to construct MOF composites from Au, Ag, and Pt NPs to be applied in photochemical reduction of CO_2. For example, Wang and coworkers prepared Ag@Co-ZIF-9 MOF composite from doping Ag NPs into Co-ZIF-9 [80]. They developed a system from $[Ru(bpy)_3]Cl_2{\cdot}6H_2O$ to be applied as photosensitizer (bpy = 4,4′-bipyridine), TEOA as electron donor, and Ag@Co-

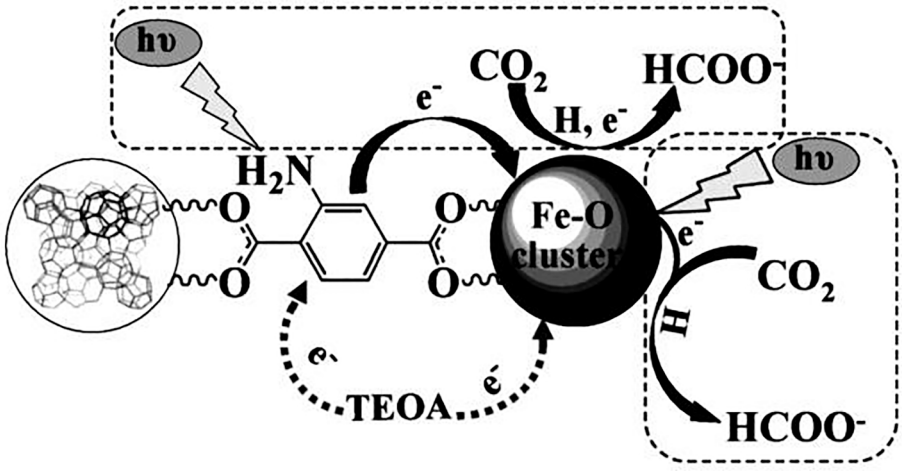

Fig. 11. Mechanism of photocatalytic conversion of CO_2 over NH_2-functionalized iron-based MIL MOFs [26]. With permission from the American Chemical Society, copyright 2014.

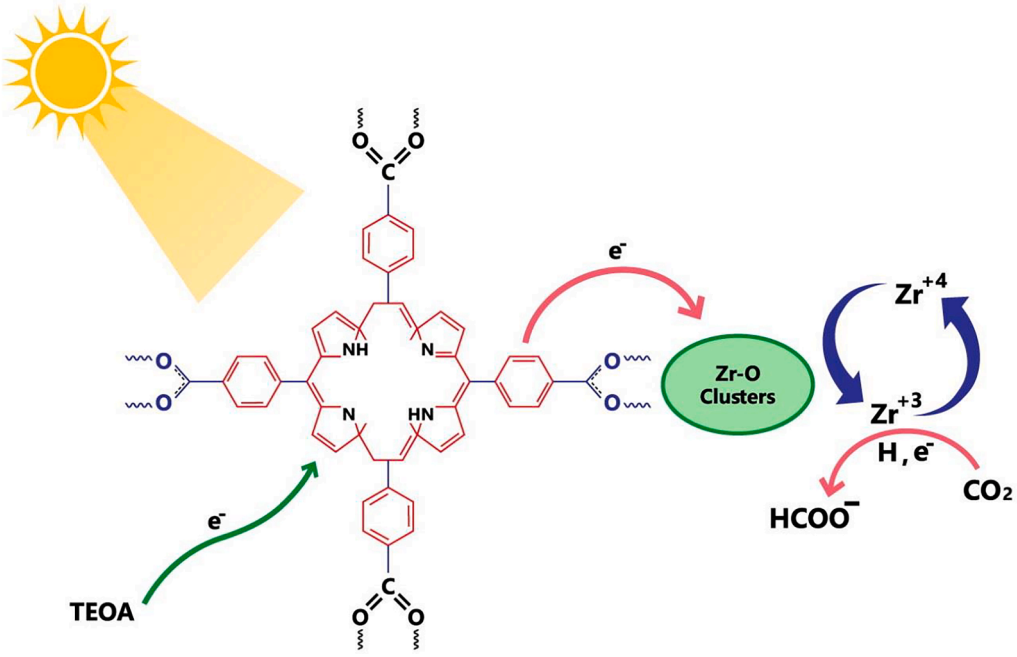

Fig. 12. The photocatalytic conversion mechanism of CO_2 on PCN-222 [25]. With permission from the American Chemical Society, copyright 2015.

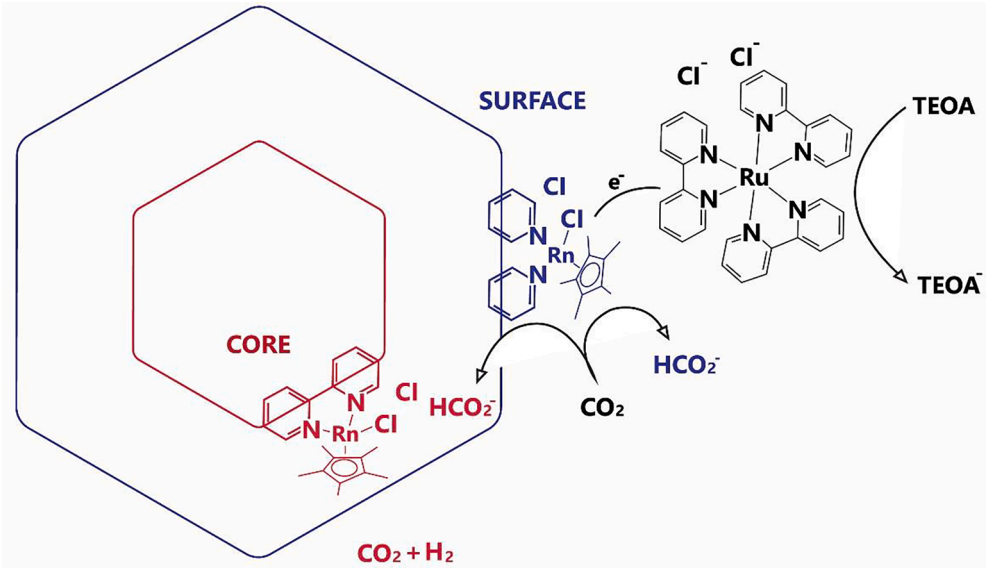

Fig. 13. Mechanism of photocatalytic conversion of CO_2 to formate in Cp*Rh@UiO-67 catalyst [37]. With permission from the Wiley-VCH, copyright 2015.

ZIF-9 as photocatalyst. This system represents an activity increase of more than 2 times (around 28.4 μmol CO) and an enhanced selectivity (20%) for 0.5 h irradiation in comparison with Co-ZIF-9. This increase is ascribed to the attendance of silver NPs serving as electron traps and active sites in CO_2 reduction.

Due to the photothermal effect, the plasmonic materials caused reaction temperature to rise under light irradiation. For example, Wang et al. designed plasmonic catalysts with high performance. They reported a zirconium-based MOF composite encapsulating plasmonic AuPt alloy NPs (AuPt@UiO-66-NH_2) as photothermal catalyst for CO_2 reduction [81]. This MOF composite produced CO from CO_2 reduction with a good selectivity of 91% and a rate of 1451 μmol g_{metal}^{-1} h^{-1}. The outstanding performances of AuPt@UiO-66-NH_2 are ascribed to the synergistic effect originating from the plasmonic metal Au, doped active metal Pt, and encapsulation structure of UiO-66-NH_2 shell.

Also, a typical example for MOF/MNPs composites with plasmonic Ag NPs for photoreduction of CO_2 to CO was presented by Yaghi and coworkers [82]. They fabricated modified UiO-67 out of $Zr_6O_4(OH)_4(-CO_2)_{12}$ secondary building units (SBUs) as well as ReTC and BPDC (Fig. 18a). Afterward, the silver nanocubes are covered with MOF (Re-UiO-67) to render Ag-Re-UiO-67 (Fig. 18b) which resulted in a 7-fold improvement of CO_2-to-CO photoreduction activity in comparison to Re-UiO-67 exposed to visible light, placing an emphasis on this fact that doped silver NPs on MOFs improve the selectivity and efficiency of such compounds in photochemical CO_2 reduction reaction.

In 2021, Fei et al. [83] used Au nanocluster for synthesis of Au-NC@MOF composite. They used heterogeneous nucleation method for stabilizing Au nanocluster by activated N-heterocyclic carbene (NHC) moieties in a porous solid state matrix, and then applied it as catalyst in photocatalytic CO_2 reduction reaction. In the process of heterogeneous

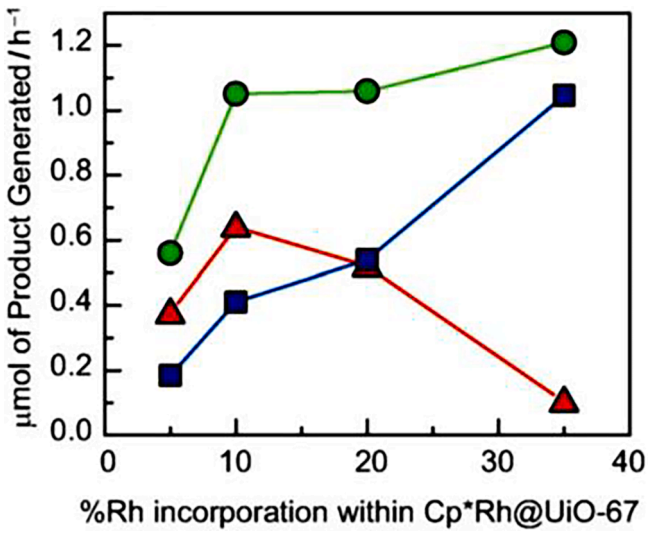

Fig. 14. Production rate of Formate (red triangle), Hydrogen (blue square) and total product (green circle) versus the loading of the rhodium catalyst [37]. With permission from the Wiley-VCH, copyright 2015.

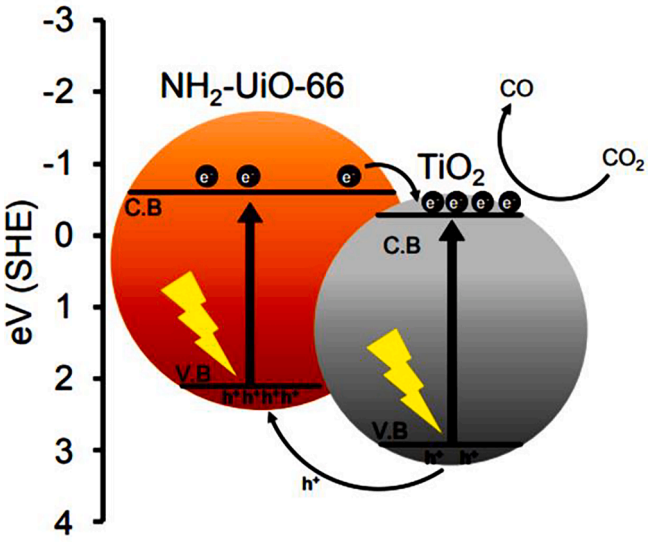

Fig. 16. CO_2 reduction mechanism in the presence of TiO_2/NH_2-UiO-66 [78]. With permission from the Elsevier, copyright 2017.

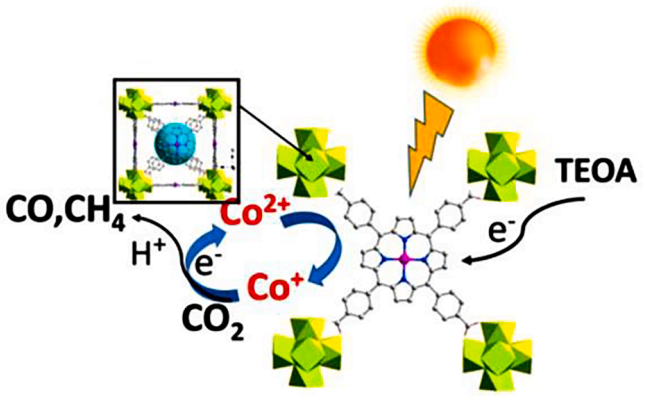

Fig. 15. CO_2 reduction mechanism in the presence of MOF-525-Co [77]. With permission from the Wiley-VCH, copyright 2016.

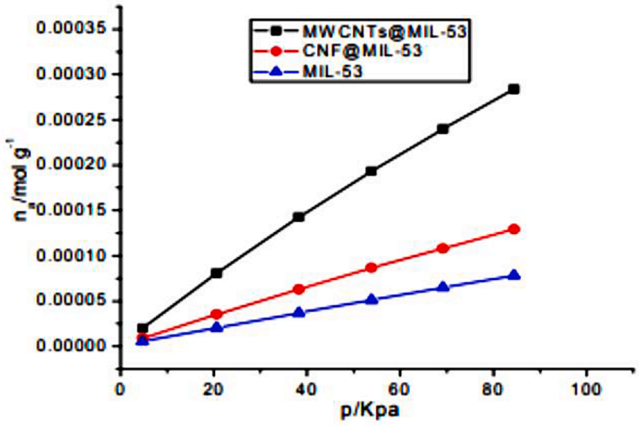

Fig. 17. Results of CO_2 uptake on unmodified MIL-53 and CNT- and CNF-modified MIL-53 [79]. With permission from the Trans Tech Publications, copyright 2014.

nucleation, Au-NCs were stabilized within the MOFs using NHC as ligand and the Au-NCs become dispersed well in a regular array within the pores of UiO-68-NHC. Covalent bonding between UiO-68-NHC and Au-NCs leads to the formation of materials with high chemical and optical stability. L-glutathione was used for the reduction of Au^{III} to Au^0 (Fig. 19). The resulting MOF composite shows a 4-fold improvement in photocatalytic CO_2 reduction compared to control materials with no NHC-ligand stabilization. Such improvement is attributed to the synergistic effect of MOF and gold nanoclusters which gives rise to the formation of MOF-NHC-Au bridges.

Liu et al.[84] provided Au@NENU-10 system from Au NPs, $[PTi_2W_{10}O_{40}]_7-$(PTiW)POM, and HKUST-1 MOF. Afterward, they applied the new system as photocatalyst in photochemical CO_2 reduction. It showed excellent selectivity and performance in CO formation from photoreduction of CO_2 under irradiation visible light. This excellent improvement owes to synergism of metal complex and MOF, as well as excellent charge separation thanks to the direct contact between Au NPs and PTiW.

Later, Deng et al.[85] synthesized cobalt-based MOF in two ways: First time through conventional solvothermal method whose product is called MOF-74-C, and the second time through transformation strategy whose product is referred to as MOF-74-T. Also, Ag NPs@Co-MOF-74 (Ag NPs@MOF-74) is prepared by the corresponding Ag NPs@Co-ZIF-67. Then they used them as catalyst in photochemical CO_2 reduction reaction. The results indicate that Ag NPs@MOF-74 and MOF-74-T provide efficiencies which are respectively 3.8 and 1.8 times as much as that of MOF-74-C in CO_2 photoreduction reaction. The observed enhancement is ascribed to the larger surface area, hollow structure along with the local surface plasmon resonance effect induced by the Ag NPs.

In 2019, Wang et al. investigated how the size of photocatalyst influences its activity. They demonstrated that photocatalyst size has an inverse relationship with its photocatalytic activity in CO_2 reduction reaction [86]. They showed that as the size of MIL-101(Cr)-Ag MOF composite is reduced from 80 to 800 nm, the rate of photochemical CO_2 reduction increases, and the highest photocatalytic activity occurs at a size of 80 nm with a rate of 808.2 μmol $g^{-1}h^{-1}$ for CO production. The increased catalytic activity of MOF composite by reducing the size may be ascribed to the enhanced concentration of unit cells on the boundaries of MOF composite facilitating the electron transport in the photochemical reaction.

One of the features of MOF/metal NPs composites is the ability to form Schottky junctions that improve charge transfer in photocatalytic reactions. Through such intersections, electrons may efficiently migrate to metal NPs and toward the cavities on the semiconductors, leading to

the spatial separation of photogenerated charge carrying particles. Wang et al. took advantage of the formed Schottky junctions to improve photocatalytic properties. They synthesized a series of flower-like Pt@NH_2-UiO-68 composites within which Pt NPs have been embedded both inside and outside of NH_2-UiO-68 [87]. They found that Pt@NH_2-UiO-68 with 2 %wt Pt NPs shows the highest CO_2 photoreduction activity in CO production (66.7 mmol $g^{-1}h^{-1}$) exposed to visible light irradiation. Good charge transfer in this process is attributed to the excellent contact between Pt NPs and NH_2-UiO-68 which was resulted from suitable location and content of Pt NPs in MOF composite. Also, the migration of charges from NH_2-UiO-68 to the Pt NPs through the Schottky junction could prevent the probable recombination of the electrons and holes generated by light irradiation.

ZIFs act synergistically to facilitate electron transfer and contribute to high photocatalytic efficiency by increasing active electrons. In 2020, Becerra et al.[88] prepared Aux@ZIF-67 MOF composite by depositing plasmonic Au NPs on ZIF-67. Having utilized it as photocatalyst in photochemical CO_2 reduction, they gained methyl alcohol and ethyl alcohol as products. They demonstrated that the resulting MOF composite, containing Au NPs with dimensions of 30 to 40 nm, improves visible light absorption. Charge separation appears to be a key factor in product selectivity and enhances photocatalytic performance of CO_2 reduction toward methyl alcohol and ethyl alcohol by an overall yield of 2.5 mmol$g^{-1}h^{-1}$ for CH_3OH and 0.5 mmol$g^{-1}h^{-1}$ for C_2H_5OH which are amongst the top amounts reported in analogous cases.

Hollow metal NPs with core@void@shell architecture show good potential in catalytic activity, due to the synergistic effect between cores and shells to improve performance and increase productivity. Wang et al. constructed core-shell catalyst Au@Pd@MOF-74 [89], by encapsulating Au@Pd NPs into MOF-74 nanoshuttles. Having used it as catalyst in photochemical reduction of CO_2, they obtained methane with a high yield of 84%. The improved chemical activity of the resulting MOF composite is ascribed to the high surface area provided by MOF component and the enhanced optical sensitivity thanks to the presence of NRTs (Fig. 20).

Gold NPs show intense light focusing and strong visible spectrum absorption due to the stimulation of the localized surface plasmon resonances (LSPR), and the stimulation of gold is higher than light-induced electron-hole recombination leads to better electron absorption efficiency. Using this property of gold, Duan and coworkers, and Li et al. achieved a high efficiency of the synthesized composite. They severally prepared formic acid and formate by using the above-mentioned MOFs. Duan and coworkers [90] constructed hybrids of thin porphyrin–based MOF nanosheets (PPF-3–1) anchored with Au NPs through electrostatic interaction. The resulting MOF composite with optimal ratio (Au/PPF-3-1A) shows a higher efficiency (4-fold) compared to PPF-3–1 when used individually for producing formic acid (a formation rate of 42.7 μmol g^{-1} h^{-1}). This higher efficiency is attributable to the transfer of plasmon resonance energy from gold NPs to PPF-3.

On the other hand, Li et al. [91] by constructing M/NH_2-MIL-125(Ti) (M = Pt and Au) investigated the effect of noble metals on the photocatalytic performance of CO_2 hydrogenation. Pt/NH_2-MIL-125(Ti) exhibited an improved activity in producing photocatalytic formate in comparison with NH_2-MIL-125(Ti) alone, while Au adversely affects this reaction. It is attributable to the more elevated potential barrier of hydrogen spillover from gold catalyst to the framework of NH_2-MIL-125 (Ti) relative Pt.

Single atoms (SAs) catalysts with unique electronic structures and unsaturated coordination mediums have uniform and more catalytic sites compared to traditional metal particles. Therefore, their development can help to promote a highly efficient photocatalytic process. In 2020, Wang et al.[92] made a comparison between the catalytic efficiency of CuSAs/UiO-66-NH_2 and Cu NPs/UiO-66-NH_2 for producing methanol and ethanol. According to the results, CuSAs/UiO-66-NH_2 not only shows an improved efficiency compared to Cu NPs/UiO-66-NH_2, but also reveals more selectively than Cu NPs/UiO-66-NH_2 in producing methanol and ethanol. Such improvement is attributed to simple conversion of CO_2 into *CHO and *CO intermediates.

Moreover, some MOF composites were constructed from cobalt single atoms and cobalt NPs severally supported on different MOFs, and their catalytic effects in photochemical CO_2 reduction of were discussed. In 2016, Ye et al.[77] constructed CoSAs@porphyrin MOF and utilized it in photochemical CO_2 reduction reaction. This MOF composite shows an enhanced efficiency in photocatalytic reduction of CO_2 toward CO, giving rise to new CO production rate (200.6 μmol $g^{-1}h^{-1}$) and new CH_4 production rate (36.67 μmol$g^{-1}h^{-1}$) which are respectively 3.13 and 5.93 times as much as those acquired for the base MOF. Such improvement is attributed to the presence of single Co atoms in the MOF that can promote the separation of electron-hole pair units of porphyrin. Also, the transfer of electrons from porphyrin toward cobalt atom supplies the electrons with longer lifespan to reduce CO_2 molecules absorbed on Co atom.

Fu et al.[93] constructed [Co NPs/NH_2-MIL-125(Ti)] and utilized it as catalyst in photochemical CO_2 reduction reaction. The new system demonstrated an improved activity compared to NH_2-MIL-125(Ti) when individually used in this reaction. Such improvement is attributed to high electron transfer and good visible-light harvesting by Co NPs doped on NH_2-MIL-125(Ti).

2.2.2. *MOF/semiconductor and carbon material composites*

Some metal-exo clusters in MOFs can act as semiconductor quantum dots, while organic ligands can activate these semiconductor quantum dots through the antenna process by light-induced charge transfer of the ligand to the metal. Therefore, MOFs may perform photocatalytic action

Table 2
Various MOF/Metal NPs Composites as photocatalyst for CO_2 reduction.

MOF Composite	Light source Illumination range	Main Carbon Products [a)]	Selectivity %	Ref.
Ag@Co-ZIF-9	>420 nm	CO (56800)	55.4	[80]
AgNPs@MOF-74	400–1000 nm	CO (1154.3)	n/a	[85]
MIL-101(Cr)-Ag	400–800 nm	CO (808)CH_4 (427.5)	65.4	[86]
Pt@NH_2–UiO-68	400–780 nm	CO (66.7)	100	[87]
Au–NC@UiO-68–NHC	Xe lamp	CO (57.6)	n/a	[83]
Au@NENU-10	>420 nm	CO (12.8)	85.9	[84]
Pt/NH_2-MIL-125(Ti)	420–800 nm	HCOOH (32.4)	n/a	[91]
CuSAs/UiO-66-NH	>400 nm	CH_3OH (5.3)	55.8	[92]
		C_2H_5OH (4.2)	44.2	
Ag ⊂ Re_3-MOF	420–800 nm	CO (2.8)[b)]	n/a	[82]
Au@Pd@MOF-74	500 W Xe lamp	CO (2.46)	n/a	[89]
CoSAs@porphyrin	200–800 nm	CO (200.6)CH_4 (36.67)	n/a	[77]
Co/NH_2-MIL-125(Ti)	Visible light 300 W Xe lamp, 420 nm	HCOOH (38.4)	n/a	[93]

a) μmol $g^{-1}h^{-1}$; b) TON.

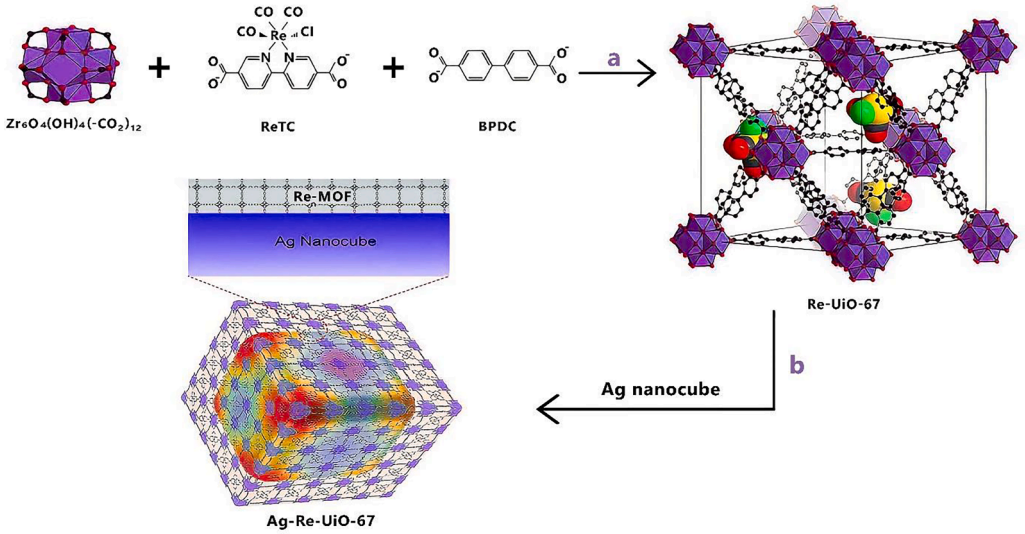

Fig. 18. a) Forming Re-UiO-67 out of $Zr_6O_4(OH)_4(-CO_2)_{12}$ SBUs as well as BPDC and ReTC, b) Coating Re-UiO-67 on an Ag nanocube [82]. With permission from the American Chemical Society, copyright 2017.

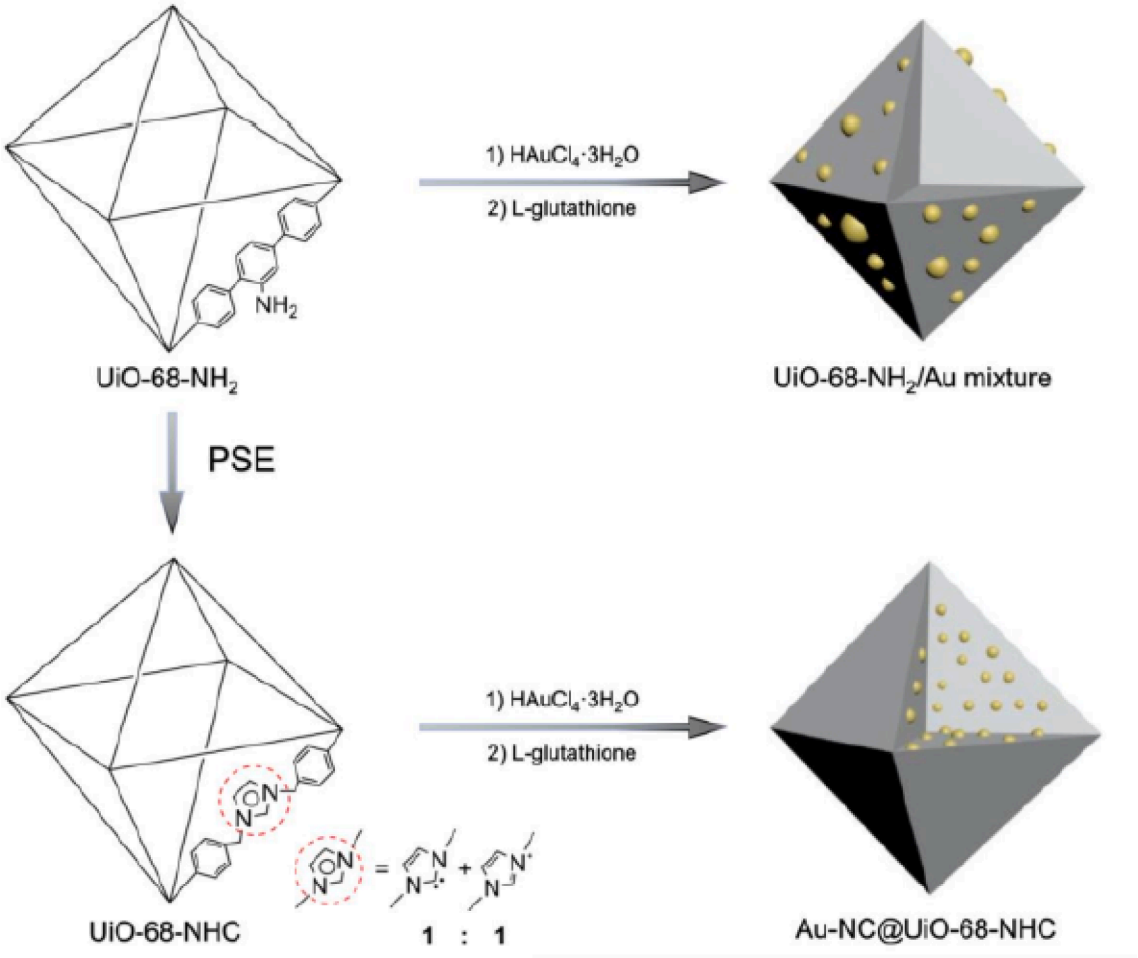

Fig. 19. Representation of synthetic route to UiO-68-NHC, Au-NC@UiO-68-NHC and UiO-68-NH_2/Au mixture [83]. With permission from the Wiley-VCH, copyright 2021.

effectively. However, due to the organic structural units in MOFs, the electrical conductivity of most of them is very poor. The integration of MOFs with semiconductors, which are materials of low toxicity, low cost and high stability, is an effective technique to enhance catalytic efficiency of MOFs in photocatalytic CO_2 reduction. The resulting MOF composite can be further classified as follows according to the type of semiconductor utilized in its structure:

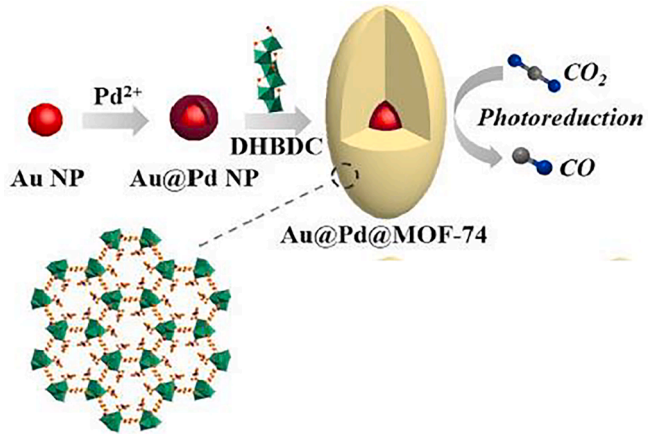

Fig. 20. Schematic representation of the assembly of Au@Pd@MOF-74 [89]. With permission from the Elsevier, copyright 2019.

- MOF and metal sulfide
- MOF and metal oxide
- MOF and perovskite
- MOF and other semiconductors

Some MOF/Semiconductor and Carbon Material Composites with potential application for photocatalysis for CO_2 reduction in Table 3 summarized.

2.2.2.1. MOF/Metal sulfide composites. A particular kind of MOF composite showing good photocatalytic activity in CO_2 reduction reaction is those MOF composites which contain the sulfides of semiconductors such as MOS_2, CdS, Bi_2S_3, etc. in their structure. Such photocatalytic activity is attributed to the appropriate position of CB and good visible light absorption of sulfide semiconductor component. For example, in 2022, Huo et al. [124] constructed a series of 3D hierarchical CdS/Ni-MOF nanocomposites among which the MOF composite containing 20% CdS showed higher activity in photocatalytic conversion of CO_2 to CO in comparison to the base materials (16 and 7 times as much for Ni-MOF and CdS, respectively). This enhancement in activity is attributed to abundant active sites and excellent charge transfer resulted from the synergistic effect of heterostructure in CdS/Ni-MOF as well as its unique hierarchical structure.

Also, in 2022, Liu et al. [156] prepared the photocatalytic Ni@CdS⊂Zn/Co-ZF by a facile self-assembly procedure, from a bimetallic MOF [Zn/Co-ZIF] and Ni-doped CdS NPs (Ni@CdS). Then they applied the new system as catalyst in photochemical CO_2 reduction reaction. The results indicate the high activity of new catalyst in photochemical reduction of CO_2 toward syngas. Furthermore, this system is remarkably efficient to recycle. This remarkable catalytic efficiency is attributed to high visible light harvesting by Ni@CdS and the availability of large effective surface area provided by Zn/Co-ZIF.

Also, some reports have been provided which indicate the production of different MOF composites containing the combinations of CdS with several MOFs including Zr-MOF, Cr-MOF, Zn-MOF, and Co-MOF. For example, Cao et al.[95] constructed CdS/NH_2-UiO-66 MOF composite and utilized it in photochemical CO_2 reduction reaction. The resulting MOF composite exhibits higher photocatalytic efficiency in comparison to CdS alone, NH_2-UiO-66, and CdS/NH_2-UiO-66/chitosan mixed powder when used individually. Such enhancement is attributed to the increased CO_2 adsorption, due to the synergy of CdS and NH_2-UiO-66 causing better charge transfer and suppressing the recombination of charge carriers, and inherent properties of membranes including good stability and the capacity to prevent easy aggregation.

Wang and coworkers [100], investigated performance of CdS/Co-ZIF-9 MOF composite for CO_2 photoreduction. The resulting MOF composite shows an apparent quantum yield of 1.93% for CO production during CO_2 reduction reaction exposed to monochromatic irradiation at 420 nm. According to the following proposed mechanism (Fig. 21): First, there is electron-hole pair generation on the CdS semiconductor. Then, we have negatively charged electron migration to conduction band of CdS, and afterwards its transference to the molecules absorbed on MOF surface and generation of CO_2^- which is stabilized by the benzimidazole linker defined in Co-ZIF-9 frame work. Finally, this generated CO_2^-, by obtaining an H^+, gives rise to CO and water.

CdS-based photocatalysts improve CO_2 photoreduction reaction thanks to their suitable band structure and good optical response. CdS in the core-shell structure is protected from photocorrosion and its absorption capacity increases without reducing its ability to harvest light. Liu et al. constructed CdS/ZIF-8 [101] MOF composite with a core-shell structure. This MOF composite shows higher selectivity (83.96%) and efficiency compared to when CdS is utilized alone. Such improvement is attributable to the strong ability of the resulting MOF composite to absorb CO_2.

In 2019, Zan et al.[104] improved the photochemical performance of the prepared photocatalyst by encapsulating semiconductor NPs within the framework of MOF, instead of simply dispersing them on the surface, because in this case, the contact surface between the MOF and the catalyst and the efficiency of optical charge transfer increase. They constructed CdS/MIL-101(Cr) composite from CdS NPs and MIL-101(Cr) through in-situ-growth strategy, aiming most of the NPs placed within the cavities of MOF composite and the rest of them are placed on the surface of composite. This MOF composite shows higher activity compared to base materials thanks to the effective separation of charge carriers generated after light irradiation because of strong interaction between CdS and MIL-101(Cr). Another example was described by Peng et al.[97] They designed a three-component system including Co(BDC) MOF and CdS as photosensitizer and molecular co-catalyst $[Co(bpy)_3]^{2+}$. Then, they applied the new system as photocatalyst in photochemical CO_2 reduction reaction during which CO was produced with a yield rate of 22 $\mu molh^{-1}$, a selectivity of 92.5%, the corresponding TON of 7.3 (4 h), and an overall efficiency of 0.7% (k = 420 nm). It indicates an improved performance compared to base materials are utilized as catalysts. The improvement is ascribed to highly well-organized transfer of charges at both CdS/MOF and MOF/solution interfaces, as well as further protection of photosentisizer from photocorrosion.

Similarly, in the work of Han et al.[102] the synergistic effect of MOF, molecular co-catalyst and CdS is well shown. They reported a MOF composite (CdS/UiO-bpy/Co) which is a merger of inorganic semiconductor (CdS) and molecular redox catalysts by using MOFs. This MOF composite shows a high efficiency for CO_2 reduction toward CO with a selectivity of 85% and an evoluation rate of 235 $\mu mol\ g^{-1}h^{-1}$. The excellent performance of this MOF composite results from good separation and transfer of charge carriers and active sites of cobalt.

$Cd_{0.2}Zn_{0.8}S$ is one of the semiconductors containing sulfide which produces alcohol in photochemical reduction of CO_2. Wang and coworkers constructed a series of MOF composite systems [$Cd_{0.2}Zn_{0.8}S$@UiO-66-NH_2] with various quantities of UiO-66-NH_2 through solvothermal method [116]. Such a system with optimal ratio (UiO-66-NH_2 content of 20 wt%) shows an enhanced photocatalytic activity for CO_2 reduction in comparison to base materials (a rate of 6.8 $\mu mol\ g^{-1}\ h^{-1}$ for producing CH_3OH). This enhancement is attributed to excellent photocatalyst stability during the reduction process and good transfer and separation charges on the interface connecting $Cd_{0.2}Zn_{0.8}S$ and UiO-66-NH_2.

Molybdenum disulfide (MoS_2) is a semiconductor containing sulfide utilized to construct the MOF composites which are applied in photochemical reduction of CO_2. For example in 2021, Duan and coworkers [111] constructed a system by combining MOS_2 nanosheets with hierarchically porous defective d-UiO-66 in order to fabricate Mo-O-Zr bimetallic sites on the joints between UiO-66 and MoS_2. This MOF

Table 3
Various MOF/semiconductor and carbon material composites as photocatalyst for CO_2 reduction.

MOF composite	Light source illumination range	Main carbon products [a)]	Selectivity (%)	Reference
Ni_3HITP_2/rGO	420 nm	CO (21925)	92.5	[94]
CdS/NH_2-UiO-66	300 W Xe lamp 400–760 nm	CO (521.9)	n/a	[95]
Zn-MOF/ZIF-67 nanosheets	Xe lamp 420 nm 120 mW cm^{-2}	CO (114.5)[f)]	91	[96]
CdS@Co(BDC)-20	420 nm	CO (21925)	92.5	[97]
Co-MOL@GO	450 nm	CO (18016.7)	95	[98]
TiO_2-in-MIL-101-Cr–NO_2	Xe lamp	CO (12800)	11.3	[99]
CdS/Co-ZIF-9	300 W Xe lamp, > 420 nm	CO (2400)	n/a	[100]
CdS/ZIF-8	>420 nm	CO (803.2)	83.96	[101]
CdS/UiO-bpy/Co	>420 nm	CO (235)	85	[102]
TPVT-MOFs@g-C_3N_4	LED visible light	CO (56.4)	99	[103]
CdS/MIL-101(Cr)	>400 nm	CO (16.3)	n/a	[104]
BIF-20@g-C_3N_4	400–800 nm	CO (15.5)	22.4	[105]
$CsPbBr_3$QDs/UiO-66-NH_2	300 W Xe lamp >420 nm	CO (8.21) CH_4 (0.26)	96.9	[106]
MAPbI3@PCN-221($Fe_{0.2}$)	>400 nm	CO (6.6) CH_4 (12.9)	34	[107]
Au/UiO-66-NH_2/GR	>400 nm	HCOOH (505)	80.9	[108]
UiO-66-NH_2/2.0GR	300 W Xe lamp >410 nm	HCOOH (418.7)	78.6	[109]
Au/PPF-3_1	>400 nm	HCOOH (42.7)	100	[110]
d-UiO-66/MoS_2	>400 nm	HCOOH (39)	94	[111]
Zn-Bim-His-1@GQD	>420 nm	CH_4 (20.9)	85	[112]
$CsPbBr_3$@ZIF-67	620 nm Xe lamp	CO (1.67) CH_4 (10.2)	82.1	[113]
CPO-27-Mg/TiO_2	16 W laser,365 nm	CO (4.09) CH_4 (2.35)	36.5	[114]
Cu_2O@MOF(Zn)-1	Xe lamp	CH_4 (1.9)	100	[115]
$Cd_{0.2}Zn_{0.8S}$@UiO-66-NH_2	300 W Xe lamp, >420 nm	CH_3OH (6.8)	n/a	[116]
rGO@NH_2-MIL-125	Hg lamp	methyl formate (1116)		[117]
Zn_2GeO_4/ZIF-8	500 W Xe lamp	CH_3OH (0.22)	n/a	[118]
Zn_2GeO_4/Mg-MOF-74	200–1100 nm	CO (71.9)	n/a	[119]
Co-ZIF-9/TiO_2	300 W Xe lamp,200–900 nm	CO (17.58) CH_4 (1.98)	n/a	[120]
UiO-66/CNNS	300 W Xe lamp,400–800 nm	CO (9.9)	n/a	[121]
(Zr-PMOF)/ultrathin g-C_3N_4	>420 nm	CO (5.5)	n/a	[122]
Al-PMOF/NH_2-rGO (5 wt%)	Visible -light	$HCOO^-$ (685.6)	n/a	[123]
20 %CdS/Ni-MOF	300 W xenon lamp 365 nm	CO (7.47)[e)]	n/a	[124]
Bi_2S_3@NH_2-MIL-125(Ti)-SH	300 W Xenon arc lamp,420 nm	CO (12.46)	n/a	[125]
CdS-P25/ZIF-67	300 W xenon lamp 320–780 nm	CO (1.49) CH_4 (1.58)	n/a	[126]
ZIF-67@a-TiO_2 MOF	300 W Xe lamp, 420 nm	CO (10.95)[d)]	67.2	[127]
PCN-224(Cu)/TiO_2	300 W Xe arc lamp,λ >300 nm	CO (37.21)	n/a	[128]
TiO_2@Cu-BTC	300-V tungsten light	CH_3OH (4000)	n/a	[129]
TiO_2/UiO-66	300 W xenon light	CH_4 (17.9)	n/a	[130]
TiO_2/NH_2-UiO-66	150 W Xe arc lamp λ >325 nm	CO (4.24)	n/a	[78]
Fe-N-TiO_2/CPO-Cu-27	70 W mercury (Hg) lamp 350–600 nm	CH_4 (48.23) CH_3OH (2.19)	n/a	[131]
$Cu_3(BTC)_2$@TiO_2	300 W Xe lamp,< 400 nm	CH_4 (2.64)	n/a	[132]
Co-MOF/Cu_2O	300 W Xe lamp 420 nm	CO (3.83)	100	[133]
Cu_2O@$Cu_3(BTC)_2$	visible-light irradiation >400 nm	CH_4 (0.091)	n/a	[134]
NH_2-UiO-66/SiC	300 W Xenon Lamp, λ >420 nm	CO (7.30)	100	[135]
TiO_2/C@ZnCo-ZIF-L	400–800 nm	CO (28.6)	99	[136]
TiO_2/AuCu/ZIF-8	Xe lamp	CO and CH_4 (86.9)	n/a	[137]
Cu_2O@Cu@UiO-66-NH_2	400–800 nm	CO (20.9) CH_4 (8.3)	n/a	[138]
TiO_2/Cu_2O/$Cu_3(BTC)_2$	Xe lamp 450 W	CH_4 (132), CO (>144)	n/a	[139]
CTU/TiO_2	Xe lamp irradiation >300 nm	CO (31.32)	n/a	[140]
$CsPbBr_3$QDs@2D Cu-TCPP	300 W Xe lamp 420 nm	CO (287.08) CH_4 (3.25)	99	[141]
$CsPbBr_3$/MIL-100(Fe)	300WXe lamp 420 nm	CO (20.4) [e)]	n/a	[142]
g-C_3N_4@Cu/ZIF-8	350–650 nm	CH_3OH (0.12)[e)]	n/a	[143]
g-C_3N_4-RGONH_2-MIL-125 (Ti)	35 W Xe lamp,450 nm	CO (95.9) CH_4 (3.48)	CO (96.53), CH_4 (3.47)	[144]
g-C_3N_4/CuO@MIL-125(Ti)	200–800 nm	CO, CH_3OH, acetaldehyde, C_2H_5OH (180.1, 997.2, 531.5, 1505.7)[e)]	n/a	[145]
Co-MOF/g-C_3N_4	300 W Xe arc lamp 420 nm	CO (6.75) CH_4 (5.47)	n/a	[146]
Co-ZIF-9/g-C_3N_4	visible light (4420 nm)	CO (495)	n/a	[147]
NH_2-UiO-66/g-C_3N_4	300 W Xe arc lamp 400 nm	CO (31.6)	n/a	[148]
C_3N_4@ZIF-8	300 W Xe arc lamp 300–600 nm	CH_3OH (0.75)	n/a	[149]
g-CNQDs/PMOF	visible-light	CO (16.10) CH_4 (6.86)	n/a	[150]
g-CNQDs/Zr-MOF	visible-light	CH_3OH (9264)[e)]	n/a	[151]
UiO-66-NH_2/CNTs	500 xenon lamp, > 400 nm	HCOOH (4.55) [d)]	63.1	[152]
RGO/NH_2-MIL-125(Ti)	Visible light,20 W LED lamp	CH_4 (5.7)[e)] C_2H_4 (0.6)[e)]	n/a	[153]
g-C_3N_4/ZIF-67	300 W Xe lamp λ >420	C_2H_5OH (325.5)	n/a	[154]
Ti-MOF@RuO_X	Xe lamp with >455 nm filter	CH_4 (800)[e)]	n/a	[155]

a) μmol $g^{-1}h^{-1}$.
d) μmol h^{-1}.
e) μmolg^{-1}.
f) nmol h^{-1}.

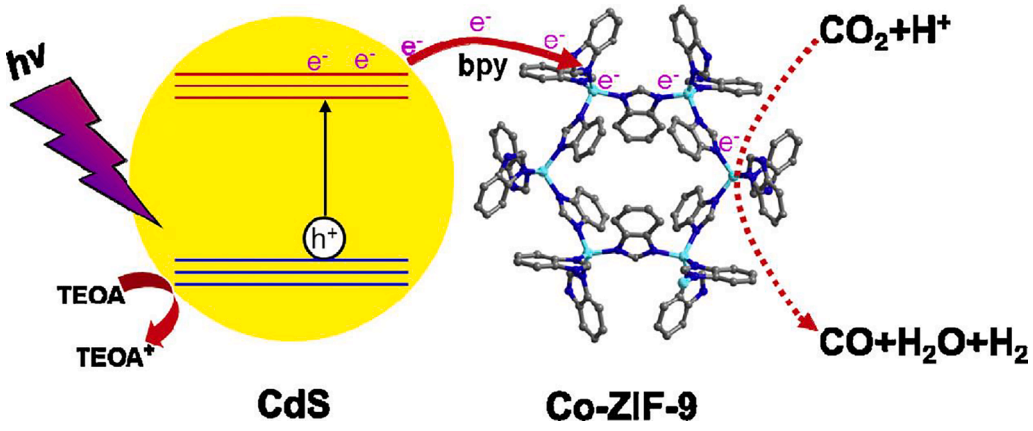

Fig. 21. Proposed mechanism for CO_2 reduction by CdS/Co-ZIF-9 [100]. With permission from the Elsevier, copyright 2015.

composite called d-UiO-66/MoS_2 facilitates the photocatalytic CO_2 reduction for producing CH_3COOH with a selectivity of 94% and an evolution rate 39 μmol $g^{-1}h^{-1}$. They showed that Mo-O-Zr bimetallic sites assist C-C coupling process by reducing the energy barrier. Consequently, acetic acid as a two-carbon product is produced in larger quantities while ethanol as another two-carbon product is produced in smaller quantities.

Bismuth(III) sulfide is another kind of semiconductor which is used in constructing MOF composites to catalyze photochemical reduction of CO_2. Wang et al.[125] constructed Bi_2S_3@NH_2-MIL-125(Ti)-SH composite by the growth of Bi_2S_3 onto NH_2-MIL-125 through the covalent conjunction strategy. This new composite in photocatalytic CO_2 reduction shows a yield of 12.46 μmol $g^{-1}h^{-1}$ for producing CO, indicating a 13-fold improvement compared to when NH_2-MIL-125 is used singly as catalyst. This improvement is attributed to the covalent coordination-driven intimate interfacial interaction in n-scheme heterojunction.

In 2022, Wang et al.[126] constructed the ternary composite CdS-P25/ZIF-67 (P25 = commercial TiO_2) by hydrothermal method. In photochemical CO_2 reduction, the resulting MOF composite exhibits higher efficiency than CdS-P25 or ZIF-67 when used individually (1.58 μmol h^{-1} and 1.49 μmol h^{-1} respectively for CH_4 and CO production). The improvement in photocatalytic CO_2 reduction reaction is ascribed to the excellent charge separation arising from the constructed dual Z-scheme system.

2.2.2.2. MOF/Metal oxide composites. Another group of semiconductors applied in constructing MOF composites are metal oxides like Cu_2O and TiO_2 which dramatically help to promote the photocatalytic features of MOF composites in CO_2 reduction.

TiO_2 is an inert and safe compound which has been widely used as metal oxide semiconductor in photocatalytic reactions such as photocatalytic CO_2 reduction. Many efforts have been made during past years to fabricate the composite of TiO_2 and ZIF. For example, Wu and coworkers [126] prepared the core-shell ZIF-67@a-TiO_2 MOF composite by hydrothermal method and low temperature calcinations. Then, they utilized it as catalyst in photocatalytic CO_2 reduction in which it showed a higher efficiency toward production of CO compared to when ZIF-67 was utilized individually (a rate of 43.8 μmol for producing CO after 4 h irradiation with a selectivity of 67.2%). This improvement is generated by a-TiO_2 layer due to an enhanced light adsorption as well as suppression of photogenerated electron-holes recombination.

Also in 2016, Xu and coworkers constructed Co-ZIF-9/TiO_2 from Co-ZIF-9 and TiO_2 through in-situ synthetic strategy [120] which causes close interconnection between TiO_2 and the MOF composite leading to higher charge separation. This MOF composite leads to a utilized photoelectron number which is 2.1 times as much as when TiO_2 is alone, also revealing a higher onset potential for reduction of CO_2 and an enhanced photocurrent density in the simulated photoelectrochemical CO_2 reduction reaction.

There are reports available about the preparation of composites from various morphologies of TiO_2 and ZIF-8 [157,158] and their application as catalyst in photochemical reduction of CO_2, all indicating an improved catalytic activity compared to the base materials. This promotion is ascribed to the capability of composite to facilitate the adsorption-desorption of CO_2 and the products, which finally leads to a boosted photoreduction of CO_2 toward CO and CH_4.

During the previous years, several attempts have been made to form different composites from TiO_2 and Cu-based MOFs. For inatance, Wang and coworkers constructed a system from copper(II)-porphyrin zirconium MOF (PCN-224(Cu)) and TiO_2 NPs [128]. This system shows a CO evolution rate (37.21 μmol $g^{-1}h^{-1}$) which is roughly 45 times as much as when PCN-224(Cu) is used (3.72 μmol $g^{-1}h^{-1}$) and 10 times as much as with TiO_2 (0.82 μmol $g^{-1}h^{-1}$). This enhancement is ascribed to more light–harvesting of metalloporphyrin-based MOF and z-scheme mechanism constructed out of the relation between MOF and TiO_2 which improves the separation of photoexcited charges.

Also, there are several reports indicating the fabrication of TiO_2 composites of different morphologies with HKUST-1 through various methods by Credico and Wang [159,160]. These reports all indicate that the catalytic activity of the resulting composite improves compared to the base materials in producing methane in CO_2 reduction reaction. This high performance is attributed to the close contact between two components of the constructed MOF composite which gives rise to higher adsorption of CO_2 by HKUST-1. Also, TiO_2 component in the MOF composite contributes to the increased absorption of visible light, facilitating an efficient injection of electrons from TiO_2 toward HKUST-1.

In 2021, Nagababu et al.[129] constructed four MOF composites including Cu-BTC-MOF, Ni-BTC-MOF, TiO_2@Cu-BTC-MOF, and TiO_2@Ni-BTC-MOF (BTC: 1,3,5-benzenetricarboxylic acid) and then investigated their performance in photochemical CO_2 reduction. Among them, TiO_2@Cu-BTC-MOF shows a yield of 4000 μmolg^{-1} for producing CH_3OH which is a remarkable increase in comparison with analogous systems. Such enhancement is resulted from large internal surface areas and pore volume in the applied MOF composite.

Many efforts also have been made in recent years to form a composite from TiO_2 and Zr-based MOF. In 2020, Wang and coworkers constructed TiO_2/UiO-66 MOF composite via a simple solvothermal and assembly method [130]. The optimum MOF composite with a dominant content of TiO_2 as 81.3 wt% produces methane product with a rate of 17.9 μmol $g^{-1}h^{-1}$ and selectivity of 90.4%. Such enhanced efficiency is attributed to adequate exposed catalytic sites and enhanced CO_2 uptake (78.9 cm^3g^{-1}) on the hierarchical porous structure.

Titanate, one of the derivatives of titania, with a crystal structure like anatase TiO_2 and 1D morphology, is another example of semiconductors

that have photocatalytic activity. Compared with common TiO_2, they are more photocatalytically active with high surface area, uniform morphology, better photogenerated charge separation, and small band gap. Petit et al.[161] have used titanate composite to improve CO_2 photoreduction. They prepared titanate or titania/NH_2-UiO-66 composites with different morphologies and applied them as catalysts in photocatalytic CO_2 reduction reaction. All of the resulting MOF composites produced CO in the above reaction and performed better compared to their base materials. The performance of titanate/NH_2-UiO-66 composite is around 5 times higher than titanate alone, while the performance of titania/NH_2-UiO-66 composite is 9 times higher than titanate. Such improvement is attributed to better transfer of charges between MOF composite components.

For the photoreduction of CO_2 by pure TiO_2 anatase, the available surfaces are limited and the poor adsorption of CO_2 on the surface leads to low catalyst efficiency. The pore space of MOFs can be very helpful for increasing CO_2 absorption and increasing access to catalytic sites. To better control this TiO_2/MOF interaction and increase the catalytic efficiency, Petit et al. carried out an in situ synthesis process to develop NH_2-UiO-66 in the presence of pre-synthesized TiO_2 nanosheets leading to the enhancement of the available levels of TiO_2. They constructed TiO_2/NH_2-UiO-66 nanocomposite via an in-situ process that allows two components to get in touch [78]. This composite shows improvement in CO_2 photoreduction reaction toward CO compared with base materials. This improvement comes from the ability of NH_2-UiO-66 to prevent the accumulation of TiO_2 leading to greater availability of active sites, high porosity of NH_2-UiO-66 which in turn causes more CO_2 absorption on the surface, and also an efficient charge transfer arising from the additional photoexcited electrons.

Moreover, many efforts have been made to make up a composite of TiO_2 and CPO-27. For example, Shariati et al.[131] constructed Fe-N-TiO_2/CPO-Cu-27 MOF composite by combining CPO-Cu-27 MOF with Fe-N-TiO_2. Compared to CPO-Cu-27 when used individually, the resulting MOF composite shows a higher efficiency in photocatalytic CO_2 reduction and produces methane and methanol when exposed to visible light irradiation. The authors also showed that partial pressure of water and CO_2 directly influence the yield of photocatalytic reduction of CO_2. In the best conditions (partial pressures of 0.096 bar for CO_2 and 0.785 bar for water), the production rates of 48.23 μmol g_{cat}^{-1} h^{-1} and 2.19 μmol g_{cat}^{-1} h^{-1} were obtained for methane and methanol, respectively. This improvment in efficiency is ascribed to high CO_2 adsorption capacity, effective charge transfer, preventing agglomeration of NPs, and improving light absorption, all provided by the resulting MOF composite. Also, Li and coworkers combined CPO-27-Mg MOF with TiO_2 to fabricate CPO-27-Mg/TiO_2 through hydrothermal self-assembly method [114]. This MOF composite shows higher efficiency in photoreduction of CO_2 toward CO compared with base materials (with product yield of 41.2 μmolg^{-1}). Also, open metal sites of MOF component prevent water reduction reaction.

It has been found that the amount of titanium oxide loading in composites is important in the photocatalytic performance. For instance, in 2020 Ding and coworkers, introduced a new composite fabricated from titanium dioxide and Cr-based MOF, and investigated its application in photocatalytic reduction of CO_2. They created molecular compartments inside MOF composite via the growth of TiO_2 within various pores of MIL-101 and its derivatives [99]. They investigated the structure–performance relationship by controlling the location and the number of TiO_2 units which were created in MOF composites. They showed that the MOF composite (TiO_2-in-MIL-101-Cr–NO_2) containing 42% TiO_2 has the highest efficiency for CO_2 conversion with an AQE of 11.3 % at wavelength of 350 nm. Such facile photocatalytic CO_2 reduction is the consequence of the synergistic effect between TiO_2 units and catalytic metal cluster.

The way of structural organization of composites also has an effective role in catalytic performance. In one of the works, Li et al. have prepared TiO_2 semiconductor wrapped around the MOF crystal in the form of a shell layer to faciliate easy photoexcitation and the absorption of gas molecules by the MOF are facilitated by the macroporous nature of shell. They formed the binary MOF composite $Cu_3(BTC)_2$@TiO_2 [132] and demonstrated that the resulting MOF composite exhibits a higher efficiency (with production rate of 2.65 μmol$g_{TiO2}^{-1}h^{-1}$) in producing methane during photochemical reduction of CO_2. The reasons for such better activity are: the presence of TiO_2 which facilitates charge separation and provides high-energy electrons for CO_2 molecules adsorbed on Cu, and high adsorption of CO_2 molecules by $Cu_3(BTC)_2$. Similarly, in 2018, Shang et al. [162] compared the catalytic activities of TiO_2@-$Cu_3(BTC)_2$ and TiO_2/$Cu_3(BTC)_2$ MOF composites. TiO_2@$Cu_3(BTC)_2$ contains TiO_2 NPs embedded into $Cu_3(BTC)_2$, while in TiO_2/$Cu_3(BTC)_2$ the TiO_2 NPs are supported on $Cu_3(BTC)_2$. They applied them as catalyst in photochemical CO_2 reduction reaction and compared the result with the case where TiO_2 is utilized individually as catalyst. The results indicated the following photocatalytic activities in producing CO during CO_2 reduction reaction as TiO_2/$Cu_3(BTC)_2$ < TiO_2@$Cu_3(BTC)_2$ > TiO_2. The higher efficiency of TiO_2/$Cu_3(BTC)_2$ is attributed to the interface formed between TiO_2 and $Cu_3(BTC)_2$ which contributes to electron transfer.

Cu_2O is another metal oxide semiconductor which is favorable for CO_2 reduction thanks to its efficient light absorption and an appropriate conduction band position. There have been efforts to composite Cu_2O with Zn-MOF, Co-MOF, and Cu-MOF and all of them showed improved catalytic properties compared to the base materials. For example, Wen and coworkers introduced the catalyst resulted from Co-based MOF and nanocrystalline cuprous oxide [133] revealing an enhanced efficiency for photocatalytic CO_2 reduction with an outstanding CO production rate of 3.83 μmol $g^{-1}h^{-1}$ which is 9.6 times higher than the rate obtained by Cu_2O alone. Compared to other reaction routes, this photocatalytic reduction of CO_2 with enhanced selectivity toward CO is achieved at the interface of solid–gas reaction where no photosensitizer or sacrificing reagent has been applied. Also, Ng et al. [134] compared the catalytic activities of Cu_2O@$Cu_3(BTC)_2$ and Cu_2O in photochemical CO_2 reduction toward methane production. The results indicated an improved activity equaling 1.9 times as much as the bare sample. This improvement stems from the facilitated charge separation and CO_2 adsorption by MOF component. Moreover, the ability of MOF component to stop the corrosion of Cu_2O by water gives rise to the stability of the resulting catalyst. In another work, Antonino et al. [115] have applied Zn-based MOF, the use of which is normally limited due to its instability at high temperatures in photochemical reduction of CO_2 toward methane. Then they made a composite out of the MOF and small Cu_2O NPs which provided an enhanced photocatalytic activity in producing methane from CO_2 reduction (TOF: 50.10^{-3} S^{-1} at 215 °C). Such significant efficiency appears to be a result of highly photocatalytic performance of the framework accompanied by the small-sized Cu_2O NPs acting as co-catalyst.

There are some attempts made to construct ternary composites by integrating TiO_2 with ZIFs. For instance, the ternary TiO_2/Carbon@ZIF-L composite was fabricated in 2019 by Li et al. through growing ZIF-L on TiO_2/C [136]. This MOF composite shows high efficiency (a rate of 28.6 μmol h^{-1} g^{-1} for producing CO) and selectivity (99%) for CO_2 photoreduction in comparison with base materials. Such improvement is attributed to accessible rich active sites, good light harvesting, and CO_2 capture capability due to synergism of the components of the resulting MOF composite.

In an interesting example, Wang et al.[137] have reported the deposition of plasmonic NPs at the interface of MOF and TiO_2, which can act both as an amplifier for excited charges and as a transfer bridge, leading to optimal absorption of CO_2 and high photocatalytic efficiency. They constructed a system comprising three components as follows: AuCu nanoprisms, thin film of TiO_2 nanoplate and NPs of ZIF. Then, they investigated it as catalyst in photocatalytic CO_2 reduction reaction. This ternary MOF composite shows higher photocatalytic performance and an approximately 7-fold improvement (CO_2 conversion rate: 86.9 μmol

$h^{-1}g^{-1}$) in CO_2 reduction in comparison with the original catalyst without MOF (CO_2 conversion rate: 12.5 μmol $h^{-1}g^{-1}$). This enhancement is ascribed to the presence of ZIF-8 which increases the reactant concentration on the surface of catalyst by high adsorption of CO_2. Moreover, AuCu nanoprisms act as an intermediator for improving the charge density at the intersections and making possible the charge transfer toward CO_2 adsorption sites on ZIF-8 to reduce CO_2 afterwards.

In a similar way, Maina and coworkers designed a ternary membrane in which they utilized Cu-TiO_2 as a substitute for AuCu nanoprisms [163]. They showed that this membrane exhibits higher photocatalytic activity towards CO_2 reduction in comparison with ZIF-8 alone. Their study also indicated that the product yield can be controlled by dosage and composition of NPs. Upon using 7 μg of semiconductor NPs in the structure of MOF composite, a higher performance was observed in comparison with the pristine MOF (CO and methanol yields enhanced respectively by 233 % and 70 %).

In another study, Wang and coworkwers have fabricated Cu_2O@-Cu@UiO-66-NH_2 nanocubes composite by coating Cu_2O@Cu using UiO-66-NH_2 through a solvothermal approach [138]. Both Cu_2O and UiO-66-NH_2 could effectively apply visible light. Cu metal acted as an electron mediator for rapid delivery of photoexcited electrons from Cu_2O to UiO-66-NH_2. Hence, more energetic charge carriers took part in CO_2 reduction on the surface of photocatalyst. The reduction of CO_2 occurred on UiO-66-NH_2 possessing a CB potential higher than E(CO_2/CO) and E (CO_2/CH_4). Cu_2O when used individually had no activity toward CO_2 reduction because of rapid recombination of photoexcited electron–hole pairs. Pure UiO-66-NH_2 only produced CO yielding a formation rate of 6.1 μmol $g^{-1}h^{-1}$. Conversely, Cu_2O@Cu@UiO-66-NH_2 exhibited not only an improved photocatalytic activity but also a higher CH_4 formation. Having enjoyed this ternary structure, CO could be further converted to CH_4, possibly attributable to the presence of p-n junction and Schottky barrier. The CO and CH_4 yields reached 20.9 and 8.3 μmol $g^{-1}h^{-1}$, respectively.

Another MOF composite called TiO_2/Cu_2O/$Cu_3(BTC)_2$ was also prepared by Wang et al in 2018 [139] and exhibited an enhanced catalytic activity to produce methane in photochemical CO_2 reduction in comparison with the original components when used singly. This improvement is ascribed to the elevated density of charge carriers. In another work, CTU/TiO_2 [CTU : CuTCPP on UiO-66-TiO_2 and CuTCPP: Cu(II)tetra(4-carboxylphenyl)porphyrin] was another ternary composite constructed by Wang and coworkers, through the hydrothermal in-situ growth [140]. This MOF composite with optimal ratio [CTU/0.6TiO_2] shows a 7-fold enhanced photocatalytic reduction of CO_2 to CO compared to base material (a rate of 31.32 μmol $g^{-1}h^{-1}$ for producing CO). The CTU composite increases the spread of titanium oxide particles on the surface, resulting in greater CO_2 absorption and higher reaction efficiency. Meantime, Wang et al.[155] compared the catalytic activities of Ti-MOF and Ti-MOF@RuO_X in CO_2 methanation reaction. The catalytid data reveal that the chemical stability and photocatalytic features of Ti-MOF are improved when it forms a composite with RuO_X, consequently enhancing its catalytic activity.

Recently, ZnO/ZIF-8 and M/ZIF-8 composites (M: Pt, Au, Cu NPs) were prepared [164] by decorating ZIF-8 with ZnO, Pt, Cu, Au NPs and employed as catalysts in photocatalytic CO_2 reduction under ultraviolet/visible light irradiation. Among these MOF composites, ZnO/ZIF-8 and Pt/ZIF-8 showed the first and second highest yields in producing methanol in CO_2 hydrogenation reaction. Methanol production rate for ZnO/ZIF-8 and Pt/ZIF-8 reaches respectively 6700 and 5300 μmol g^{-1} after 1 h exposure to UV/Vis irradiation. The superior activity of Pt/ZIF-8 is due to its higher capability to trap the light and its high surface area provides a more effective interaction between CO_2 and photocatalyst, and consequently exhibits higher efficiency compared to Cu and Au. Furthermore, constant generation of electron-hole pairs together with effective charge carrier isolation owing to formation of type II heterojunctions reveals a higher efficiency compared to M/ZIF-8.

2.2.2.3. MOF/perovskite composites. Halide Perovskites such as $CH_3NH_3PbI_3$ and $CsPbBr_3$, in spite of some certain weaknesses including low CO_2 capturing ability, intense radiative recombination, slow reaction dynamics, and weak stability, have attracted a special attention for some of their strengths including broad absorption spectrum, elevated extinction coefficients and extensive electron-hole diffusion lengths in order to be used in the structure of MOF composites acting as photocatalyst in photochemical reactions including photocatalytic CO_2 reduction.

In 2022, Zhang et al.[141] constructed $CsPbBr_3$QDs@2D Cu-TCPP heterojunction system and utilized it as catalyst in CO_2 photochemical reduction reaction. The resulting system with the optimal amounts (20% $CsPbBr_3$ QDs) show an improvement in photocatalytic conversion of CO_2 in comparison with $CsPbBr_3$ QDs when used alone, exhibiting a yield of 287.08 μmol $g^{-1}$for CO producing during a 4 h reaction and a selectivity of 99% which exhibits an almost 3.87-fold enhancement compared to $CsPbBr_3$ QDs. The improved performance by the resulting MOF composite is attributed to better transfer of photoinduced electrons to the reaction center causing better adsorption and activation of CO_2.

The main role for increasing the efficiency of photocatalytic activity in perovskite and MOF composites can be attributed to the rapid charge transfer and separation at the interface between perovskite and MOF. This synergistic effect is well seen in the work of Zhong et al. They designed $CsPbBr_3$ QDs/UiO-66NH_2 MOF composite by combining $CsPbBr_3$ QDs and UiO-66NH_2 MOF [106]. The resulting composite shows higher photocatalytic activity for CO_2 reduction in comparison with base materials, which is attributed to good transfering of electrons between UiO-66-NH_2 and $CsPbBr_3$ QDs, vast surface area, and excellent capacity of light absorption.

Lu and coworkers have used $CH_3NH_3PbI_3$ QDs as perovskite semiconductor and constructed a group of MAPbI_3@PCN-221(Fe_x) MOF composites (x = 0–1) as catalyst for photoreduction of CO_2 from the QDs peroveskite $CH_3NH_3PbI_3$ (MAPbI_3) embedded in the holes of PCN-221 (Fe_x) through sequential deposition method [107]. They reported that the MOF composite with QDs shows a high efficiency which is 38-fold higher than that of a MOF without QDs for photocatalytic reduction reaction of CO_2 toward CO and CH_4. This excellent efficiency is ascribed to the good absorption coefficient of QDs. Also, catalytic sites of iron help to transfer electrons produced by $CH_3NH_3PbI_3$ QDs and porphyrin groups.

During recent years, some attempts have been made to construct $CsPbBr_3$ with boron imidazolate framework, ZIF, and MIL-100(Fe). For example, Zhang et al. have encapsulated $CsPbBr_3$ peroveskite within BIF-122-Co (BIF: boron imidazolate framework) to construct $CsPbBr_3$/BIF-122-Co [165]. According to their study, this new composite shows improved photocatalytic activity in comparison with base materials, which is attributable to increased stability and good charge transfer of halide proveskite as well as accelerated photoinduced charge separation all caused by BIF-122-Co. Similarly, Chen and coworkers synthesized $CsPbBr_3$@ZIF-67 and $CsPbBr_3$@ZIF-8 photocatalysts by in-situ coating of ZIF onto the surface of $CsPbBr_3$ [113]. Photoconverting CO_2 over $CsPbBr_3$@ZIF-8 and $CsPbBr_3$@ZIF-67 generated CO and CH_4 with an electron consumption rate of 15.498 and 29.630 μmol $g^{-1}h^{-1}$, respectively. Cobalt ion in these MOF composites acts as an accelerator both for charge separation and combining ZIF with $CsPbBr_3$. This in turn provides better moisture stability, CO_2 capture, and charge transfer, all leading to higher photocatalytic activity (2.66 & 1.39 times as much for $CsPbBr_3$@ZIF-67 & $CsPbBr_3$@ZIF-8) in reduction reaction of CO_2 toward methan and CO in comparison to the case when $CsPbBr_3$ is used individually.

MIL-100(Fe) is one of the ideal MOFs in the synthesis of photocatalyst composites because it has strong and complementary visible light absorption to the far red and can actively participate in the electron transfer process. Roeffaers et al.[142] constructed $CsPbBr_3$/MIL-100(Fe) in order to investigate photochemical reduction reaction under light irradiation. The resulting MOF composite with optimal ratio shows a

rate of 20.4 μmol $g^{-1}h^{-1}$ for producing CO which is almost 4 times as much as that of $CsPbBr_3$ or MIL-100(Fe) alone. This improvement is attributed to high surface area, boosted light harvesting by MIL-100(Fe), and the synergistic effect between $CsPbBr_3$ and MIL-100(Fe) giving rise to better transmission and separation of charge carriers.

2.2.2.4. Other semiconductors such as Zn_2GeO_4, Zn-MOF nanosheet, etc.. Other semiconductors such as Zn_2GeO_4 and Zn-based MOF nanosheet, thanks to their unique properties, are used in constructing the MOF composites which act as photocatalyst in photocatalytic CO_2 reduction reaction. Zn_2GeO_4 semiconductor is widely used as catalyst in photochemical reduction reaction of CO_2 due to certain properties such as highly arranged structure, light stability, and thermal stability. However, some defects such as poor absorption of CO_2 and insufficient use of solar energy restrict the application domain of this catalyst. To overcome such shortcomings, Gao and coworkers have combined Mg-MOF-74 and Zn_2GeO_4 to prepare Zn_2GeO_4/Mg-MOF-74 composite via hydrothermal method [119]. This MOF composite improves photocatalytic performance of CO_2 reduction reaction for producing CO more than 7 times as much as when the base materials are used. Such improvement is attributed to light/thermal stability of Zn_2GeO_4 as well as the strong CO_2 uptake of Mg-MOF-74 composite and its ability to inhibit photogenerated electron-hole recombination.

ZIFs have a good ability to absorb CO_2 and, in addition, due to their high thermal and chemical stability and stability in water, they provide a good synergistic effect with Zn_2GeO_4 for CO_2 photoreduction activity. Wang et al.[118] used ZIF-8 NPs to synthesize Zn_2GeO_4/ZIF-8 MOF composite through immobilizing ZIF-8 NPs on the surface area of Zn_2GeO_4 nanorods. The resulting MOF composite containing 25 wt% ZIF-8 exhibits a 3.8 times higher CO_2 absorption compared to Zn_2GeO_4 alone, leading to a 62% enhancement in reduction of CO_2 to CH_3OH in photochemical CO_2 reduction reaction. In 2018, Sun and coworkers [96] applied a system containing Zn-MOF as semiconductor photosensitizer and $[Co_2(OH)L](ClO_4)_3$ or ZIF-67 as co-catalyst. This system shows higher selectivity and efficiency (81.5%, TON for CO = 117.8) in photocatalytic CO_2 reduction reaction in comparison with Zn-MOF bulk (67.9%, TON for CO = 63.6). This improvement is attributed to promoted transfer of charge, efficient separation, and higher life span of electron-hole pairs generated by light irradiation.

2.2.2.5. MOF/carbon material composites. Carbon materials have been vastly used in construction of MOF composites for photocatalytic activities because of their large specific surface area, high thermal/chemical stability, and significant electrical conductivity. Graphitic carbon nitride (g-C_3N_4) is a specific group of carbon nitride compounds. Because of extraordinary semiconductor features of carbon nitrides, they reveal an astonishing catalytic performance in a special range of reactions, including CO_2 activation. For example, Li et al. in 2022 utilized g-C_3N_4 to construct a MOF composite appropriate for photochemical reduction of CO_2. They [166] fabricated a π-π stacking hybrid system out of g-C_3N_4 and Cu-porphyrin MOF. This system shows an excellent efficiency in photocatalytic CO_2 reduction toward ethane as a two-carbon hydrocarbon product (selectivity of 44%). Also, it shows a total selectivity of 71% for single-carbon and two-carbon hydrocarbons together (methane and ethane). C_2H_6 formation is attributed to sufficient C-C coupling produced via self-reconstruction of this system during reaction.

Most MOFs, such as ZIF-8, have a relatively wide band gap and therefore require UV light for excitation. Investigations show that the inclusion of noble metals reduces the band gap in MOF and leads to an increase in photocatalytic activity. Sayadi et al. chose copper as a metal that also problems faint absorption and renewed electron-hole recombination induced by fast light were resolved in the catalyst [143]. They constructed g-C_3N_4@Cu/ZIF-8 nanocomposite by doping ZIF-8 and copper metal on g-C_3N_4. According to the results, the hybrid product generated during photocatalytic CO_2 reduction toward methanol shows an improved efficiency equaling over 3 times as much as when ZIF-8 is used individually. The improvement in efficiency is attributed to higher absorption of CO_2 on the produced hybrid (0.12 $mmolg^{-1}$) in comparison to the base materials ZIF-8 (0.039 $mmolg^{-1}$), Cu/ZIF-8 (0.043 $mmolg^{-1}$), g-C_3N_4 (0.051$mmolg^{-1}$) which may be a consequence of the increased surface area as well as the enhanced electrical conductivity due to the suppression of photogenerated holes-electrons recombination. In another work, Zhou et al. showed that suitable functional groups in the MOF structure along with g-C_3N_4 in a composite can provide a suitable CB for high efficiency catalytic activity. They designed a series of composites from TPVT-MOFs (TPVT : 2,4,6-tris(2-(pyridin-4-yl) vinyl)-1,3,5-triazine) and g-C_3N_4 with different ratios[103]. The resulting MOF composite shows a rate of 56.4 μmol $g^{-1}h^{-1}$, which is 3.2 times higher than to g-C_3N_4 alone for reduction of CO_2 to CO and trace H_2. This increased activity is attributed to more favorable CB and VB for photoreduction reaction of CO_2, which is due to the synergy of TPVT-MOFs and g-C_3N_4. Furthermore, H_2O uptake on the surface of the MOF composite boosts CO_2 absorption, which in turn leads to greater reduction of CO_2.

In a similar work, Tahir et al. [144] constructed a g-C_3N_4-RGONH_2-MIL-125(Ti) composite (RGO: reduced graphene oxide) and utilized it as catalyst in photochemical CO_2 reduction reaction. The results denoted that CO production rate in this system is respectively 5 and 2.5 times higher than when g-C_3N_4 and g-C_3N_4-RGO are individually used as catalysts. This composite shows a rate of 383.79 μmol g^{-1} for producing CO after 4 h irradiation under visible light compared to 75.72 and 154.73 μmol g^{-1}, respectively obtained by pristine g-C_3N_4 and the g-C_3N_4-RGO. Also this composite exhibits a CH_4 evolution of 13.8 μmol $g^{-1.}$ This improvement is ascribed to the presence of RGO which constructed an effective Z-scheme bridge for the separation and transfer of charges (Fig. 22).

QDs are a class of semiconductor materials that not only can absorb strong light, but also can effectively promote the transfer of electrons generated by light by inhibiting charge recombination. Although QDs, as catalysts or cocatalysts, have the practical potential of CO_2 reduction reaction, due to their low stability, their practical use is difficult. To solve this problem, QDs are loaded onto the surface of the substrate. This approach can effectively prevent the aggregation of QDs. However, it may lead to a decrease in light absorption as well as the concentration of active sites. MOFs provide excellent support for QDs with stereoscopic scattering and well-preserved light absorption capabilities. In addition, the close contact and matching band gap between QDs and MOFs can prevent the recombination of the photogenerated electrons and holes, thereby increasing photocatalytic activity performance. For example, Li et al.[145] embedded CuO as QDs in the pores of MIL-125(Ti) MOF and used g-C_3N_4/CuO@MIL-125(Ti) composite photocatalyst for the photocatalytic reduction of CO_2. They constructed g-C_3N_4/CuO@MIL-125 (Ti) MOF composite by encapsulating CuO QDs in the holes of MIL-125 (Ti) and then combining it with g-C_3N_4. The resulting MOF composite with an optimized amount of g-C_3N_4/1%CuO@MIL-125(Ti) equaling 2.5% shows better catalytic activity in CO_2 photoreduction reaction in the presence of water, compared to base materials, and produces CO, CH_3OH, acetaldehyde, and C_2H_5OH up to 180.1, 997.2, 531.5, and 1505.7 μmol g^{-1}, respectively. Such enhanced efficiency is attributed to the presence of MIL-125(Ti) which prevents agglomeration of CuO QDs, due to its large surface area and poriferous configuration. Moreover, MIL-125(Ti) component when constructing a composite with CuO QDs stables the resulting composite in water (reducing agent) which in turn improves photochemical CO_2 reduction reaction. Also, thanks to the close liaison between CuO QDs and Ti active site in MIL-125(Ti), the generated photoelectrons in MIL-125(Ti) and g-C_3N_4 can be transferred to the CuO QDs, and such transfer in turn contributes to the improvement of photochemical CO_2 reduction reaction.

As a good semiconductor photocatalyst, g-C_3N_4 has potential application in the photocatalytic reduction of CO_2. To improve its practical

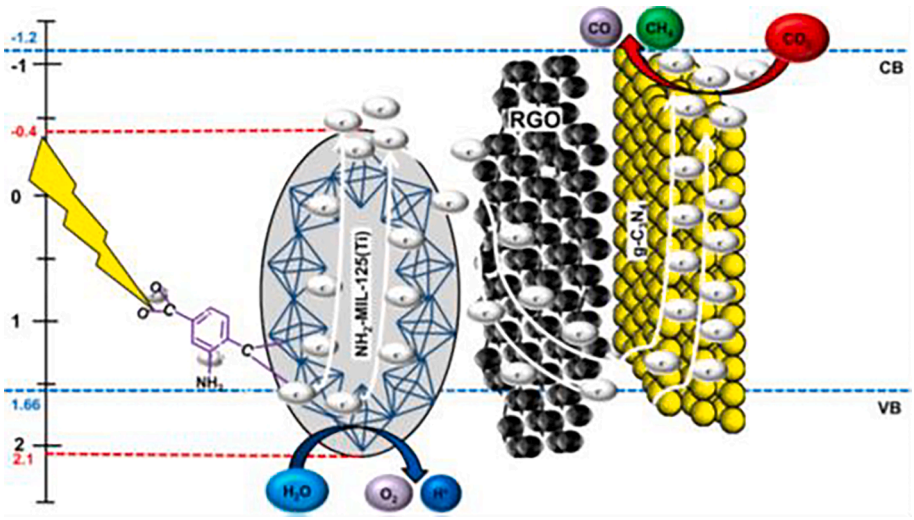

Fig. 22. Formation of a Z-scheme heterojunction over the g-C_3N_4-RGONH_2-MIL-125(Ti) nanocomposite under visible light irradiation [144]. With permission from Elsevier, copyright 2021.

application and further increase its photocatalytic performance under visible light, various methods such as physical and chemical modifications have been proposed by researchers to accelerate the generation of electrons and holes. For example, Zhang et al.[154] constructed g-C_3N_4/ZIF-67 MOF composite and utilized it as photocatalyst in photoelectrochemical CO_2 reduction. In photoelectrochemical CO_2 reduction to ethanol, the resulting MOF composite shows an enhanced efficiency three times as much as when g-C_3N_4 is used individually. This improvement is ascribed to synergy between g-C_3N_4 and ZIF-67 which enlarges the electron-hole separation.

There are also several attempts to form MOF composites by synthesizing Co, Zn and Zr with carbon material to be used in photochemical reduction of CO_2. For example, Wang and coworkers,[146] prepared Co-MOF/g-C_3N_4 MOF composite and analyzed its influence on photocatalytic CO_2 reduction reaction. The resulting MOF composite showed an improved photocatalytic activity being almost twice as much as when g-C_3N_4 is individually utilized in photocatalytic reduction of CO_2 with a CO and CH_4 production rate of 6.75 and 5.47 μmol $g^{-1}h^{-1}$, respectively. This enhancement is ascribed to the presence of Co-MOF component in the resulting composite which not only causes a wide spectrum of visible light is absorbed, but also improves charge separation. Also, Wang and coworkers constructed Co-ZIF-9/g-C_3N_4 MOF composite from Co-ZIF-9 and g-C_3N_4 [147]. The resulting MOF composite shows excellent photocatalytic efficiency in the CO_2 reduction than base materials, without any alteration in the structure of g-C_3N_4 and Co-ZIF-9 after the reaction. This higher activity is attributed to Co-ZIF-9 that increases CO_2 absorption and improves charge separation. In another work, BIF-20 as one of the types of ZIFs has a good potential for CO_2 storage and separation. B-H sites of it are active centers for the photocatalytic reaction of CO_2 reduction, therefore, by equipping the pore surfaces with B-H sites in the MOF structure, a suitable space for the photocatalytic reaction can be created. However, the absorption of BIF-20 in the visible light region is limited due to its wide band gap. To increase the photocatalytic efficiency, Xu et al. used the synergistic effect of MOF and g-C_3N_4. They prepared BIF-20@g-C_3N_4 from BIF-20 and g-C_3N_4 by electrostatic self–assembly method [105]. The resulting MOF composite shows an improvement in photocatalytic CO_2 reduction activity compared to g-C_3N_4 nanosheet alone, which is equal to a 9.7-fold enhancement in CH_4 evolution rate (15.524 μmol $g^{-1}h^{-1}$) and a 9.84-fold enhancement in CO production rate (53.869 μmol $g^{-1}h^{-1}$) that is attributed to the B-H bond which traps photoexcited electrons, inhibits recombination of charge carriers, and increases CO_2 absorption.

Another example of MOF/g-C_3N_4 composite was synthesized by Zhang et al.[148] in which the MOF structural unit of NH_x-Zr-O as active group plays the main role in MOF. NH_2-UiO-66/g-C_3N_4 MOF composite from holey g-C_3N_4 and NH_2-UiO-66 with rich amino group (–NH_2) through a facile in situ growth route was synthesized. The resulting MOF composite with an optimized component ratio (35% of which is the MOF component) shows an improved catalytic activity in photochemical CO_2 reduction reaction toward CO (31.6 μmol $g^{-1}h^{-1}$) which shows double and triple enhancement respectively compared to g-C_3N and NH_2-UiO-66 alone. This improved activity is attributed to the formation of NHx-Zr-O which accelerates the separation and transfer of charge carriers.

Furthermore, Zhong et al. used ultrathin g-C_3N_4 in the preparation of composite to increase the photocatalytic efficiency. They constructed a series of ZPUCN-x composites (Zr-PMOFs/ultrathin g-C_3N_4) from Zr-PMOFs and ultrathin g-C_3N_4 by in situ solvothermal method,[122] in which zirconium MOF is surrounded by ultrathin carbon nitride causing an interaction between them. This interaction facilitates separation and transfer of photoexcited charge carriers on the resulting MOF composite. The optimized composite (x = 3) leads to a CO yield of 5.05 μmol $g^{-1}h^{-1}$ during CO_2 reduction, which is 2.2 and 3.2 times higher than the analogous rates for Zr-PMOFs and bare g-C_3N_4, respectively.

ZIF-8 has two unique properties that make it suitable for the fabrication of ZIF-8/semiconductor composites for photocatalytic CO_2 reduction. One feature is the transparency of ZIF-8. Therefore, the light harvesting capacity in the composite is increased. Another feature is the good adsorption selectivity in ZIF-8. For the photocatalytic reduction reaction of CO_2, it is very important that the photocatalytic system can efficiently absorb the reactant CO_2 but not tend to the reduction products such as CH_4, CH_3OH. In 2017, Liu et al.[149] used ZIF-8 MOF and C_3N_4 to produce C_3N_4@ZIF-8 composite and subsequently applied it as catalyst in photochemical CO_2 reduction to gain methanol. The resulting MOF composite exhibits a roughly triple increase in photocatalytic CH_3OH production efficiency compared to when the bulk C_3N_4 is used individually. This improvement is attributed to high adsorption of CO_2 by transparent ZIF-8 and the boosted efficiency for charge separation caused by C_3N_4.

The composites made up of MOFs and graphene quantum dots (GQD) were designed by Ding and coworkers. They prepared environmentally friendly (Zn-Bim-His-1@GQD) MOF composite by binding the GQDs into the cavities of Zn-Bim-His MOF composite [112]. The resulting MOF composite (Zn-Bim-His-1@GQDs) ameliorated photocatalytic performance for CO_2 reduction compared to base materials with evolution rates of 20.9 and 3.7 μmol $h^{-1}g^{-1}$ for CH_4 and CO, respectively. This enhanced activity is attributed to the synergistic effect between Zn-Bim-

His-1 and GQDs, prevention of photogenerated charges recombination by Zn-Bim-His-1@GQDs, and the availability of active sites enriched on the surface of MOF composite.

Graphene carbon nitride quantum dots (g-CNQDs) are used to improve photocatalytic properties during targeted construction of MOF composites. This material, when combined with MOFs, gives rise to better electron-hole separation, and therefore improves the electronic properties of the product. Han et al.[150] constructed g-CNQDs/PMOF composite [PMOF: porphyyrin MOF] and applied it in photochemical CO_2 reduction reaction. The resulting MOF composite shows a 2.34-fold improvement in the CO production rate (31.6 μmol $g^{-1}h^{-1}$) and a 6.02-fold improvement in the CH_4 production rate (6.86 μmol $g^{-1}h^{-1}$) compared to when PMOF is used individually. This improvement in efficiency and selectivity is attributed to good separation of electrons-holes and long-lived electrons confined at cobalt centers, both owing to g-CNQDs component.

Saikia et al.[151] constructed a binary MOF composite from g-CNQDs and Zr(IV)-based MOF composite (g-CNQDs@MOF) exposed to regular LED lamps. In the resulting MOF composite, g-CNQDs acts as a co-catalyst improving electron-hole separation by extending the lifespan of photogenerated charge carriers on the MOF composite surface. Therefore, these extra electrons create more active sites on the surface of composite, leading to a highly efficient optional reduction of CO_2 to methanol while no other carbon or gas product is generated.

Moreover, some attempts have been made to fabricate CNT composites. For example, Yan and Yang constructed UiO-66-NH_2/CNTs with different ratios of MOF and CNTs, through loading UiO-66-NH_2 on the surface of CNTs via hydrothermal method [152]. This MOF composite with optimal amount (2 wt% CNTs), when used as a photocatalyst for CO_2RR, provides optimum yields of 28.8 μmol and 63.1% for HCOOH exposed to visible light irradiation for 4 h. This efficiency is attributed to high specific surface area provided by UiO-66-NH_2/CNTs (1.5 times as much as UiO-66-NH_2 alone) which results in an increased absorption of CO_2 and an efficient inhibition of photogenerated electron–hole recombination by CNTs.

RGO has unique properties such as good mobility of charge carriers and good optical transparency and with two-dimensional structure can act as an excellent charge transfer conductor [167]. Zhao et al. applied RGO to synthesize RGO/NH_2-MIL-125(Ti) [117,168] and utilized the resulting MOF composite in photochemical CO_2 reduction. The generated products are CH_3OH and $HCOOCH_3$ and the resulting MOF composite exhibits very good stability. Compositing NH_2-MIL-125(Ti) with RGO reduces the agglomeration of RGO and enhances photogenerated charge separation.

Also, Do et al.[123] constructed Al-PMOF/NH_2-RGO from a porphyrin MOF Al-PMOF and amine-functionalized graphene (NH_2-rGO) and used it as catalyst in photocatalytic CO_2 reduction reaction. The results showed an improvement in CO_2 photoreduction towards producing formate compared to base materials. Formate production rate stood at 685.6 μmol g_{cat}^{-1} h^{-1} yielding a selectivity of approximately 100%. This improvement is attributed to the decreased band gap in graphene-porphyrin base MOF and also suppressing the potogenerated electron-holes recombination. On the other hand, Peng et al.[94] constructed a system with a composite thin film consisting of the 2D/2D RGO/Ni_3HITP_2 heterostructure as the cocatalyst, $[Ru(bpy)_3]^{+2}$ as the photosensitizer, and TEOA as electrondonor. The resulting system shows higher performance in photocatalytic CO_2 reduction reaction toward CO in comparison with base materials. This improvement is attributed to good charge immigration within two-dimensional heterostructure, and higher electron density enhanced at the isolated Ni-N_4 sites by the electrostatic charge transfer.

Composite photocatalytic systems are classified into type-II and Z-scheme types based on the charge transfer pathway produced by light. The redox efficiency of photoinduced positive electrons and holes in the type II hybrid is reduced due to the migration of photoinduced electrons to the more positive CB and the migration of photoinduced holes to the more negative VB, respectively. While, in the Z-scheme, the composite has a good separation of photoinduced charges, and the redox process is carried out well. For instance, In 2019, Liu et al.[110] demonstrated that constructing a Z-scheme heterojunction is a practical method to separate photogenerated electron-holes and promote the activity of the semiconductor photocatalyst. They constructed O-ZnO/RGO/UiO-66-NH_2 Z-scheme heterojunction and used it as catalyst in photocatalytic CO_2 reduction. The results indicate that the above system shows a better catalytic activity than O-ZnO/UiO-66-NH_2 and ZnO/rGO/UiO-66-NH_2 in photocatalytic reduction of CO_2 toward CH_3OH and HCOOH with the yields of 34.83 and 6.41 μmol $g^{-1}h^{-1}$ respectively.

Graphene (G) is a zero-gap semiconductor which is vastly used in photochemical reactions. For instance, Yan et al. constructed a ternary MOF composite via the hydrothermal method by modifying MOF of UiO-66-NH_2 with Au NPs and G [108]. The new MOF composite exhibits higher photocatalytic activity (49.9 μmol) and also provides higher selectivity (80.9%) than those of UiO-66-NH_2/G (71.65%) and UiO-66-NH_2 alone (38.3%) in CO_2 photoreduction to products like H_2 and HCOOH. Such high performance is attributed to the presence of Au NPs for their high absorption of light. Also, G prevents recombining the electron-hole pairs and improves the dispersibility of UiO-66-NH_2, providing more active sites for capturing CO_2. In another study, UiO-66-NH_2/G MOF composite was synthesized by Li et al.[109] via microwave-assisted in situ assembly. They applied the new compound as catalyst in photochemical CO_2 reduction. The resulting MOF composite exhibits higher activity and selectivity in producing formic acid from CO_2 compared to UiO-66-NH_2. This better efficiency is attributed to several factors including the tight junctions between UiO-66-NH_2 and the surface of G, small size of MOF crystal particles, high capacity of the resulting MOF composite to adsorb CO_2, and appropriate distribution of UiO-66-NH_2 on the surface of G.

Silicon carbide (SiC) is another carbon material recognized as semiconductors. For CO_2 reduction, most conventional photocatalytic routes are carried out in a liquid phase system, while the low solubility of CO_2 limits its large-scale application. In contrast, in gas-solid phase conditions, CO_2 molecules can have direct contact with the catalyst, which is more suitable for practical applications. The interface coupling plays an important role in the transmission of optical carriers. Conventional thermochemical methods, such as high-temperature hydrothermal and calcination, improve surface coupling. However, MOFs may lose their structure under the conditions of these synthetic methods. In contrast, the liquid phase microwave method with mild conditions produces strong coupling at the interface of the composite while maintaining the structure of MOFs. This method is based on microwave absorbent materials to produce super-hot surfaces in a very short time. Xiao et al.[135] selected SiC as a strong microwave absorbent for the microwave super-hot spot operation to drive the growth of MOF nanocrystals. They synthesized NH_2-UiO-66/SiC MOF composite from SiC and NH_2-UiO-66 by microwave according to the super-hot spot heating mechanism on SiC. The resulting MOF composite showed higher efficiency for photoreduction of CO_2 to CO with a rate of 7.30 μmol$g^{-1}h^{-1}$ which is 5 times as much as higher compared to NH_2-UiO-66 as photocatalyst. This improvement can be ascribed to the enhanced capacity to absorb CO_2 molecules due to higher specific surface area being available, as well as to better charge transfer and separation of photogenerated carriers leading to better utilization of electrons.

The transformation of MOFs into ultrathin MOL films can accelerate mass transfer/electron transfer and facilitate access to active sites, which is crucial for efficient catalytic activities. In 2021, Zhang and coworkers constructed Co-MOL@GO MOF composite from Co-MOL and GO by facile template strategy [98]. The resulting MOF composite [Co-MOL@GO] exhibits an improvement for CO_2 photoreduction with a total CO yield of 3133 mmolg^{-1} and CO selectivity of 95%, ca. 34 times higher than that of Co-MOL. This improvement in efficiency is attributed to better charge transfer between two components of the resulting MOF, which arises from synergistic effect between them.

Also, there is a successful attempt for the synthesis of UiO-66/CNNS from carbon nitride nanosheets (CNNS) and UiO-66, reported by Ye and coworkers. They constructed UiO-66/CNNS composite through electrostatic self-assembly method from UiO-66 and nanosized carbon nitride nanosheets [121]. The resulting MOF composite shows higher photocatalytic activity for the CO_2 conversion than CNNS alone (a CO evolution rate of 9.9 μmol g_{CN}^{-1} h^{-1}). This improvement is attributed to the large surface area and strong CO_2 capture ability caused by the presence of UiO-66. They proposed a mechanism according to which photoexcited electrons from CNNS can move toward UiO-66, restraining electron–hole pair recombination. As a result, long-lived electrons are available to reduce the CO_2 molecules absorbed in UiO-66.

Carbon dots (CDs) are a new class of fluoresent small-carbon nanomaterials with particle sizes of less than 10 nm. This group of materials has a vast range of applications including photochemical CO_2 reduction reaction. In 2020, Li et al. constructed CD-decorated and CD-embedded NH_2-UiO-66 particles and investigated the effects of these two states of CDs on the photocatalytic reduction of CO_2 [68]. They found out that CDs when embedded into NH_2-UiO-66 improve the photocatalytic activity for CO_2 conversion, because in this new state the charges are transformed and separated rather better than when CDs are decorated on NH_2-UiO-66.

2.2.3. MOF composites with host–guest interactions

Another type of MOF composites is formed by encapsulating certain guests such as molecular catalysts, molecular photosensitizers (PSs), and other functional species in the cavities of the host MOF. Consequently, the interaction between host and guest, both charge transfer and light harvesting are better performed, and it finally improves the photocatalytic activity of resulting MOF composites. When MOF has cavities with appropriate sizes, one may embed simultaneously both catalyst molecules and PS molecules in the cavities and consequently increase the efficiency of the reaction. For example, Warnan and coworkers synthesized a supramolecule from the photocatalyst *fac*-ReBr$(CO)_3$(4,4dcbpy) (dcbpy = dicarboxy-2,2′-bipyridine) and Ru$(bpy)_2$(5,5′-dcbpy)Cl_2 (bpy = 2,2′-bipyridine) as PS and the MOF MIL-101-NH_2(Al) [169]. They found that activity and stability of the formed supramolecule is related to the ratio between catalyst and PS molecules. When the ratio of catalyst molecules to PS molecules is 7.9, the catalytic properties of the supramolecule in the photocatalytic reduction of CO_2 to CO greatly improve and the final accumulation with a TON value of 18 after 4 h.

In another report, Peng et al. designed a photocatalytic system with $Ni_3(HITP)_2$ (HITP =-hexaaminotriphenylene) 2D MOF in the form of exfoliated nanosheets as co-catalyst, $[Ru(bpy)_3]^{2+}$ as PS, and TEOA as electron donor [170] to investigate photochemical conversion of CO_2 to CO. The resulting MOF composite exhibited high efficiency for photoreduction of CO_2 to CO in comparison with base materials (CO yield rate of 3.45x10^4 μmol$g^{-1}h^{-1}$ with high selectivity of 97% for over 3 h). This improvement is attributable to a synergic effect resulting from high conductivity and highly active Ni-N4 catalytic properties accompanying the above conductive 2D MOF.

Transition metal complexes are one of the light-harvesting materials that have the potential to convert solar energy into electricity or chemical fuels through the formation of long-lived charge decoupled excited states. Lin and coworkers prepared a MOF composite comprising cuprous PS and cobalt or rhenium molecular catalysts for investigating photochemical conversion of CO_2 to CO [171]. This MOF composite shows improvement in the photochemical reduction of CO_2 to CO displaying a TON of 1328. This improvement is attributed to the increased stability of PS and catalyst molecules as well as an increased electron transfer between them.

Ru- and Rh-polypyridyl complexes are also considered as good PSs. In this context, Drazniek et al. utilized MIL-101-NH_2 MOF as nanoreactor, and co-confined catalyst molecule and PS into MOF cavities. They [172] prepared Rh-Ru@MIL-101-NH_2 composite by immobilizing the molecular catalyst $[Cp^*Rh(4,4'\text{-bpydc})]^{2+}$ and a molecular PS $[Ru(bpy)_2(4,4'\text{-bpydc})]^{2+}$ (bpydc : bipyridinedicarboxylic acid) into the MIL-101-NH_2 via post-synthetic impregnation. The resulting MOF composite shows higher selectivity and efficiency (a rate of 132.2 $mmolg^{-1}h^{-1}$) toward formate as an exclusive product, compared to when catalyst molecule is used individually.

Furthermore, depending on the size of the pores of MOF composite, the catalyst molecule and the PS molecule can be either embedded inside cavity or anchored on the outside surface of the MOF composite. For example, Warnan and coworkers [173] have investigated a MOF isoreticular series UiO-66, UiO-67, and UiO-68 in terms of host-guest interaction with the molecular catalyst $[ReBr(CO)_3(4,4'\text{-dcbpy})]$ and the molecular PS $[Ru(bpy)_2(5,5'\text{-dcbpy})]Cl_2$. Accordingly, UiO-66 only allowed for $[ReBr(CO)_3(4,4'\text{-dcbpy})]$ and $[Ru(bpy)_2(5,5'\text{-dcbpy})]Cl_2$ anchoring to occur on the particle surfaces; UiO-67 allowed $[ReBr(CO)_3(4,4'\text{-dcbpy})]$ to reside inside the cavities, and $[Ru(bpy)_2(5,5'\text{-dcbpy})]Cl_2$ to anchor on the outer surface; while UiO-68 allowed both $[ReBr(CO)_3(4,4'\text{-dcbpy})]$ and $[Ru(bpy)_2(5,5'\text{-dcbpy})]Cl_2$ to reside inside the cavities.

In this way, a variety of photocatalysts with different activities and stabilities are formed by this MOF composite series. Such difference is caused by the ratio between catalyst molecules and PS. Coupling of PSs with MOFs is a very common method to kinetically improve CO_2 photoreduction as well [174]. In 2014, Wang and coworkers coupled Co-ZIF-9 with a ruthenium-based PS, $[Ru(bpy)_3]Cl_2{\cdot}6H_2O$ for enhancing photoreduction of CO_2 to CO [175]. This mixture improves the photocatalytic reduction of CO_2 compared to PS only. This improvement is attributed to better charge transfer and high absorption of CO_2 by Co-ZIF-9. An analogous system was designed in which ZIF-67 and ruthenium semisentisizer collaborate, and its effect on photocatalytic conversion of CO_2 to CO was investigated [175,176]. It was found that, under optimum conditions, the efficiency of CO_2 photocatalytic reduction shows a significant improvement compared to base materials.

Similarly, Peng and coworkers invented another composite by using ZIF-67 as catalyst in photochemical CO_2 reduction. They constructed ZIF-67@PPy (PPy = polypyrrole) composite from polymerization of ZIF-67 with cubic crystal morphology [177]. The resulting MOF composite shows a roughly billion times enhancement in conductivity as well as higher stability, porosity and surface area in comparison with base materials, which improves the activity of photocatalytic CO_2 reduction reaction (59.42 μmol of CO yield during a 4 h test and a CO evolution rate of 1.49×10^4 μmol h^{-1} g^{-1}). This improvement is attributed to the synergistic effect between ZIF-67 and PPy and good PPy-mediated electron harvesting.

Liao et al. developed a particular kind of MOF composite formed by the electrostatic force between MOF as anion and PS as cation. They constructed Ru@Cu-HHTP (HHTP: 2,3,6,7,10,11-hexahydroxytriphenylene) MOF composite from an anionic MOF Cu-HHTP as the host and a cationic PS $[Ru(phen)_3]^{2+}$ (phen: 1,10-phenanthroline) as the guest [178]. Due to the electrostatic interaction between PS and Cu-HHTP, the PSs are placed in Cu-HHTP cavities (Fig. 23). This system shows high efficiency in photocatalytic conversion of CO_2 to CO (CO evolution rate of 130 mmol $g^{-1}h^{-1}$ with a selectivity of 92.9% under the laboratory light and CO evolution rate of 69.5 mmol $g^{-1}h^{-1}$ with a selectivity of 91.3% under natural solar light) which is attributed to better charge transfer between its two components.

Another method to enhance the efficiency of photocatalysts for the reduction of CO_2 is immobilizing POMs inside the cavities of MOFs and using PS, simultaneously. For example, Draznieks et al.[179] designed a system in which a Keggin-type POM $PW_{12}O_4O_3^-$ and the catalytic complex $Cp^*Rh(bpydc)Cl_2$ (bpydc: 2,2′-bipyridine-5,5′-dicarboxylic acid) were placed inside the cavities of UiO-67. The resulting composite $[PW_{12}$,Cp*Rh)@UiO-67] improves the efficiency in photocatalytic reduction of CO_2 to formate compared to the system lacking POM [Cp*Rh@UiO-67]. Such improvement is attributed to POM which plays the role of a proton relay.

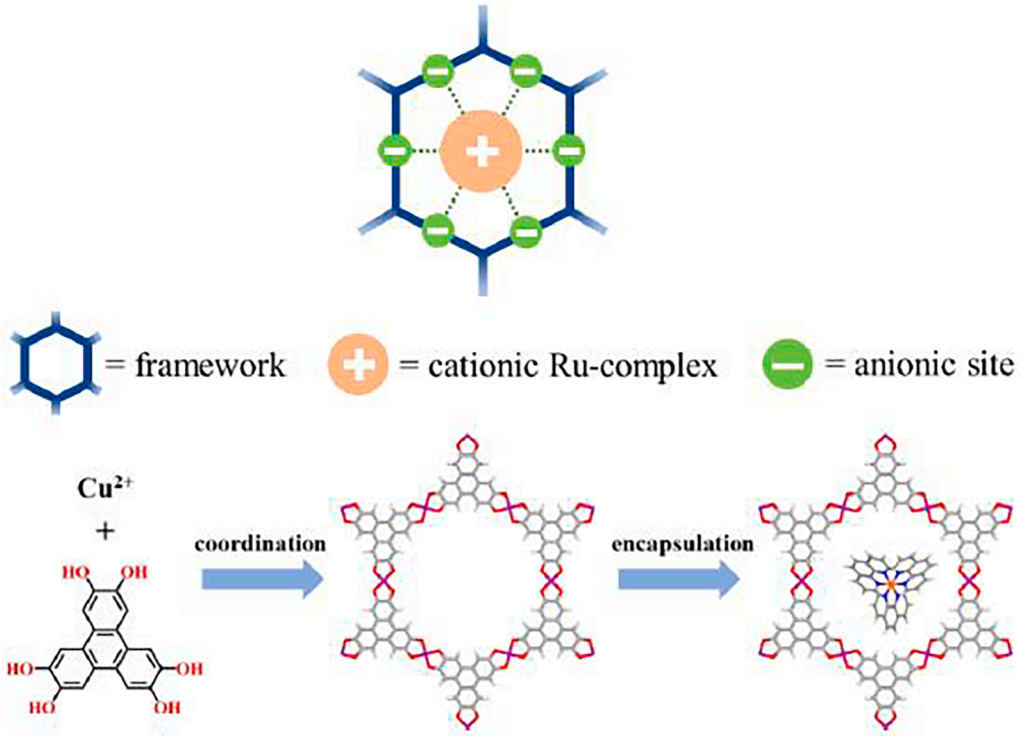

Fig. 23. Electrostatic interaction between photosensitizer $[Ru(phen)_3]^{2+}$ and MOF and illustration of the synthetic path forming Cu-HHTP and subsequent encapsulation of $[Ru(phen)_3]^{2+}$ [178]. With permission from the American Chemical Society, copyright 2021.

Applying the composites of catalysts and MOFs enhances their catalytic properties in photochemical CO_2 reduction reaction. For instance, in 2022, Hupp et al. constructed the MOF composite [Fe-TCPP@NU-1000] by grafting NU-1000 to the catalyst molecule tetra(4-carboxyphenyl) porphyrin iron(III)chloride (Fe-TCPP) [180]. In this system a self-contained photocatalyst was formed by pyrene linker absorbing the electrons and transferring them to the porphyrin catalyst. Such procedure caused an improvement in the photocatalytic activity during CO_2 reduction in comparison with most other iron porphyrin-based catalysts (TON: 22 and TOF: 11 h^{-1} for CO production in 2 h illumination at 1390 nm). Finally, leaching of grafted iron-porphyrin from the resulting MOF composite caused a decrease in catalytic activity.

Similarly, Jin and Kong constructed Ni@Ru-UiO-67 MOF composite from the molecular catalyst $[Ni^{II}(bpet)(H_2O)_2]$ (bpet: 1,2-bis((pyridin-2-ylmethyl)thio)ethane) and Ru-UiO-67 MOF composite [181]. They demonstrated that the resulting MOF composite improves photocatalytic conversion of CO_2 to CO yielding a TON of 581 and a significant selectivity of 99 % after 20 h. Photoluminescence assessments demonstrated a smooth immigration of electrons from the excited Ru-MOFs toward the encapsulated Ni(II) complex, which was essential for the superior performance of Ni@Ru-UiO-67. Similar types of MOF composites have been reported in which they are utilized as catalyst in photochemical CO_2 reduction reactions, consisting of MOFs and Ru catalyst. For example, in 2016, Kitagawa and coworkers synthesized PCP-Ru composite bearing a Ru-Co complex, through post-synthetic exchange (PSE) method [182]. In CO_2 photochemical reduction, the PCP-Ru composite produced CO, HCOOH and H_2 and showed the highest activity in conversion of CO_2 to CO among similar composites. This improvement in activity is attributed to the synergistic effect between the gas adsorption properties of a PCP and the catalytic properties of a molecular catalyst.

Sometimes incorporation of a catalytic molecule in MOFs by post-synthetic modification on the ligand may lead to undesirable interactions between the metal complex and the solid surface, which reduces the efficiency of molecular catalysts. The direct preparation of metal complexes using the substrate as a solid ligand is a suitable strategy to increase catalytic activity. In this aspect, Sun et al.[183] constructed MOF-253-$Ru(CO)_2Cl_2$ by immobilizing active Ru carbonyl complex into MOF-253, and then investigated the catalytic effect of the resulting system on photocatalytic CO_2 reduction toward formate. The amount of formate acquired is 12 times as much as when the individual materials are used as catalysts. This improvement is attributed to higher visible light adsorption and a greater number of photogenerated electrons transmitted from ligands to the active sites of MOF-253.

Similarly, MOF composites have been synthesized from UiO-67 MOF and various catalysts, to serve as catalyst in photochemical CO_2 reduction reaction to acquire formic acid. As an instance, Chamber et al.[37] constructed Cp*Rh@UiO-67 through reacting UiO-67 with Cp*Rh(bpydc)Cl_2 complex (bpydc = 2,2′-bipyridine-5,5′-dicarboxylic acid) in deionized water at room temperature for 24 h (Fig. 24), and applied it in the optimized state (when catalyst molecule comprises 10% of the resulting system) in photochemical CO_2 reduction reaction to afford formate as the main product with high efficiency. This significant efficiency arises from the large surface area provided by MOF component for the catalyst.

The postsynthetic metalation of a MOF including metal-chelating ligands is another method for synthesis of the catalytic composites. In 2015, Cohen et al.[184] used this method to prepare UiO-67-Mn(bpy)$(CO)_3Br$ system by incorporating a molecular catalyst into a MOF platform. This system shows improvement in CO_2 photoreduction in comparison with UiO-67 alone and homogeneous reference systems (TON for formate: 50 and 110 respectively after 4 and 18 h). Such improvement is attributed to high CO_2 adsorption on UiO-67-Mn(bpy)$(CO)_3Br$ and isolated catalytic sites provided by the struts of the framework, as well as to the enhanced stability thanks to the structure of Mn-MOF.

Cobalt oxide species (CoO_X) is a catalyst that has been widely used for CO_2 to CO conversion and has certain advantages such as low price and high stability. Hence, by confining CoO_X NPs in the channels of the MOF as a co-catalytic system one may raise the efficiency of CoO_X in

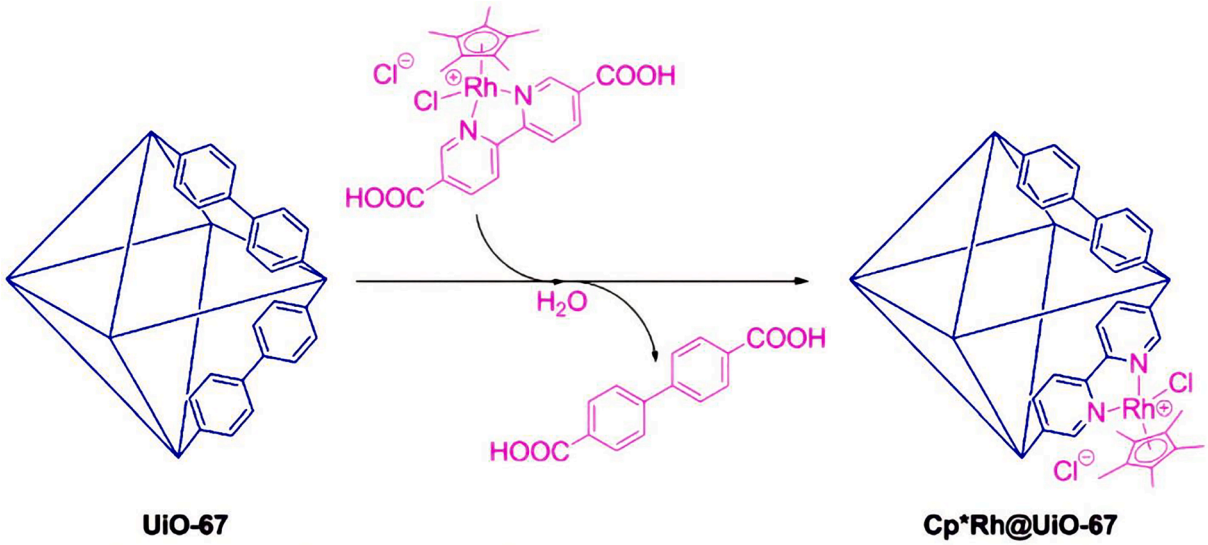

Fig. 24. Constructing Cp*Rh@UiO-67 from UiO-67 and rhodium complex catalyst through post-synthetic linker exchange [37]. With permission from the Wiley-VCH, copyright 2015.

photochemical CO_2 reduction reaction. For example, Wang et al. designed a novel MOF composite [185] namely CoO_x/MIL-101(Cr) to improve CO_2 photoreduction. This MOF composite shows higher activity for photoreduction of CO_2 to CO in comparison with bare CoO_x and MIL-101(Cr) (with producing of 28.7 μmol·h^{-1} CO).

Ir single atoms are active centers to promote activation of gas molecules such as CO_2 and produce liquid fuels under visible light and mild conditions. Wang and coworkers [186] reported that Ir single atoms as catalytic centers anchored on the metal nodes of the gas-permeable organic framework membranes could improve the electronic structure of such photocatalysts and make them more efficient in photocatalytic CO_2 reduction reactions. For example, Iridium single atom being anchored on the metal node of activated NH_2-UiO-66 advances CO_2 reduction reaction toward the formic acid product with an AQE of 2.51% at 420 nm on the gas liquid–solid reaction interface.

Bi_2MoO_6 is an excellent photocatalyst and solar-energy-conversion material for degradation of organic compounds such as CO_2 under visible-light irradiation [153,187]. In 2022, Cai et al.[188] constructed Ce-MOF/Bi_2MoO_6 heterostructure by intense contact between two components via the electron coupled structure, and then applied it as catalyst in photochemical CO_2 reduction reaction. The new system exhibited a higher efficiency in comparison with Ce-MOF and Bi_2MoO_6 when each component is used individually. The optimized photocatalyst produces CH_4, CH_3OH, and HCOOH with evolution rates of 113.87, 4.59, and 73.48 μmol $g^{-1}h^{-1}$, respectively. This improvement is attributed to the high surface area provided by Ce-MOF and efficient electron transfer by Bi_2MoO_6. Also, enhanced interfacial interaction appears to increase the separation and transfer of photogenerated charge carriers. In another work, copper, thanks to its amphoteric character as well as cheap, appears to be a good applicant to be coupled with ZIF-8. Therefore, the compounds of Cu/ZIF-8 are expected to exhibit improved photocatalytic reactions toward producing methanol. In 2018, Goyal et al.[189] prepared Cu/ZIF-8 MOF composite via a hydrothermal method and employed in photochemical reduction of CO_2 to methanol. The resulting system with optimal ratio shows enhancement in photocatalytic activity in comparison with base materials (a methanol yield of 35.82 μmol g^{-1} L^{-1} after 6 h). This improved activity is attributed to the solvent effect in the synthesis method and the amount of Cu loading over ZIF-8.

Recently, Roy et al.[190] constructed Ce/Ti-based bimetallic 2-aminoterephthalate MOF and Ce-terephthalate MOF, and then applied them as catalysts in photocatalytic CO_2 reduction. The authors indicated that Ce/Ti-based bimetallic 2-aminoterephthalate MOF (UiO-66) exhibits better efficiency in photocatalytic CO_2 reduction toward acetic acid in comparison with Ce-terephthalate MOF. The H_2 generation was investigated for the pristine Ce-terephthalate MOF and the photocatalyst $Ce_{0.5}Ti_{0.5}$-MOF- NH_2 (Fig. 25). Such better efficiency arises from higher flux of photogenerated electron-holes and their recombination at a lower rate, higher capability to adsorb CO_2 as well as an appropriate band gap.

Generally, the comparison of electroreduction and photoreduction of CO_2 shows that both methods have some advantages and limitations. In photoreduction procedure, there are few MOFs able to promote photoreduction reaction efficiently, because most MOFs are not good electron conductors and most MOFs show a poor performance in the photocatalytic reaction, which is often due to the poor absorption of visible light and the absence of active electrons. On the positive side, photoreduction uses the free and accessible light source of the sun to excite electrons and, photoreactors are relatively simple systems. In comparison, electroreduction requires a battery power source to carry out the process. In addition, the selectivity in photoreduction is better than in

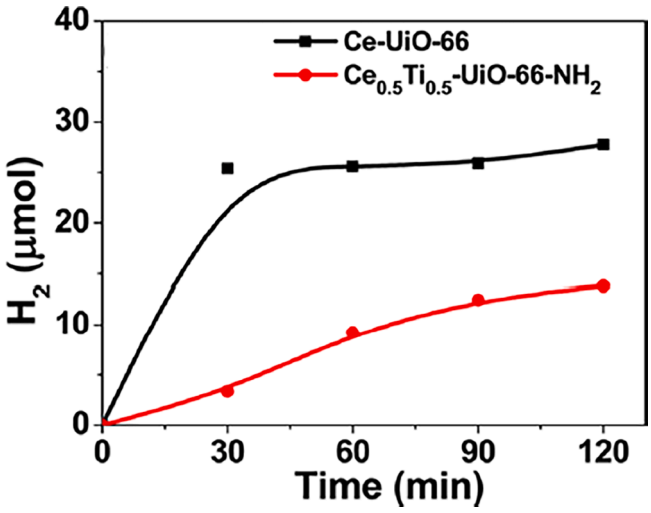

Fig. 25. Photocatalytic H_2 process against the time for the pristine Ce-UiO-66 and $Ce_{0.5}Ti_{0.5}$UiO-66-NH_2 [190]. With permission from American Chemical Society, Copyright 2022.

electroreduction.

The list of some MOF composites with host-guest interaction for photocatalysis application of CO_2 reduction reaction is summarized in Table 4.

2.3. Photoelectroreduction of CO_2 by MOF composites

Photoelectroreduction is another method for CO_2 reduction to value-added products. This method is like electroreduction in terms of the experimental setup but instead of normal conducting electrodes used in electroreduction it applies semiconductor electrodes. Thanks to the solar energy entered the story, this method decreases electricity consumption in comparison with electroreduction method. Photoelectroreduction can reach higher efficiency in comparison with photoreduction, and it is attributable to the ability of external bias voltage to shift the partition between photogenerated electrons and holes as a major obstruction which restricts the photocatalytic efficiency. An ordinary photoelectrochemical reduction system has a semiconductor which absorbs light to boost the reaction on the electrode surfaces. Fig. 26 illustrates three typical bipartite photoelectrochemical units. Semiconductors may be utilized either as photocathode (Fig. 26A) or photoanode (Fig. 26B). Both electrodes can also benefit from semiconductor photocatalysts (Fig. 26C) [3].

Jain et al.[191] reported the conversion of CO_2 gas into two-carbon alcohol (ethanol) by photoelectroreduction method. They applied a ternary composite containing Cu_xO/GO and Cu-MOF as photocathode. This MOF composite delivered excellent efficiency in CO_2 reduction with the maximum ethanol yield of 162 uMcm^{-2} after 4 h at potential of −0.5 V vs Ag/AgCl. This excellent efficiency is attributed to good charge separation as well as high mobility and density of photogenerated charge carriers, leading to more availability of photoelectrons for CO_2 reduction. Moreover, DFT calculation indicates that the absorption of CO_2 on Cu atoms occurs vertically, which in turn enhances CO_2 absorption on the MOF composite surface due to the proximity of CO_2 molecules to the surface.

Two-dimensional nanosheets can have efficient catalytic activity for CO_2 reduction due to their attractive features such as large surface area and regular porosity. However, major reduction products such as CO or formic acid are produced resulting from the transfer of one or two electrons. Cheng et al.[192] used CuS NPs as additive to produce valuable reduced products such as hydrocarbons with high selectivity. They anchored CuS NPs on Cu-MOF nanosheet (Cu-porphyrin) and applied the resulting system as cathode in photoelectrochemical reduction of CO_2. The results indicate that this catalyst can form ethanol with a high selectivity and efficiency. Total conversion rate of carbon atom in photoelectroreduction of CO_2 over this cathode catalyst is 5174 nmolh^{-1}cm^{-2} with a selectivity of 74.4% for ethane product. CuS by amplifying the binding energy to adsorb CO* in S atoms (1.5 eV) enhances the catalytic activity of the MOF composite.

TiO_2 is another widely used semiconductor employed in the photoelectrocatalysis of CO_2 reduction reaction. This semiconductor under radiation according to the energy of the band gap can produce e^-/h^+ pairs that have an acceptable separation under the potential created at the interface between the electrode (semiconductor) and the electrolyte. For instance, in 2018, Cardoso et al. constructed Ti/TiO_2NT-ZIF-8 MOF composite by precipitating ZIF-8 on TiO_2 nanotubes via layer-by-layer method [193]. They applied this MOF composite as a photoelectrocatalyst for CO_2 reduction reaction in aqueous solution. The MOF exhibited an efficient photoelectrocatalytic performance in converting CO_2 into methanol and ethanol (production rates of up to 10 mmolL^{-1} for C_2H_5OH and 0.7 mmolL^{-1} for CH_3OH in 0.1 molL^{-1} at 0.1 V, exposed to visible light irradiation). They ascribed this excellent efficiency to the presence of ZIF-8 which acts not only as CO_2 adsorbent but also as a co-catalyst. Table 5 shows the parameters related to three photoelectrochemical reactions by MOF composites as photoelectrocatalysts. The reduction products are ethanol or methanol.

2.4. Hydrogenation of CO_2 by MOF composites

CO_2 hydrogenation is a chemical reaction typically catalyzed by metals with hydrogenation activity like ruthenium, platinum, nickel and palladium, among others. One of the industrial catalysts used in the production of methanol from CO_2 hydrogenetion is Cu/ZnO/Al_2O_3, which has some limitations such as cogeneration of CO gas and deactivation by coke deposition. Thus, some efforts have been made to utilize MOF composites to find a more efficient alternative for this commercial catalyst. The results were compared with Cu/ZnO/Al_2O_3 as the benchmark catalyst. In one pioneering study, Yaghi and coworkers reported how the support influences the catalytic activity of Cu when incorporated within different types of MOFs, such as UiO-66, MIL-101(Cr), ZIF-8, MOF-26, to produce methanol by CO_2 hydrogenation [194]. They found that UiO-66 is the best solid for the promotion of copper catalytic properties in CO_2 hydrogenation reaction since it catalyzes the hydrogenation of CO_2 with a molar ratio of 1/3 for CO_2/H_2 at a pressure of 10 bar and a temperature of 175 °C in order to produce methanol with a selectivity of 100 %. Interestingly, the observed TOF (10 h^{-1}) is about 8 times higher than with Cu/ZnO/Al_2O_3 as benchmark catalyst. Calculation shows that in Cu@UiO-66, the 3d binding energy of Zn moved toward lower oxidation state compared to UiO-66, indicating that upon getting in contact with Cu NPs, the Zr(IV) 3d energy decreased because

Table 4
Various MOF composites with host-guest interaction as photocatalyst for CO_2 reduction.

MOF Composite	Light source Illumination range	Main carbon products [a)]	Selectivity (%)	Ref.
Ru@Cu-HHTP	>400 nm	CO (130000)	92.9	[178]
ReRu-66	100 W LED lamp 450 nm	CO (83800)[b)]	100	[173]
$Ni_3(HITP)_2$ MOF	420 nm	CO (34500)	n/a	[170]
CoOx/MIL-101	>420 nm	CO (28700)	70.3	[185]
ZIF-67@PPy	420 nm	CO (14900)	63.1	[177]
(PW12,Cp*Rh)@UiO-67	>415 nm	HCOOH (58300)[b)]	n/a	[179]
Ir1/A-aUiO	>400 nm	HCOOH (510)	99	[186]
Rh-Ru@MIL-101-NH_2	>415 nm	HCOOH (26.4)	100	[172]
Ni@Ru-UiO-67	450 nm	CO (581)[c)]	n/a	[181]
Fe-TCPP@NU-1000	1390 nm	CO (22)[c)]	n/a	[171]
Zr-DMBD − Co	visible light	CO (97941)[c)]	98	[174]
Co-ZIF-9/Ru	>420 nm	CO (41.8)		[175]
Cp*Rh@UiO-67	300 W Xe arc lamp, 415 nm	HCOOH (n/a)	n/a	[37]
UiO-67-Mn(bpy)$(CO)_3$Br	470 nm	$HCOO^-$ (50)[c)]	96	[184]
Ce-MOF/Bi_2MoO_6	350–600 nm	CH_4 (113.84) CH_3OH (4.59) HCOOH (73.48)	n/a	[188]
2Cu/ZIF-8 N_2	500 W xenon lamp 530–580 nm	CH_3OH (35.82 μmol g^{-1} L^{-1} after 6 h)	n/a	[189]

a) μmol g^{-1}h^{-1}; b) μmol^{-1}mmol^{-1}h^{-1}; c) TON.

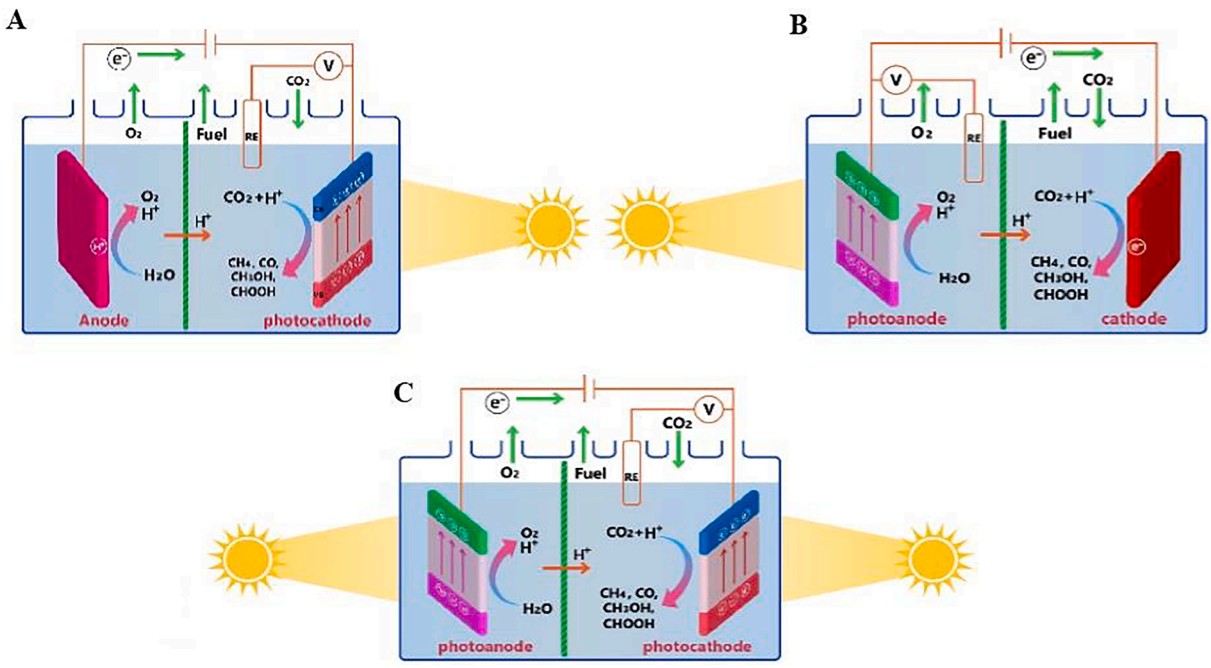

Fig. 26. Three candidates for bipartite photoelectrochemical units to be used in CO_2 reduction divided by proton-exchange membranes. (A) Semiconductor acting as photocathode. (B) Semiconductor acting as photoanode. (C) Semiconductors act both as photocathode and photoanode [3]. With permission from the Royal Society of Chemistry, copyright 2016.

Table 5
Various MOF composite photoelectrocatalysts for CO_2 reduction.

MOF composite	Electrolyte	Light source, wavelength	Main carbon product	Potential	Ref.
GO/Cu_xO/Cu-BTC	0.1 M $KHCO_3$ + 0.1 M Na_2SO_4 (4:1)	150 W Xe lamp	C_2H_5OH (162)[a)]	−0.5 V vs. Ag/Ag Cl	[191]
CuS/CuPor NSs	0.5 M H_2SO_4/0.5 M $NaHCO_3$	300 W Xe lamp, 320–410 nm	C_2H_5OH (5174)[b)]	−2 V vs. RHE	[192]
Ti/TiO_2NT-ZIF-8	0.1 M Na_2SO_4	125 W Hg lamp, UV–vis	C_2H_5OH (10)[c)], CH_3OH (0.7) [c)]	0.1 V vs. Ag/Ag Cl	[193]

a) $uMcm^{-1}$, b) $nmolh^{-1}cm^{-2}$, c) mmol L^{-1}.

of metal-support interaction.

Zeng and coworkers integrated photothermal effect and heat insulation by constructing AuPt@ZIF MOF composite to reduce the reaction temperature of CO_2 hydrogenation [195]. In the resulting MOF composite, ZIF prevents heat spreading over the solution, Au NPs transform light energy to local heat, and Pt NPs act as a role of catalyst in this reaction. They showed that the catalytic activity of Au-Pt@ZIF under light irradiation at 100 °C is comparable to that obtained in the dark at 150 °C. This MOF composite shows a TOF of 1522 h^{-1} (about 13 times as much as the TOF obtained in the dark) for producing CH_3OH under light irradiation at 150 °C.

Alloy metal NPs together with semiconductors can provide active and efficient catalytic sites for CO_2 hydrogenation. Mori et al.[196] used Pd@Ag alloy NPs for this purpose and observed that the catalytic activity was ten times higher than that of monometallic Pd/TiO_2 composite. They constructed PdAg/TiO_2@ZIF-8 MOF composite and investigated its catalytic activity for producing formic acid from CO_2 hydrogenation under reaction conditions of 2 MPa at 100 °C. The optimized MOF composite (thickness of ZIF-8 layer: 1.6 nm) exhibits a double activity compared to base materials, which is attributed to suppressing the agglomeration of NPs during the catalytic reaction. Further, the same group [197] constructed ZIF-8@Pd_nAg_m@ZIF-8 system [Pd_nAg_m NPs, n and m represent the theoretical mole ratio of Pd and Ag, respectively] and utilized it as a catalyst in CO_2 hydrogenation. Among them, ZIF-8@Pd_1Ag_2@ZIF-8 yielded the maximum catalytic performance in producing formic acid, while any greater or less Pd:Ag ratios decreased the catalytic activity. This higher catalytic efficiency is attributable to the synergistic effect generated by synthesizing PdAg alloy and ZIF-8 support. The electron-rich Pd sites provided by charge transfer from Ag to Pd and the basic N groups within the nanopores of the ZIF-8 significantly contribute to the improved production of formic acid.

Jiang et al.[198] synthesized UiO-68-supported NHC-Cu(I)-H in which N-heterocyclic carbene (NHC) is applied to anchor coinage metal hydrides M(I)-H (M: Cu, Ag and Au) onto the organic linker of UiO-68. The resulting MOF composite, when used in CO_2 hydrogenation, presents well-defined active sites suited for the production of methanol with significant efficiency. One of the common catalysts in CO_2 hydrogenation is Cu/ZnO_x, the catalytic properties of this catalyst are diminished due to the condensation of copper NPs and separation from ZnO_x. When Cu/ZnO_x is encapsulated within special MOFs, the MOF cavities prevent Cu NPs agglomeration and consequently the catalytic features of Cu/ZnO_x are enhanced. Wang and coworkers used (UiO-bpy) MOFs as novel support for NPs of Cu/ZnO_x catalyst [199]. They constructed a MOF composite called Cu/ZnO_x@UiO-bpy (bpy: 2,2′-bipyridine) through anchoring the Cu/ZnO_x NPs on the UiO-bpy MOF. The strong interaction created between Cu/ZnO_x and bpy prevents the agglomeration of copper NPs and phase separation between Cu and ZnO_x. They showed that the resulting MOF composite catalyzes CO_2 hydrogenation and produces CH_3OH with a yield of up to 2.59 $g_{MeOH}kg_{Cu}{}^{-1}h^{-1}$ and 100% selectivity at 250 °C and the pressure of 40 bar with a H_2/CO_2 ratio of 3.

Loc et al. [200] used stable UiO-66 MOF as a support for Cu, ZnO NPs to catalyze the reduction reaction of CO_2. They constructed Cu/ZnO@UiO-66 MOF composite and utilized it as catalyst in CO_2 hydrogenation reaction. This catalyst shows good efficiency in producing methanol (153.93 $\mu molg^{-1}h^{-1}$). Such high efficiency is attributed to

spherical structure of UiO-66 MOF crystal providing large surface area. Another product of CO_2 hydrogenation is CH_4. Such a reaction which yields CH_4 is also called the Sabatier reaction, appearing to be an important catalytic procedure for removing the CO_2 concentration and producing the clean CH_4 fuel.

In 2015, Lu et al. constructed a series of highly active Ni@MOF-5 catalysts for CO_2 methanation under the low temperature through impregnation methods [201]. This significant catalytic activity is ascribed to highly uniform dispersion of Ni over MOFs. This catalyst also revealed almost no deactivation during long term stability tests up to 100 h. Later in 2017, Lu and coworkers constructed a group of Ni@MIL-101 MOF composites by enclosing Ni NPs in MIL-101 via a double solvent method [202]. The resulting MOF composite with an optimal Ni loading (20 wt%) showed remarkable efficiency and good selectivity for producing CH_4 (TOF: $1.63.10^{-3}$ s^{-1} at 300 °C). This excellent efficiency is ascribed to excellent dispersion of Ni NPs and small activation energy (Ea = 68.9 kg/mol). In another work, nickel-based catalysts are suitable options for preparing CO_2 reduction catalysts due to their abundance and low cost, high activity, and selectivity for CH_4. Cheang and co-workers constructed a Ni@UiO-66 MOF composite through the adsorption of Ni NPs into the cavity of UiO-66 [203]. The resulting MOF composite with an optimal Ni loading (20 wt%) shows high selectivity (100 %) and excellent activity (57.6%) in CO_2 methanation reaction under atmospheric conditions at 250 °C when H_2/Ar ratio is 5%, which is attributed to good dispersion of Ni NPs and low activation energy (Ea: 68.9 KJ/mol).

Chen et al.[204] have prepared Ni/UiO-66 and its activity was tested in CO_2 hydrogenation reaction under nonthermal plasma (NTP) conditions. This catalyst shows a significant efficiency in conversion of CO_2 into methane in comparison with other catalysts like Ni/ZrO_2 and Ni/α-Al_2O_3, yielding a CO_2 conversion and a CH_4 selectivity of 85% and 99%, respectively, as well as a TOF (1.8 ± 0.02 s^{-1}) which is twice as much as that of Ni/ZrO_2 and Ni/α-Al_2O_3. This improvement both in efficiency and selectivity is attributed to lower energy barrier required to activate CO_2 hydrogenation of Ni/UiO-66 in comparison with Ni/α-Al_2O_3 and Ni/ZrO_2, because the excited species (such as CO_2 and H_2) and radicals generated under NTP conditions can easily interact with catalyst surface and the adsorbed species, giving rise to lowered activation energy of CO_2 hydrogenation reaction.

Ni/Al_2O_3 catalyst has been widely used due to its availability and low cost. For example, in 2020, Mihet et al.[205] constructed Ni/MIL-101-Al_2O_3 by immobilizing MIL-101 on a catalytic support (Al_2O_3), with Ni NPs deposited by an adopted double solvent approach. Then, the catalytic activities of Ni/MIL-101-Al_2O_3, Ni/MIL-101, and Ni/Al_2O_3 were compared toward methane production. The highest catalytic activity was achieved by Ni/MIL-101-Al_2O_3 in CO_2 reduction at 350 °C with a CO_2 conversion rate of 85.8% and a CH_4 selectivity to 93.2%, while the lowest catalytic activity was with Ni/Al_2O_3. This enhanced activity of the MOF composite can be attributable to the large surface area of MIL-101 (above 3000 m^2/g), its special mesoporous structure, as well as excellent thermal and mechanical stability of alumina.

Lazar et al.[206] investigated the catalytic activity of Ni NPs introduced in microporous UiO-66 and mesoporous MIL-101 in the CO_2 methanation process. They constructed Ni@UiO-66 and Ni@MIL-101 MOF composites and investigated their catalytic properties in CO_2 methanation reaction by changing some parameters such as temperature, reactant ratio, GHSV (gas hourly space velocity values), etc. The best catalytic performance was obtained for Ni@MIL-101 sample in CO_2 hydrogenation reaction with CO_2 conversion of 56.4 % and CH_4 selectivity to 91.6% at 320 °C at CO_2:H_2 ratio of 1.8. This remarkable performance is attributed to a significant contribution of the Ni-MOF interaction to the CO_2 adsorption capacity.

Recently, ruthenium compounds have been developed to serve as active catalyst for the hydrogenation of CO_2 to carboxylic acid and methane. In 2022, Wang et al.[207] constructed a MOF composite called $RuCl_3$@ZIF-8-Mtz [Mtz: 3-methyl-1,2,4-triazole] by anchoring $RuCl_3$ on

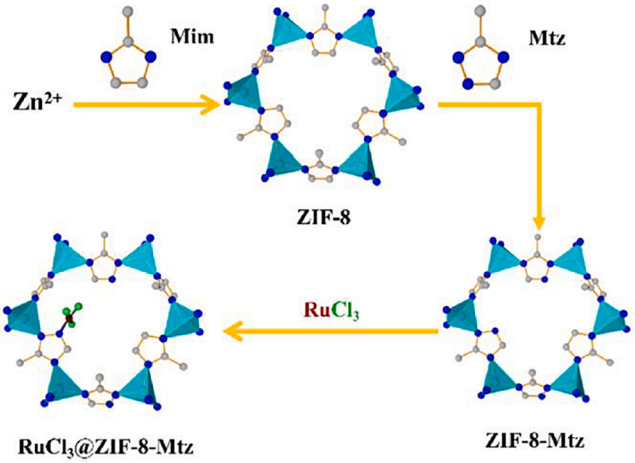

Fig. 27. Synthesis pathway of $RuCl_3$@ZIF-8-Mtz [207]. With permission from the Elsevier, copyright 2021.

modified ZIF-8. ZIF-8 was chosen as the primary MOF and 3-methyl-1,2,4-triazole (Mtz) with an additional N site (mime) as a new ligand partially replaced the parent ligand through the post-synthetic method (Fig. 27). These results indicate that as N-sites in Mtz donate additional electron-density to Ru, they make CO_2 more active. Therefore, $RuCl_3$@ZIF-8-Mtz (0.29) which contains most Mtz ligands show a better catalytic efficiency compared to $RuCl_3$@ZIF-8-Mtz(0.15) and $RuCl_3$@-ZIF-8 in CO_2 hydrogenation toward formic acid.

Recently, Mehlana et al.[208] constructed JMS-1 MOF and Ru(II)@JMS-1a MOF composite both of which are able to convert CO_2 into formate in the presence of hydrogen, while Ru(II)@JMS-1a shows a higher efficiency than JMS-1 MOF. Under optimized conditions (total pressure of 50 bar, $CO_2/H_2 = 1{:}4$ at a temperature of 110 °C) it produces formate with a yield of 98%. Such an outstanding conversion is acquired by incorporating active catalytic centers in MOF.

In another example, Wang et al.[209] prepared $RuCl_3$@MIL-101(Cr)-Sal (Sal: salicylaldehyde) and $RuCl_3$@MIL-101(Cr)-DPPB (DPPB:2-diphenylphosphinobenzaldehyde) MOF composites by anchoring of $RuCl_3$ onto some modified MOFs including MIL-101(Cr)-Sal and MIL-101(Cr)-DPPB. Then they employed these MOF composites as catalysts in CO_2 hydrogenation reaction. The results indicate that $RuCl_3$@MIL-

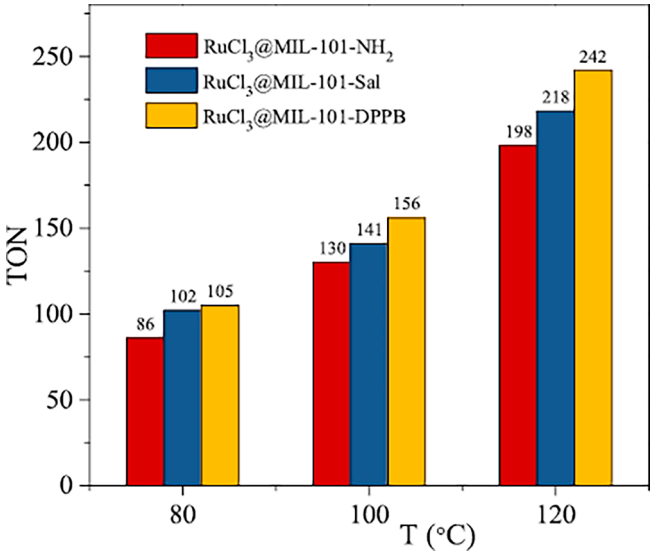

Fig. 28. Catalytic performance of the different catalysts with the different temperatures [209]. With permission from Elsevier, copyright 2022.

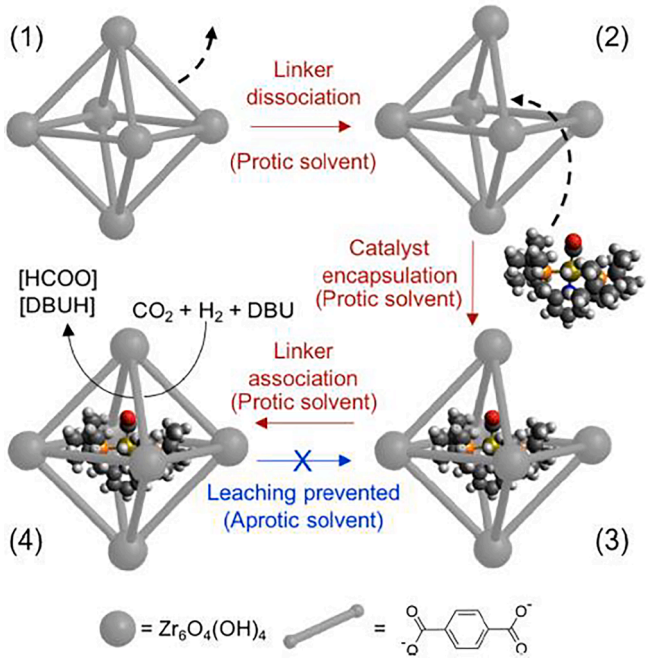

Fig. 29. Catalysis in MOFs using aperture-opening encapsulation [210]. With permission from the Royal Society of Chemistry, copyright 2020.

101(Cr)-DPPB leads to a higher catalytic efficiency toward formic acid compared to when $RuCl_3$@MIL-101(Cr) and $RuCl_3$@MIL-101(Cr)-Sal. The observed TON for such case equals to 831 under 6 MPa (CO_2/H_2 = 1:1) at 120 °C with DMSO and H_2O as the mixed solvents and Et_3N as the base additive in the presence of PPh_3. This enhanced efficiency is attributed to the stronger coordination electron donor interaction between Ru(III) ions and chelating groups in the $RuCl_3$@MIL-101(Cr)-DPPB. The performance comparison of three catalysts is observed in Fig. 28.

Sometimes, to perform highly efficient catalytic reactions, it is necessary to incorporate large molecules into the structure of the MOFs to produce catalyst MOF-composites. In 2018, Byers and Tsung designed a new technique for encapsulating large molecules in the pores of MOFs, the dissociative of linkers and their exchange is used (Fig. 29). This process depends on the nature of the solvent and was used for the synthesis of host–guest composites for chemical catalysis. They constructed Ru@UiO-66 MOF composite via aperture-opening process by encapsulation of the transition metal Ru complex [(t-Bu-PNP)Ru(CO)-HCl] (t-Bu-PNP: 2,6-bis((di-*tert*-butylphosphino)methyl)pyridine) in a MOF [210]. This MOF composite shows a good catalytic activity in CO_2 hydrogenation reaction with a TOF value of 6.105 h^{-1} at 27 °C and 15 bar with a H_2/CO_2 ratio of 4 for formate production. Also, this catalyst shows higher recyclability, more decelerated bimolecular deactivation actions, and better anti-poisoning capacity compared to its homogeneous alternative.

Homogeneous Ru catalysts have good application potential in CO_2 hydrogenation. However, there are problems such as catalyst and product separation that limit their applications. Therefore, the development of Ru-based heterogeneous catalysts is of great importance. Wang et al.[211] immobilized different Ru complexes $RuCl_3$, $[RuCp^*Cl_2]_2$ (Cp^* : pentamethylcyclopentadienyl) and $[Ru(C_6Me_6)Cl_2]_2$ (C_6Me_6 : hexamethylbenzene) on an azolium-based MOF to construct the so-called Ru_x-NHC-MOF (x = 1, 2, 3). Among these constructed systems, Ru_3-NHC-MOF composite shows the highest efficiency with a TON of 3803 at 120 °C under a total pressure of 8 MPa (H_2:CO_2 = 1) for 2 h. This high efficiency is attributed to the strong electron-donating ability of C_6Me_6 ligand of $[Ru(C_6Me_6)Cl_2]_2$ complex.

Plasma is an ionized gas that consists of equivalent ionizing positive and negative ions and electrons. High energy electrons can provide a large amount of energy to activate the CO_2 redox reaction at the low temperature. In 2019, Xu et al.[212] applied Ru/Zr-MOF catalyst for CO_2 hydrogenation toward CH_4 in an optimal ratio of H_2:CO_2 (4:1), with an assist from dielectric barrier discharge plasma. The outcomes indicate that the synergistic effect between plasma and Ru/Zr-MOF composite facilitates CO_2 conversion toward CH_4 about 1.9 times as much as when pure plasma and plasma with Zr-MOF are utilized (a yield of 39.1 % and a selectivity of 94.6%).

Another example of Ru-composite and conversion of CO_2 to methane was recently reported [213]. Ru/SION-105 MOF (SION-105 : Eu-MOF) was prepared by immobilizing Ru NPs on the Eu-MOF, providing an indirect pathway to convert CO_2 into methane. Through this new method, the catalyst efficiently transforms amino-alcohol to oxazolidinones (upon reaction with CO_2) and then to methane by hydrogen. The details of the reaction mechanism are illustrated in Fig. 30.

Platinum, palladium and nickel dioxide are three common catalysts used for CO_2 hydrogenation which reveal enhanced catalytic activity when supported on MOFs, and it is because of the special features of MOFs. Liu et al. [214] constructed Pd@PtNCs@UiO-66 MOF composite by encapsulating Pd@PtNPs into UiO-66, and then etched the compound further to form Pd@PtNCs. The resulting MOF composite shows high CO_2 conversion to CO with a significant selectivity. Such improvement is attributed to UiO-66 which prevents Pd@PtNCs from agglomeration and sintering.

Jiang and coworkers [215] utilized light irradiation to improve the conditions of hydrogenation reaction. They prepared Pd_3Cu@UiO-66 MOF composite by encapsulating Pd_3Cu NPs into UiO-66 and then applied the product as catalyst in hydrogenation of CO_2 to methanol under light irradiation. According to these results, the maximum yield of methanol was 340 $\mu molg^{-1}h^{-1}$ at 1.25 MPa, 200 °C. The acquired yield is 5.6 times more than when the reaction is executed in the dark. This improvement is attributed to light irradiation which helps to form HCOO* intermediate and therefore accelerates the rate determining step.

In another work, Pt@UiO-67 MOF composite [216] was constructed by encapsulating Pt NPs in Zr-based MOF and utilized it as catalyst in CO_2 hydrogenation reaction. This MOF composite improves the conditions of CO_2 hydrogenation reaction thanks to Pt NPs embedded into MOF structure. Under a total pressure of 8 bar and at 170 °C, approximately 1 % conversion of CO_2 led to the formation of methanol (approximately 20 %) and methane (approximately 80 %).

The reduction product of formic acid is a valuable material because it provides a starting material to access a wide range of useful organic derivatives such as carboxylic acids and amides. Recently, Makhubela et al.[217] by using a composite based on Pd, Ni, Pt NPs provided the redox reaction conditions for the production of formate. They constructed MOF/M composite, [M: Pd, Ni, Pt] and MOF : $[Cd(bdc)(DMF)]_n$ by impregnating cadmium-based MOF with Pd, Ni, and Pt NPs. Then, they utilized the original MOF and the resulting MOF composites as catalysts in CO_2 hydrogenation. The MOF composite shows higher efficiency than the original MOF in CO_2 hydrogenation, and unlike the original MOF, they produced formate, selectively. Among the three MOF composites, MOF/Pt produced the highest amount of formate (TON: 1500) at 170 °C within 2 h. This enhancement in activity (a formate yield of 98%) is attributed to the impregnation of metal NPs into the MOF which boosts the catalytic activity of active sites.

Zhang et al.[218] prepared a group of Pd@UiO-66 catalysts with various loadings of Pd NPs via a sol–gel method, and their activity is tested in CO_2 methanation reaction. The resulting MOF composite with optimal amounts (Pd loading of 6 wt%) shows a high efficiency, yielding a CO_2 reduction rate of 50 % and a CH_4 selectivity to 97.3 % at 340 °C, 4 MPa. This remarkable efficiency is ascribed to the synergistic effect between Pd and UiO-66 in which the Zr-O group of UiO-66 MOF gives rise to an enhanced CO_2 adsorption, and palladium NPs provide the activated CO_2 with hydrogen species.

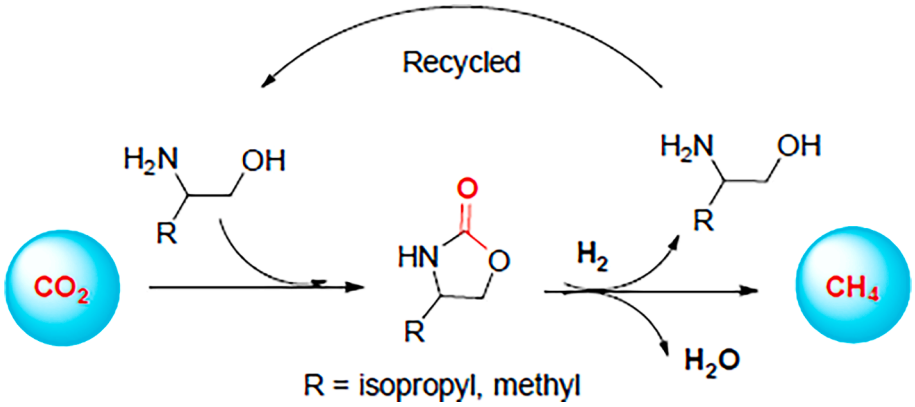

Fig. 30. Representation of CO_2 methanation by using amino-alcohols.

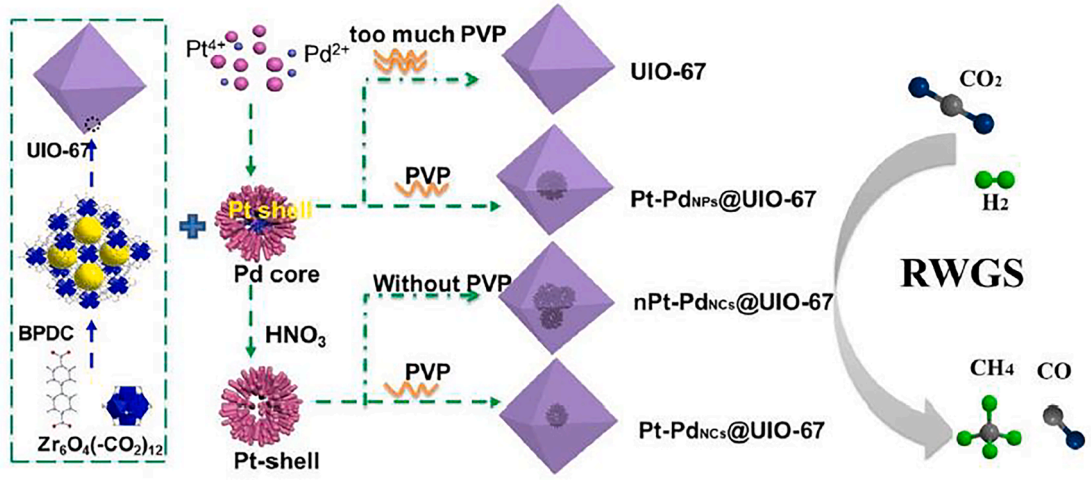

Fig. 31. Synthesis pathway for preparing M@UiO-67 (M = Pt–PdNPs, Pt–PdNCs) [220]. With permission from Elsevier, copyright 2019.

Another example of the catalytic reaction of converting CO_2 to formate by the synergistic effect of NPs incorporated to MOF was reported by Mehlana et al.[219] They provided two isostructural Pd(II)-containing MOFs (Pd@Mg:JMS-2a and Pd@Mn:JMS-2a). When utilized in CO_2 hydrogenation, both exhibited higher catalytic activity than base materials to formate (TON values of 7272 and 9808 were respectively obtained for Pd@Mg:JMS-2a and Pd@Mn:JMS-2a after 24 h). For such homogenous systems, the catalytic activity can be enhanced by anchoring them on MOFs.

Composite M@UiO-67 (M: Pt-Pd NPs, Pt-Pd NCs) were employed by Xu et al.[220] Branched Pt-Pd NPs or Pt-Pd NCs were placed as core in UiO-67. The synthesis pathway for preparation the M@UIO-67 composite is given in Fig. 31. The activity of these solids was tested in CO_2 hydrogenation. The MOF composite with Pt-Pd NCs shows an improved CO_2 hydrogenation reaction toward CO compared to Pt-Pd NPs. This improvement is attributed to the hollow structure of Pt-Pd NCs.

Stawowy et al.[221] demonstrated that MOF-supported Cu NPs can be an appropriate catalyst for converting CO_2 into alcohols in hydrogenation reaction. They investigated the effect of introduction of copper NPs to the modified UiO-66(Ce/Zr) MOF composite in CO_2 hydrogenation reaction toward methanol production. Initially, they exchanged 50% of Zr content in UiO-66 with Ce and observed that the selectivity toward the methanol product increased from 3.5% to 28.7%. Later, Cu NPs was introduced to the modified UiO-66(Ce/Zr) MOF composite and found that the selectivity toward the methanol product enhanced to 59 %. This improvement is attributed to Zr-Cu and Ce-Cu proper interactions. In a similar work, Taylor et al.[222] prepared a series of CuNPs@zirconium/hafnium MOF composites and their activity is tested in CO_2 hydrogenation reaction toward methanol. The results indicate that the performance of Cu/MOF composite in hydrogenation of CO_2 to methanol depends on the rate of charge transfer between metal NPs and MOF which can be controlled by an appropriate assortment of functional group and metal species.

Mitsuka et al.[223] constructed Cu/amorphous UiO-66 from Cu NPs and amorphous UiO-66 and also Cu-ZnO/amUiO-66 from Cu-ZnO nanocomposites and amUiO-66 by using spray-drying method. Having investigated the catalytic activity for CO_2 hydrogenation toward methanol, they showed that the catalytic activity of Cu/amUiO-66 is three times as much as that of Cu/UiO-66, while the catalytic activity of Cu-ZnO/amUiO-66 is respectively 1.5 times and 2.5 times as much as those of Cu/amUiO-66 and Cu-ZnO/γ-Al_2O_3. In all the above-mentioned cases, MOF composites exhibit better catalytic activity thanks to their unique structural properties.

Controlling the catalytic product selectivity of CO_2 reduction by irradiation intensity is an interesting report by Zeng et al.[224] They explained the use of light in order to fix metal centers of an intermediate oxidation state for selective chemical conversions of CO_2. They demonstrated that when low-intensity light is applied, Cu(I) species are generated and ethanol is acquired as a product of CO_2 reduction. However, by generation of Cu(0) species in darkness, methanol is resulted from CO_2 reduction reaction (Fig. 32).

Xu et al. utilized UiO to develop a catalytic system for CO_2 hydrogenation reaction. They [225] constructed $ZnZrO_x$/SAPO-34@UiO-n (n = 66, 66-NH_2 and 67), and their activity is tested in CO_2 hydrogenation

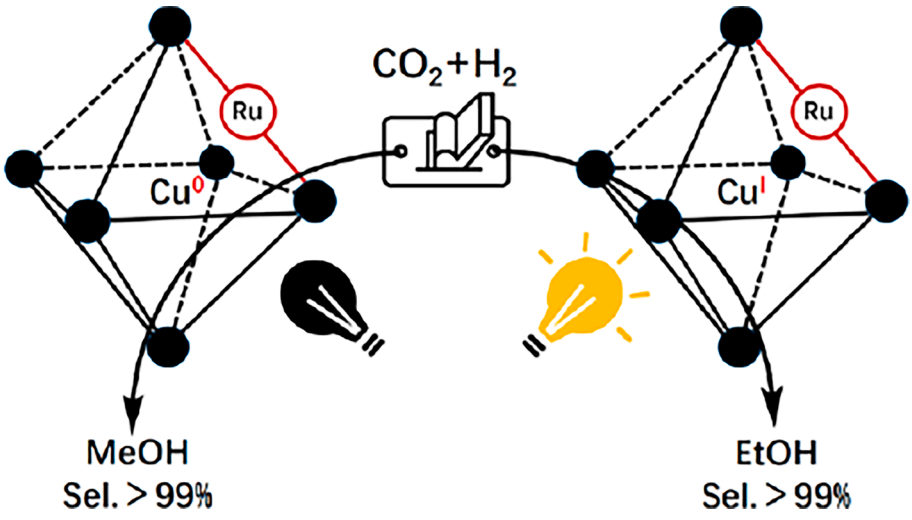

Fig. 32. Controlling catalytic selectivity of CO_2 hydrogenation using low-intensity light [224]. With permission from the Royal Society of Chemistry, copyright 2019.

toward light olefins. The MOF composite shows very selective CO_2 reduction to 80 % yield for production of C_2-C_4 olefins, whereas upon omitting the MOF component from the above system and by applying $ZnZrO_x$/SAPO-34 as catalyst, paraffin products are generated with a yield of 57%. These results indicate that utilizing UiO-n MOF shifts the product of CO_2 hydrogenation from paraffins toward olefins.

In an analogous work, Au et al.[226] immobilized molecular iridium catalyst in UiO MOF and used the resulted material as catalyst in CO_2 hydrogenation reaction through which a high TOF of 410 h^{-1} was acquired for producing formic acid under atmospheric pressure and at 85 °C. This improvement is ascribed to the large surface area provided by MOF component of new system.

Wang et al. used a ZnO catalyst for hydrogenation of CO_2. They [227] constructed ZnO/Zr-MOF and its catalytic performance is evaluated in CO_2 hydrogenation reaction. The resulting MOF composite exhibits a yield of 110 mg $_{MeOH}$ $g^{-1}_{catalyst}$ or 440 mg $_{MeOH}$ g $^{-1}_{Zn}h^{-1}$ with more than 95% selectivity for CH_3OH production which is amongst the top amounts reported for analogous catalysts. This improvement is attributed to the capability of Zr-MOF to prevent the agglomeration of Zn NPs.

Prior to the above study, Hong et al.[228] in a similar work had constructed ZnO/ZIF-8 MOF composite through epitaxial growth of a thin ZIF-8 on ZnO nanorods and used as catalyst in CO_2 hydrogenation reaction. The resulting MOF composite when prepared in optimal percentage of components produces methanol in CO_2 hydrogenation with a selectivity range of 66–78% and a yield range of 12.1–19.8 at 523–563 K at 4.5 M/Pa which is amongst the top record reported in analogous cases. They also showed that there is a volcanic relationship between CH_3OH yield and the thickness of ZIF-8.

Co NPs showed high catalytic activity and selectivity for linear hydrocarbons and with a low activity in the WGS (water–gas shift) reaction. The special feature of Co-containing catalysts is that in their reaction the H_2:CO ratio is close to the stoichiometric ratio and the methane yield increases with increasing temperature. Also, due to their high hydrogenation activity, mainly alkanes are produced. For instance, in 2018, Kustov et al.[229] constructed Co/MIL-53(Al) through embedding Co NPs in Co/MIL-53(Al) and utilized as catalyst in CO_2 hydrogenation reaction yielding hydrocarbon and carbon monoxide with high efficiency (with total CO_2 conversion of 37.5% at 340 °C). This improvement in the CO_2 reduction compared to the thermodynamic conversion is attributable to the expected shift of the equilibrium toward the formation of CO due to its further rapid conversion to hydrocarbons by the Fisher-Tropsch reaction.

In general, it is very important to find the optimal conditions for the CO_2 hydrogenation reaction, such as the molar ratio of H/CO_2, temperature and pressure. Table 6 shows the types of CO_2 hydrogenation reactions by various MOF composites as catalysts and the conditions of the reactions.

3. Conclusion and future outlook

MOF composites, thanks to their unique structural characteristics, are increasingly being developed to replace conventional catalysts. Among others, MOF composites are also considered as potential catalysts for conversion of CO_2 as an undesirable greenhouse gas. To put it concisely, the utilizations of MOF composites as catalysts in reduction of CO_2, including electroreduction, photoreduction, photoelectroreduction and hydrogenation of CO_2 were discussed. Although MOF composites are of high capability to be utilized as catalysts in converting CO_2 into valuable compounds, their catalytic features must be improved by minimizing certain weak points such as low thermal and chemical stability. Also, by fully understanding the interactions among different components of MOF composites, rational methods shall be designed to construct such compounds in a purposeful way. On the other hand, CO_2 reduction by MOF composites has been mostly carried out on a laboratory scale. However, to control the atmospheric CO_2, such a process shall be carried out on an industrial scale. It is noteworthy that the MOF composite catalysts made up of a combination of inexpensive transition metals including metal oxides and polycarboxylic aromatic compounds available in large scale are considered as economic catalysts. Hence, in the domain of industrial scale application, it is recommended to focus and carry out more research on this special kind of catalyst for photochemical and electrophotochemical reducing of CO_2.

Moreover, major compounds obtained from CO_2 reduction reaction by using MOF composites are usually either one-carbon compounds including CO, CH_4, HCOOH, and CH_3OH or two-carbon compounds including CH_3CH_2OH, CH_3COOH, and C_2H_4. Thus, being inspired by the fact that when bimetallic MOF composites are used as catalysts the reaction goes towards producing two-carbon products, it seems to be appropriate to place focus on producing valuable products with more than two carbon atoms.

In electrochemical reduction of CO_2, those MOF composites which are built using the most common elements on the Earth exhibiting an outstanding selectivity and Faradaic efficiency, assist the electrocatalytic reduction of CO_2. Assuming a scenario in which green, renewable electricity is cheap during certain valley hours, it seems appropriate to spend more time and effort concentrating on fabricating such an electrocatalyst category of MOF composites.

Furthermore, most of MOF composites utilized as photocatalyst in

Table 6
Various MOF composites as catalysts for hydrogenation of CO_2.

MOF composite	T (°C), Pressure (bar)	Main carbon products	TOF (h^{-1})	Ref.
CuC UiO-66	175, 10 ($H_2/CO_2 = 3$)	CH_3OH	10	[194]
Cu/ZnOx@UiO-bpy	250, 40 ($H_2/CO_2 = 3$)	CH_3OH	2.59 g_{MeOH} $kg_{Cu}^{-1}h^{-1}$	[199]
Au&Pt@ZIF	150, 32 ($H_2/CO_2 = 3$)	CH_3OH	1522	[195]
[Ru]@UiO-66	27, 15 ($H_2/CO_2 = 4$)	HCOOH	600,000	[197]
Ni@MOF-5	1 ($H_2/CO_2 = 4$)	CH_4	75[a]	[201]
20Ni@MIL-101	300, 1 ($H_2/CO_2 = 4$)	CH_4	5.868	[202]
Ni@UiO-66	320, 10 ($H_2/CO_2 = 3$)	CH_4	154.8	[203]
PdAg/TiO_2@ZIF-8	20 ($H_2/CO_2 = 1$)	HCOOH	15.2 [d]	[196]
ZIF-8@Pd_1Ag_2@ZIF-8	100, 20 ($H_2/CO_2 = 1$)	HCOOH	0.695 [d]	[197]
Cu,ZnO@UiO-66	(n/a), (n/a)	CH_3OH	153.93 [d]	[200]
Ni/UiO-66	250, atmospheric pressure, (H_2:$CO_2 = 4$)	CH_4	99[b]	[204]
Ni/MIL-101-Al_2O_3	350, 1 atm (CO_2:H_2 = 1:5.2)	CH_4	93.2[b]	[205]
Ni@MIL-101	320, 1 atm (CO_2:H_2 = 1:8)	CH_4	4650	[206]
$RuCl_3$@ZIF-8-Mtz	120, 40 ($H_2/CO_2 = 1$)	HCOOH	85.8[a]	[207]
Ru(II)@JMS-1a	110, 50 (CO_2/H_2 = 1:4)	$HCOO^-$	98[c]	[208]
$RuCl_3$@MIL-101(Cr)-DPPB	120, 60 (CO_2/H_2 = 1:1)	HCOOH	831[f]	[209]
Ru_3-NHC-MOF	120, 80 (H_2:$CO_2 = 1$)	HCOOH	3803[f]	[211]
Ru/Zr-MOF	DBD cold plasma, atm pressure ($H_2/CO_2 = 4$)	CH_4	39.1[c]	[212]
Ru/SION-105	205, 70	CH_4	71[c]	[213]
Pd@PtNCs@UiO-66	400, 20 (CO_2/H_2 = 1:3)	CO	19.6[c]	[214]
Pd_3Cu@UiO-66	200, 12.5	CH_3OH	340 [e]	[215]
Pt@UiO-67	170, 8 (CO_2/H_2 = 1:6)	CH_3OH,CH_4	20,80[c]	[216]
Cu/UiO-66(Ce/Zr)	200, 18 (H_2/CO_2:3/1)	CH_3OH	468 [e]	[221]
mbpyOH-[IrIII]-UiO	atmospheric-pressure	HCOOH	410	[226]
ZnO/ZrMOF	4(H_2/CO_2:3/1)	CH_3OH	>95[b]	[227]
ZnO/ZIF-8 MOF	250–290, 45	CH_3OH	66–78[b]	[228]

a) conversion (%); b) selectivity (%); c) yield (%); d) $mmolh^{-1}g^{-1}$; e)$\mu molg^{-1}h^{-1}$; f)TON.

CO_2 reduction are developed on MOF architecture of ZIF, UiO, and MIL series because of their remarkable water stability. Therefore, it is recommended to make more efforts to construct some MOF composites based on other MOFs than MIL, UiO and ZIF, with high water stability, so that they can act as photocatalyst in CO_2 reduction reaction. Also, CO_2 reduction by MOF composites using electrophotochemical method have not been adequately addressed yet. Since in this method the consumption rate of electrical energy is reduced due to the simultaneous use of solar energy, and as this fact is dramatically important in economic terms, it appears to be a very good field for more research and development.

Moreover, alcohols are the main products of photoelectrochemical CO_2 reduction. Hence it is recommended that further efforts be made to fabricate other value-added chemicals including saturated and unsaturated hydrocarbons as well as carboxylic acids by controlling certain parameters including electric current density, electrolyte solution, etc.

In hydrogenation method, since many of MOF composites are unstable in high temperatures, finding an appropriate MOF composite being able to perform CO_2 reduction in room temperature and atmospheric pressure and low concentration of CO_2 is of great importance. Consequently, MOF composites show a bright future as heterogenous catalysts for reduction and conversion of CO_2 into valuable materials. The next challenges will be the removing of some deficiencies (such as low thermal and chemical stability) of MOF composites, their purposeful synthesis, and their application on an industrial scale.

The selectivity of the CO_2 reduction reaction can be increased by several methods. One possibility is the use of electrically active supports that by adjusting the voltage of the redox reaction drive the product selectivity to a specific compound having the matching redox potential. Carbon matrices can be used as supports in this method, which can also help selectivity through tuning the pore size and specific surface area. Another way to increase selectivity is to introduce special functional groups in the composite framework, which may increase the selectivity percentage even up to five times. In addition, the use of metal NPs in composites can improve the selectivity of carbon CO_2 reaction towards valuable hydrocarbons.

Declaration of Competing Interest

The authors declare that they have no known competing financial interests or personal relationships that could have appeared to influence the work reported in this paper.

Data availability

Data will be made available on request.

Acknowledgements

The authors gratefully acknowledge from Tarbiat Modares University and the support received from the Niroo Research Institute (NRI) under the contract number 99/50420/152. This work was supported by the National Natural Science Foundation of China (Grant No. 92161106), the Natural Science Foundation of Ningxia (Grant No. 2022AAC05017), and the Foundation of State Key Laboratory of Physical Chemistry of Solid Surfaces (Grant No. 202013). Financial support by the Spanish Ministry of Science and Innovation (PDI-2021-0126071-OB-CO21) and Generalitat Valenciana (Prometeo 2021-038) is gratefully acknowledged. This study forms part of the Advanced Materials programme and was supported by MCIN with funding from European Union NextGenerationEU (PRTR-C17.I1) and by Generalitat Valenciana (Graphica MFA/2022/023. The Institute is a Center of Excellence Severo Ochoa (CEX-2021-001230-S). A.D. is beneficiary of a grant María Zambrano in Universitat Politècnica de València within the framework of the grants for the retraining in the Spanish university system (Spanish Ministry of Universities, financed by the European Union, NextGeneration EU).

References

[1] R. Wang, F. Kapteijn, J. Gascon, Chem. Asian J. 14 (2019) 3452–3461.
[2] D. Li, M. Kassymova, X. Cai, S.-Q. Zang, H.-L. Jiang, Coord. Chem. Rev. 412 (2020), 213262.
[3] S. Xie, Q. Zhang, G. Liu, Y. Wang, Chem. Commun. 52 (2016) 35–59.
[4] A. Álvarez, A. Bansode, A. Urakawa, A.V. Bavykina, T.A. Wezendonk, M. Makkee, J. Gascon, F. Kapteijn, Chem. Rev. 117 (2017) 9804–9838.

[5] M.W. Hussain, A. Giri, A. Patra, Sustain. Energy Fuels 3 (2019) 2567–2571.
[6] J. Liu, L. Chen, H. Cui, J. Zhang, L. Zhang, C.-Y. Su, Chem. Soc. Rev. 43 (2014) 6011–6061.
[7] S. Kempahanumakkagari, K. Vellingiri, A. Deep, E.E. Kwon, N. Bolan, K.-H. Kim, Coord. Chem. Rev. 357 (2018) 105–129.
[8] L. Zhang, J. Liu, C.-Y. Su, Porphyrin Metal-Organic Frameworks in Heterogeneous Supramolecular Catalysis, in: Supramolecular Catalysts: Design, Fabrication and Applications, World Scientific, 2020, pp. 225–265.
[9] A. Bavykina, N. Kolobov, I.S. Khan, J.A. Bau, A. Ramirez, J. Gascon, Chem. Rev. 120 (2020) 8468–8535.
[10] M.Y. Masoomi, K.C. Stylianou, A. Morsali, P. Retailleau, D. Maspoch, Cryst. Growth Des. 14 (2014) 2092–2096.
[11] A.R. Abbasi, A. Moshtkob, N. Shahabadi, M.Y. Masoomi, A. Morsali, Ultrason. Sonochem. 59 (2019), 104729.
[12] S.A.A. Razavi, M.Y. Masoomi, A. Morsali, Chem. Eur. J. 23 (2017) 12559–12564.
[13] F. Bigdeli, C.T. Lollar, A. Morsali, H.C. Zhou, Angew. Chem. Int. Ed. 59 (2020) 4652–4669.
[14] N. Abdollahi, S.A.A. Razavi, A. Morsali, M.-L. Hu, J. Hazard. Mater. 387 (2020), 121667.
[15] R. Abazari, A. Morsali, D.P. Dubal, Inorg. Chem. Front. 7 (2020) 2287–2304.
[16] X. Li, Q.-L. Zhu, EnergyChem 2 (2020), 100033.
[17] H. Zhang, J. Li, Q. Tan, L. Lu, Z. Wang, G. Wu, Chem. Eur. J. 24 (2018) 18137–18157.
[18] A. Dhakshinamoorthy, A.M. Asiri, H. Garcia, Trends Chem. 2 (2020) 454–466.
[19] C.-W. Kung, C.O. Audu, A.W. Peters, H. Noh, O.K. Farha, J.T. Hupp, ACS Energy Lett. 2 (2017) 2394–2401.
[20] B.C. e Silva, K. Irikura, J.B.S. Flor, R.M.M. Dos Santos, A. Lachgar, R.C.G. Frem, M.V.B. Zanoni, J. CO2 Util. 42 (2020), 101299.
[21] Y. Zhou, L. Zheng, D. Yang, H. Yang, Q. Lu, Q. Zhang, L. Gu, X. Wang, Small Methods 5 (2021) 2000991.
[22] H. Liu, H. Wang, Q. Song, K. Küster, U. Starke, P.A. van Aken, E. Klemm, Angew. Chem. Int. Ed. 61 (2022) e202117058.
[23] M. Tahir, N.S. Amin, Energy Convers. Manag. 76 (2013) 194–214.
[24] K. Kočí, L. Obalová, Z. Lacný, Chem. Pap. 62 (2008) 1–9.
[25] H.-Q. Xu, J. Hu, D. Wang, Z. Li, Q. Zhang, Y. Luo, S.-H. Yu, H.-L. Jiang, J. Am. Chem. Soc. 137 (2015) 13440–13443.
[26] D. Wang, R. Huang, W. Liu, D. Sun, Z. Li, ACA Catal. 4 (2014) 4254–4260.
[27] Y.T. Guntern, J.R. Pankhurst, J. Vávra, M. Mensi, V. Mantella, P. Schouwink, R. Buonsanti, Angew. Chem. Int. Ed. 58 (2019) 12632–12639.
[28] Z. Xin, Y.-R. Wang, Y. Chen, W.-L. Li, L.-Z. Dong, Y.-Q. Lan, Nano Energy 67 (2020), 104233.
[29] Z. Yuan, M.R. Eden, R. Gani, Ind. Eng. Chem. Res. 55 (2016) 3383–3419.
[30] A. Schoedel, Z. Ji, O.M. Yaghi, Nature Energy 1 (2016) 1–13.
[31] D. Sun, Y. Fu, W. Liu, L. Ye, D. Wang, L. Yang, X. Fu, Z. Li, Chem. Eur. J. 19 (2013) 14279–14285.
[32] L. Shen, R. Liang, L. Wu, Chin. J. Catal. 36 (2015) 2071–2088.
[33] K.G. Laurier, F. Vermoortele, R. Ameloot, D.E. De Vos, J. Hofkens, M.B. Roeffaers, J. Am. Chem. Soc. 135 (2013) 14488–14491.
[34] C. Gomes Silva, I. Luz, F.X. Llabres i Xamena, A. Corma, H. García, Chem. Eur. J. 16 (2010) 11133–11138.
[35] L. Shen, W. Wu, R. Liang, R. Lin, L. Wu, Nanoscale 5 (2013) 9374–9382.
[36] L.-W. Xu, S.-L. Qian, B.-X. Dong, L.-G. Feng, Z.-W. Li, J. Mater. Sci. 57 (2022) 526–537.
[37] M.B. Chambers, X. Wang, N. Elgrishi, C.H. Hendon, A. Walsh, J. Bonnefoy, J. Canivet, E.A. Quadrelli, D. Farrusseng, C. Mellot-Draznieks, ChemSusChem 8 (2015) 603–608.
[38] I. Hod, M.D. Sampson, P. Deria, C.P. Kubiak, O.K. Farha, J.T. Hupp, ACS Catal. 5 (2015) 6302–6309.
[39] R.S. Pillai, H. Jobic, M.M. Koza, F. Nouar, C. Serre, G. Maurin, N.A. Ramsahye, Chemphyschem 18 (2017) 2739–2746.
[40] M. Prakash, H. Jobic, N.A. Ramsahye, F. Nouar, D. Damasceno Borges, C. Serre, G. Maurin, J. Phys. Chem. C 119 (2015) 23978–23989.
[41] B.L. Huang, A.J.H. McGaughey, M. Kaviany, Int. J. Heat Mass Transf. 50 (2007) 393–404.
[42] A.I. Skoulidas, J. Am. Chem. Soc. 126 (2004) 1356–1357.
[43] M. Alvaro, E. Carbonell, B. Ferrer, F.X. Llabrés i Xamena, H. Garcia, Chem., Eur. J. 13 (2007) 5106–5112.
[44] X. Zhao, H. Xu, X. Wang, Z. Zheng, Z. Xu, J. Ge, ACS Appl. Mater. Interfaces 10 (2018) 15096–15103.
[45] X. Jiang, H. Wu, S. Chang, R. Si, S. Miao, W. Huang, Y. Li, G. Wang, X. Bao, J. Mater. Chem. A 5 (2017) 19371–19377.
[46] X. Xie, X. Zhang, M. Xie, L. Xiong, H. Sun, Y. Lu, Q. Mu, M.H. Rummeli, J. Xu, S. Li, J. Zhong, Z. Deng, B. Ma, T. Cheng, W.A. Goddard, Y. Peng, Nature Commun. 13 (2022) 63.
[47] P. De Luna, W. Liang, A. Mallick, O. Shekhah, F.P. García de Arquer, A.H. Proppe, P. Todorović, S.O. Kelley, E.H. Sargent, M. Eddaoudi, ACS Appl. Mater. Interfaces 10 (2018) 31225–31232.
[48] J. Albo, M. Perfecto-Irigaray, G. Beobide, A. Irabien, J. CO2 Util. 33 (2019) 157–165.
[49] S.-M. Hwang, S.Y. Choi, M.H. Youn, W. Lee, K.T. Park, K. Gothandapani, A. N. Grace, S.K. Jeong, ACS Omega 5 (2020) 23919–23930.
[50] L. Ye, J. Liu, Y. Gao, C. Gong, M. Addicoat, T. Heine, C. Wöll, L. Sun, J. Mater. Chem. A 4 (2016) 15320–15326.
[51] J.-X. Wu, S.-Z. Hou, X.-D. Zhang, M. Xu, H.-F. Yang, P.-S. Cao, Z.-Y. Gu, Chem. Sci. 10 (2019) 2199–2205.
[52] N. Kornienko, Y. Zhao, C.S. Kley, C. Zhu, D. Kim, S. Lin, C.J. Chang, O.M. Yaghi, P. Yang, J. Am. Chem. Soc. 137 (2015) 14129–14135.
[53] M.-J. Liu, S.-M. Cao, B.-Q. Feng, B.-X. Dong, Y.-X. Ding, Q.-H. Zheng, Y.-L. Teng, Z.-W. Li, W.-L. Liu, L.-G. Feng, Dalton Trans. 49 (2020) 14995–15001.
[54] Y.-R. Wang, Q. Huang, C.-T. He, Y. Chen, J. Liu, F.-C. Shen, Y.-Q. Lan, Nature Commun. 9 (2018) 4466.
[55] Y. Guo, W. Shi, H. Yang, Q. He, Z. Zeng, J.-Y. Ye, X. He, R. Huang, C. Wang, W. Lin, J. Am. Chem. Soc. 141 (2019) 17875–17883.
[56] X. Tan, C. Yu, C. Zhao, H. Huang, X. Yao, X. Han, W. Guo, S. Cui, H. Huang, J. Qiu, ACS Appl. Mater. Interfaces 11 (2019) 9904–9910.
[57] S. Chen, W.-H. Li, W. Jiang, J. Yang, J. Zhu, L. Wang, H. Ou, Z. Zhuang, M. Chen, X. Sun, D. Wang, Y. Li, Angew. Chem. Int. Ed. 61 (2022) e202114450.
[58] L. Wang, X. Li, L. Hao, S. Hong, A.W. Robertson, Z. Sun, Chin. J. Catal. 43 (2022) 1049–1057.
[59] D. Feng, Z.Y. Gu, J.R. Li, H.L. Jiang, Z. Wei, H.C. Zhou, Angew. Chem. Int. Ed. 51 (2012) 10307–10310.
[60] G. RamÍRez, M. Lucero, A. Riquelme, M. Villagrán, J. Costamagna, E. Trollund, M.J. Aguirre, J. Coord. Chem. 57 (2004) 249–255.
[61] D. Behar, T. Dhanasekaran, P. Neta, C. Hosten, D. Ejeh, P. Hambright, E. Fujita, J. Phys. Chem. A 102 (1998) 2870–2877.
[62] K. Leung, I.M. Nielsen, N. Sai, C. Medforth, J.A. Shelnutt, J. Phys. Chem. A 114 (2010) 10174–10184.
[63] M.L. Sun, Y.R. Wang, W.W. He, R.L. Zhong, Q.Z. Liu, S. Xu, J.M. Xu, X.L. Han, X. Ge, S.L. Li, Small 17 (2021) 2100762.
[64] K.-Y.W. L. Feng, J. Willman, ACS Cent. Sci. 6 (2020) 353–359.
[65] H. Xu, X. Luo, J. Wang, Y. Su, X. Zhao, Y. Li, ACS Appl. Mater. Interfaces 11 (2019) 20291–20297.
[66] K.-G. Liu, Z. Sharifzadeh, F. Rouhani, M. Ghorbanloo, A. Morsali, Coord. Chem. Rev. 436 (2021), 213827.
[67] R. Abazari, S. Sanati, A. Morsali, A.M. Kirillov, A.M. Slawin, C.L. Carpenter-Warren, Inorg. Chem. 60 (2021) 2056–2067.
[68] X.-Y. Dao, X.-F. Xie, J.-H. Guo, X.-Y. Zhang, Y.-S. Kang, W.-Y. Sun, ACS Appl. Energy Mater. 3 (2020) 3946–3954.
[69] H. Dong, X. Zhang, Y. Lu, Y. Yang, Y.-P. Zhang, H.-L. Tang, F.-M. Zhang, Z.-D. Yang, X. Sun, Y. Feng, Appl. Catal. B: Environ. 276 (2020), 119173.
[70] X.J. Kong, T. He, J. Zhou, C. Zhao, T.C. Li, X.Q. Wu, K. Wang, J.R. Li, Small 17 (2021) 2005357.
[71] S. Kitagawa, Chem. Soc. Rev. 43 (2014) 5415–5418.
[72] J. Long, S. Wang, Z. Ding, S. Wang, Y. Zhou, L. Huang, X. Wang, Chem. Commun. 48 (2012) 11656–11658.
[73] H. Furukawa, K.E. Cordova, M. O'Keeffe, O.M. Yaghi, Science 341 (2013) 1230444.
[74] W.L. Queen, M.R. Hudson, E.D. Bloch, J.A. Mason, M.I. Gonzalez, J.S. Lee, D. Gygi, J.D. Howe, K. Lee, T.A. Darwish, Chem. Sci. 5 (2014) 4569–4581.
[75] Y. Izumi, Recent advances (2012–2015) in the photocatalytic conversion of carbon dioxide to fuels using solar energy: Feasibilty for a new energy, in, Advances in CO2 Capture, Sequestration, and Conversion, ACS Publications (2015) 1–46.
[76] N.-N. Zhu, X.-H. Liu, T. Li, J.-G. Ma, P. Cheng, G.-M. Yang, Inorg. Chem. 56 (2017) 3414–3420.
[77] H. Zhang, J. Wei, J. Dong, G. Liu, L. Shi, P. An, G. Zhao, J. Kong, X. Wang, X. Meng, J. Zhang, J. Ye, Angew. Chem. Int. Ed. 55 (2016) 14310–14314.
[78] A. Crake, K.C. Christoforidis, A. Kafizas, S. Zafeiratos, C. Petit, Appl. Catal. B: Environ. 210 (2017) 131–140.
[79] S. Ullah, A.M. Shariff, M.A. Bustam, A.E. Elkhalifah, G. Murshid, N. Riaz, B. Shimekit, in,, Applied Mechanics and Materials, Trans Tech Publ (2014) 870–873.
[80] M. Chen, L. Han, J. Zhou, C. Sun, C. Hu, X. Wang, Z. Su, Photo-reduction of carbon dioxide by ultra-small Ag nanoparticles doped Co-ZIF-9 under visible light, Nanotechnol. 29 (2018), 284003.
[81] Y. Wang, X. Zhang, K. Chang, Z. Zhao, J. Huang, Q. Kuang, Chem., Eur. J. 28 (2022) e202104514.
[82] K.M. Choi, D. Kim, B. Rungtaweevoranit, C.A. Trickett, J.T.D. Barmanbek, A. S. Alshammari, P. Yang, O.M. Yaghi, J. Am. Chem. Soc. 139 (2017) 356–362.
[83] Y. Jiang, Y. Yu, X. Zhang, M. Weinert, X. Song, J. Ai, L. Han, H. Fei, Angew. Chem. Int. Ed. 60 (2021) 17388–17393.
[84] S.M. Liu, Z. Zhang, X. Li, H. Jia, M. Ren, S. Liu, Adv. Mater. Interfaces 5 (2018) 1801062.
[85] X. Deng, L. Yang, H. Huang, Y. Yang, S. Feng, M. Zeng, Q. Li, D. Xu, Small 15 (2019) 1902287.
[86] F. Guo, S. Yang, Y. Liu, P. Wang, J. Huang, W.-Y. Sun, ACS Catal. 9 (2019) 8464–8470.
[87] F. Guo, Y.-P. Wei, S.-Q. Wang, X.-Y. Zhang, F.-M. Wang, W.-Y. Sun, J. Mater. Chem. A 7 (2019) 26490–26495.
[88] J. Becerra, D.-T. Nguyen, V.-N. Gopalakrishnan, T.-O. Do, ACS Appl. Energy Mater. 3 (2020) 7659–7665.
[89] Y. Han, H. Xu, Y. Su, Z.-L. Xu, K. Wang, W. Wang, J. Catal. 370 (2019) 70–78.
[90] L. Chen, Y. Wang, F. Yu, X. Shen, C. Duan, J. Mater. Chem. A 7 (2019) 11355–11361.
[91] D. Sun, W. Liu, Y. Fu, Z. Fang, F. Sun, X. Fu, Y. Zhang, Z. Li, Chem., Eur. J. 20 (2014) 4780–4788.
[92] G. Wang, C.-T. He, R. Huang, J. Mao, D. Wang, Y. Li, J. Am. Chem. Soc. 142 (2020) 19339–19345.
[93] Y. Fu, H. Yang, R. Du, G. Tu, C. Xu, F. Zhang, M. Fan, W. Zhu, RSC Adv. 7 (2017) 42819–42825.

[94] Q. Mu, W. Zhu, X. Li, C. Zhang, Y. Su, Y. Lian, P. Qi, Z. Deng, D. Zhang, S. Wang, Appl. Catal. B: Environ. 262 (2020), 118144.
[95] H. Zhao, X. Yang, R. Xu, J. Li, S. Gao, R. Cao, J. Mater. Chem. A 6 (2018) 20152–20160.
[96] L. Ye, Y. Gao, S. Cao, H. Chen, Y. Yao, J. Hou, L. Sun, Appl. Catal. B: Environ. 227 (2018) 54–60.
[97] Q. Mu, Y. Su, Z. Wei, H. Sun, Y. Lian, Y. Dong, P. Qi, Z. Deng, Y. Peng, J. Catal. 397 (2021) 128–136.
[98] J.-W. Wang, L.-Z. Qiao, H.-D. Nie, H.-H. Huang, Y. Li, S. Yao, M. Liu, Z.-M. Zhang, Z.-H. Kang, T.-B. Lu, Nature Commun. 12 (2021) 1–9.
[99] Z. Jiang, X. Xu, Y. Ma, H.S. Cho, D. Ding, C. Wang, J. Wu, P. Oleynikov, M. Jia, J. Cheng, Nature 586 (2020) 549–554.
[100] S. Wang, X. Wang, Appl. Catal. B: Environ. 162 (2015) 494–500.
[101] Y. Liu, L. Deng, J. Sheng, F. Tang, K. Zeng, L. Wang, K. Liang, H. Hu, Y.-N. Liu, Appl. Surf. Sci. 498 (2019), 143899.
[102] C. Chen, T. Wu, H. Wu, H. Liu, Q. Qian, Z. Liu, G. Yang, B. Han, Chem. Sci. 9 (2018) 8890–8894.
[103] Z. Han, Y. Fu, Y. Zhang, X. Zhang, X. Meng, Z. Zhou, Z. Su, Dalton Trans. 50 (2021) 3186–3192.
[104] D. Ding, Z. Jiang, J. Jin, J. Li, D. Ji, Y. Zhang, L. Zan, J. Catal. 375 (2019) 21–31.
[105] G. Xu, H. Zhang, J. Wei, H.-X. Zhang, X. Wu, Y. Li, C. Li, J. Zhang, J. Ye, ACS Nano 12 (2018) 5333–5340.
[106] S. Wan, M. Ou, Q. Zhong, X. Wang, Chem. Eng. J. 358 (2019) 1287–1295.
[107] L.Y. Wu, Y.F. Mu, X.X. Guo, W. Zhang, Z.M. Zhang, M. Zhang, T.B. Lu, Angew. Chem. Int. Ed. 58 (2019) 9491–9495.
[108] X. Wang, Y. Su, G. Yang, G. Chai, Z. Xu, M.S. Nasir, X. Zheng, C. Wang, W. Yan, Int. J. Hyd. Energy 46 (2021) 11621–11635.
[109] X. Wang, X. Zhao, D. Zhang, G. Li, H. Li, Appl. Catal. B: Environ. 228 (2018) 47–53.
[110] J. Meng, Q. Chen, J. Lu, H. Liu, ACS Appl. Mater. Interfaces 11 (2018) 550–562.
[111] F. Yu, X. Jing, Y. Wang, M. Sun, C. Duan, Angew. Chem. Int. Ed. 60 (2021) 24849–24853.
[112] D. Wei, W. Tang, Y. Gan, X. Xu, Catal. Sci. Technol. 10 (2020) 5666–5676.
[113] Z.-C. Kong, J.-F. Liao, Y.-J. Dong, Y.-F. Xu, H.-Y. Chen, D.-B. Kuang, C.-Y. Su, ACS Energy Lett. 3 (2018) 2656–2662.
[114] M. Wang, D. Wang, Z. Li, Appl. Catal. B: Environ. 183 (2016) 47–52.
[115] M. Cabrero-Antonino, S. Remiro-Buenamañana, M. Souto, A.A. García-Valdivia, D. Choquesillo-Lazarte, S. Navalón, A. Rodriguez-Diéguez, G.M. Espallargas, H. García, Chem. Commun. 55 (2019) 10932–10935.
[116] Y. Su, Z. Zhang, H. Liu, Y. Wang, Appl. Catal.B: Environ. 200 (2017) 448–457.
[117] Y. Zhao, W. Cai, J. Chen, Y. Miao, Y. Bu, Front. Chem. 7 (2019) 789.
[118] Q. Liu, Z.-X. Low, L. Li, A. Razmjou, K. Wang, J. Yao, H. Wang, J. Mater. Chem. A 1 (2013) 11563–11569.
[119] H. Zhao, X. Wang, J. Feng, Y. Chen, X. Yang, S. Gao, R. Cao, Catal. Sci. Technol. 8 (2018) 1288–1295.
[120] S. Yan, S. Ouyang, H. Xu, M. Zhao, X. Zhang, J. Ye, J. Mater. Chem. A 4 (2016) 15126–15133.
[121] L. Shi, T. Wang, H. Zhang, K. Chang, J. Ye, Adv. Func. Mater. 25 (2015) 5360–5367.
[122] Y. Wang, W. Zhen, Y. Zeng, S. Wan, H. Guo, S. Zhang, Q. Zhong, J. Mater. Chem. A 8 (2020) 6034–6040.
[123] N. Sadeghi, S. Sharifnia, T.-O. Do, J. Mater. Chem. A 6 (2018) 18031–18035.
[124] M. Xu, C. Sun, X. Zhao, H. Jiang, H. Wang, P. Huo, Appl. Surf. Sci. 576 (2022), 151792.
[125] H. Wang, Q. Zhang, J.-J. Li, J.-Y. Zhang, Y. Liu, M. Zhou, N. Zhang, Y.-Z. Fang, Q. Ke, J. Colloid Interface Sci. 606 (2022) 1745–1757.
[126] L. Wang, Z. Zhang, Q. Han, Y. Liu, J. Zhong, J. Chen, J. Huang, H. She, Q. Wang, Appl. Surf. Sci. 584 (2022), 152645.
[127] H. Wang, D. Wu, C. Yang, H. Lu, Z. Gao, F. Xu, K. Jiang, J. CO2 Util. 34 (2019) 411–421.
[128] L. Wang, P. Jin, J. Huang, H. She, Q. Wang, ACS Sustain. Chem. Eng. 7 (2019) 15660–15670.
[129] P. Nagababu, Y.T. Prabhu, A. Kularkar, M. Subbalakshmi, J. Nagarkar, S. Rayalu, Emergent Mater. 4 (2021) 503–514.
[130] Y. Ma, Q. Tang, W.-Y. Sun, Z.-Y. Yao, W. Zhu, T. Li, J. Wang, Appl. Catal. B: Environ. 270 (2020), 118856.
[131] A. Shariati, Sol. Energy 186 (2019) 166–174.
[132] R. Li, J. Hu, M. Deng, H. Wang, X. Wang, Y. Hu, H.L. Jiang, J. Jiang, Q. Zhang, Y. Xie, Adv. Mater. 26 (2014) 4783–4788.
[133] W.-W. Dong, J. Jia, Y. Wang, J.-R. An, O.-Y. Yang, X.-J. Gao, Y.-L. Liu, J. Zhao, D.-S. Li, Chem. Eng. J. 438 (2022), 135622.
[134] H. Wu, X.Y. Kong, X. Wen, S.P. Chai, E.C. Lovell, J. Tang, Y.H. Ng, Angew. Chem. Int. Ed. 60 (2021) 8455–8459.
[135] S. Xiao, Y. Guan, H. Shang, H. Li, Z. Tian, S. Liu, W. Chen, J. Yang, J. CO2 Util. 55 (2022), 101806.
[136] A. Zhou, Y. Dou, C. Zhao, J. Zhou, X.-Q. Wu, J.-R. Li, Appl. Catal. B: Environ. 264 (2020), 118519.
[137] T. Butburee, Z. Sun, A. Centeno, F. Xie, Z. Zhao, D. Wu, P. Peerakiatkhajohn, S. Thaweesak, H. Wang, L. Wang, Nano Energy 62 (2019) 426–433.
[138] S.-Q. Wang, X.-Y. Zhang, X.-Y. Dao, X.-M. Cheng, W.-Y. Sun, ACS Appl. Nano Mater. 3 (2020) 10437–10445.
[139] X. He, W.-N. Wang, J. Mater. Chem. A 6 (2018) 932–940.
[140] L. Wang, P. Jin, S. Duan, H. She, J. Huang, Q. Wang, Sci. Bull. 64 (2019) 926–933.
[141] N. Zhang, J.-J. Li, Y. Li, H. Wang, J.-Y. Zhang, Y. Liu, Y.-Z. Fang, Z. Liu, M. Zhou, J. Colloid Interface Sci. 608 (2022) 3192–3203.
[142] R. Cheng, E. Debroye, J. Hofkens, M.B. Roeffaers, Catalysts 10 (2020) 1352.
[143] E. Chamanehpour, M.H. Sayadi, M. Hajiani, Adv. Compos. Hyb. Mater. (2022) 1–17.
[144] R.R. Ikreedeegh, M. Tahir, J. Environ. Chem. Eng. 9 (2021), 105600.
[145] N. Li, X. Liu, J. Zhou, W. Chen, M. Liu, Chem. Eng. J. 399 (2020), 125782.
[146] Q. Chen, S. Li, H. Xu, G. Wang, Y. Qu, P. Zhu, D. Wang, Chin. J. Catal. 41 (2020) 514–523.
[147] S. Wang, J. Lin, X. Wang, Phys. Chem. Chem. Phys. 16 (2014) 14656–14660.
[148] Y. Wang, L. Guo, Y. Zeng, H. Guo, S. Wan, M. Ou, S. Zhang, Q. Zhong, ACS Appl. Mater. Interfaces 11 (2019) 30673–30681.
[149] S. Liu, F. Chen, S. Li, X. Peng, Y. Xiong, Appl. Catal. B: Environ. 211 (2017) 1–10.
[150] C. Zheng, X. Qiu, J. Han, Y. Wu, S. Liu, ACS Appl. Mater. Interfaces 11 (2019) 42243–42249.
[151] K. Sonowal, N. Nandal, P. Basyach, L. Kalita, S.L. Jain, L. Saikia, J. CO2 Util. 57 (2022), 101905.
[152] X. Wang, G. Yang, G. Chai, M.S. Nasir, S. Wang, X. Zheng, C. Wang, W. Yan, Int. J. Hyd. Energy 45 (2020) 30634–30646.
[153] L. Zhang, T. Xu, X. Zhao, Y. Zhu, Appl. Catal. B: Environ. 98 (2010) 138–146.
[154] Y. Meng, L. Zhang, H. Jiu, Q. Zhang, H. Zhang, W. Ren, Y. Sun, D. Li, Mater. Sci. Semicond. Process. 95 (2019) 35–41.
[155] S. Wang, M. Cabrero-Antonino, S. Navalón, C.-C. Cao, A. Tissot, I. Dovgaliuk, J. Marrot, C. Martineau-Corcos, L. Yu, H. Wang, Chem 6 (2020) 3409–3427.
[156] H.-Z. Liu, X. Liu, B. Li, H. Luo, J.-G. Ma, P. Cheng, ACS Appl. Mater. Interfaces 14 (2022) 28123–28132.
[157] E. Pipelzadeh, V. Rudolph, G. Hanson, C. Noble, L. Wang, Appl. Catal. B: Environ. 218 (2017) 672–678.
[158] Z. Huang, P. Dong, Y. Zhang, X. Nie, X. Wang, X. Zhang, J. CO2 Util. 24 (2018) 369–375.
[159] B. Di Credico, M. Redaelli, M. Bellardita, M. Calamante, C. Cepek, E. Cobani, M. D'Arienzo, C. Evangelisti, M. Marelli, M. Moret, Catalysts 8 (2018) 353.
[160] X. He, Z. Gan, S. Fisenko, D. Wang, H.M. El-Kaderi, W.-N. Wang, ACS Appl. Mater. Interfaces 9 (2017) 9688–9698.
[161] A. Crake, K.C. Christoforidis, A. Gregg, B. Moss, A. Kafizas, C. Petit, Small 15 (2019) 1805473.
[162] Q.-C. Shang, X.-Z. Fang, H.-L. Jiang, Q. Zhang, Chin. J. Chem. Phys. 31 (2018) 613.
[163] J.W. Maina, J.r.A. Schütz, L. Grundy, E. Des Ligneris, Z. Yi, L. Kong, C. Pozo-Gonzalo, M. Ionescu, L.F. Dumée,, ACS Appl. Mater. Interfaces 9 (2017) 35010–35017.
[164] M.I. Ostad, M.N. Shahrak, F. Galli, J. CO2 Util. 43 (2021), 101373.
[165] J.D. Yi, D.H. Si, R. Xie, Q. Yin, M.D. Zhang, Q. Wu, G.L. Chai, Y.B. Huang, R. Cao, Angew. Chem. Int. Ed. 60 (2021) 17108–17114.
[166] S. Xie, Y. Li, B. Sheng, W. Zhang, W. Wang, C. Chen, J. Li, H. Sheng, J. Zhao, Appl. Catal. B: Environ. 310 (2022), 121320.
[167] S. Li, T. Zhu, L. Dong, M. Dong, New J. Chem. 42 (2018) 17644–17651.
[168] J.O. Olowoyo, U. Saini, M. Kumar, H. Valdés, H. Singh, M.O. Omorogie, J. O. Babalola, A.V. Vorontsov, U. Kumar, P.G. Smirniotis, J. CO2 Util. 42 (2020), 101300.
[169] P.M. Stanley, C. Thomas, E. Thyrhaug, A. Urstoeger, M. Schuster, J.r. Hauer, B. Rieger, J. Warnan, R.A. Fischer,, ACS Catal. 11 (2021) 871–882.
[170] W. Zhu, C. Zhang, Q. Li, L. Xiong, R. Chen, X. Wan, Z. Wang, W. Chen, Z. Deng, Y. Peng, Appl. Catal. B: Environ. 238 (2018) 339–345.
[171] X. Feng, Y. Pi, Y. Song, C. Brzezinski, Z. Xu, Z. Li, W. Lin, J. Am. Chem. Soc. 142 (2020) 690–695.
[172] X. Wang, F.M. Wisser, J. Canivet, M. Fontecave, C. Mellot-Draznieks, ChemSusChem 11 (2018) 3315–3322.
[173] P.M. Stanley, J. Haimerl, C. Thomas, A. Urstoeger, M. Schuster, N.B. Shustova, A. Casini, B. Rieger, J. Warnan, R.A. Fischer, Angew. Chem. Int. Ed. 60 (2021) 17854–17860.
[174] D.C. Liu, T. Ouyang, R. Xiao, W.J. Liu, D.C. Zhong, Z. Xu, T.B. Lu, ChemSusChem 12 (2019) 2166–2170.
[175] S. Wang, W. Yao, J. Lin, Z. Ding, X. Wang, Angew. Chem. Int. Ed. 53 (2014) 1034–1038.
[176] M. Wang, J. Liu, C. Guo, X. Gao, C. Gong, Y. Wang, B. Liu, X. Li, G.G. Gurzadyan, L. Sun, J. Mater. Chem. A 6 (2018) 4768–4775.
[177] Z.-Y. Chen, Q.-L. Hong, H.-X. Zhang, J. Zhang, ACS Appl. Energy Mater. 5 (2021) 1175–1182.
[178] N.-Y. Huang, H. He, S. Liu, H.-L. Zhu, Y.-J. Li, J. Xu, J.-R. Huang, X. Wang, P.-Q. Liao, X.-M. Chen, J. Am. Chem. Soc. 143 (2021) 17424–17430.
[179] Y. Benseghir, A. Lemarchand, M. Duguet, P. Mialane, M. Gomez-Mingot, C. Roch-Marchal, T. Pino, M.-H. Ha-Thi, M. Haouas, M. Fontecave, J. Am. Chem. Soc. 142 (2020) 9428–9438.
[180] K. Zhang, S. Goswami, H. Noh, Z. Lu, T. Sheridan, J. Duan, W. Dong, J.T. Hupp, J. Photochem. Photobiol. 10 (2022), 100111.
[181] Z.-H. Yan, B. Ma, S.-R. Li, J. Liu, R. Chen, M.-H. Du, S. Jin, G.-L. Zhuang, L.-S. Long, X.-J. Kong, Sci. Bull. 64 (2019) 976–985.
[182] T. Kajiwara, M. Fujii, M. Tsujimoto, K. Kobayashi, M. Higuchi, K. Tanaka, S. Kitagawa, Angew. Chem. Int. Ed. 55 (2016) 2697–2700.
[183] D. Sun, Y. Gao, J. Fu, X. Zeng, Z. Chen, Z. Li, Chem. Commun. 51 (2015) 2645–2648.
[184] H. Fei, M.D. Sampson, Y. Lee, C.P. Kubiak, S.M. Cohen, Inorg. Chem. 54 (2015) 6821–6828.
[185] Y. Ma, J. Du, Y. Fang, X. Wang, ChemSusChem 14 (2021) 946–951.
[186] Y.-C. Hao, L.-W. Chen, J. Li, Y. Guo, X. Su, M. Shu, Q. Zhang, W.-Y. Gao, S. Li, Z.-L. Yu, L. Gu, X. Feng, A-X. Yin, R. Si, Y-W. Zhang, B. Wang, C-H. Yan, Nature Commun 12 (2021) 2682.

[187] J. Bi, L. Wu, Y. Zhang, Z. Li, J. Li, X. Fu, Appl. Catal. B: Environ. 91 (2009) 135–143.
[188] W. Cai, X. Yu, Y. Cao, C. Hu, Y. Wang, Y. Zhao, Y. Bu, J. Environ. Chem. Eng. 10 (2022), 107461.
[189] S. Goyal, M.S. Shaharun, C.F. Kait, B. Abdullah, M. Ameen, Catalysts 8 (2018) 581.
[190] S. Payra, S. Ray, R. Sharma, K. Tarafder, P. Mohanty, S. Roy, Inorg. Chem. 61 (2022) 2476–2489.
[191] N. Nandal, P.K. Prajapati, B.M. Abraham, S.L. Jain, Electrochim. Acta 404 (2022), 139612.
[192] J. Cheng, X. Yang, X. Xuan, J. Zhou, Chem. Eng. J. 392 (2020), 123799.
[193] J. Cardoso, S. Stulp, J. De Brito, J. Flor, R. Frem, M. Zanoni, Appl. Catal. B: Environ. 225 (2018) 563–573.
[194] B. Rungtaweevoranit, J. Baek, J.R. Araujo, B.S. Archanjo, K.M. Choi, O.M. Yaghi, G.A. Somorjai, Nano Lett. 16 (2016) 7645–7649.
[195] W. Zhang, L. Wang, K. Wang, M.U. Khan, M. Wang, H. Li, J. Zeng, Small 13 (2017) 1602583.
[196] K. Mori, A. Konishi, H. Yamashita, J. Phys. Chem. C 124 (2020) 11499–11505.
[197] M. Wen, K. Mori, Y. Futamura, Y. Kuwahara, M. Navlani-García, T. An, H. Yamashita, Sci. Rep. 9 (2019) 15675.
[198] K. Yang, J. Jiang, ACS Appl. Mater. Interfaces 13 (2021) 58723–58736.
[199] B. An, J. Zhang, K. Cheng, P. Ji, C. Wang, W. Lin, J. Am. Chem. Soc. 139 (2017) 3834–3840.
[200] N.T.T. Van, L.C. Loc, N. Tri, H.T. Cuong, Int. J. Nanotechnol. 12 (2015) 405–415.
[201] W. Zhen, B. Li, G. Lu, J. Ma, Chem. Commun. 51 (2015) 1728–1731.
[202] W. Zhen, F. Gao, B. Tian, P. Ding, Y. Deng, Z. Li, H. Gao, G. Lu, J. Catal. 348 (2017) 200–211.
[203] Z.-W. Zhao, X. Zhou, Y.-N. Liu, C.-C. Shen, C.-Z. Yuan, Y.-F. Jiang, S.-J. Zhao, L.-B. Ma, T.-Y. Cheang, A.-W. Xu, Catal. Sci. Technol. 8 (2018) 3160–3165.
[204] H. Chen, Y. Mu, Y. Shao, S. Chansai, H. Xiang, Y. Jiao, C. Hardacre, X. Fan, AIChE J. 66 (2020) e16853.
[205] O. Grad, M. Mihet, G. Blanita, M. Dan, L. Barbu-Tudoran, M.D. Lazar, Catal. Today 366 (2021) 114–122.
[206] M. Mihet, O. Grad, G. Blanita, T. Radu, M.D. Lazar, Int. J. Hyd. Energy 44 (2019) 13383–13396.
[207] X. Hu, M. Luo, M. ur Rehman, J. Sun, H.A. Yaseen, F. Irshad, Y. Zhao, S. Wang, X. Ma,, J. CO2 Util. 60 (2022), 101992.
[208] P. Tshuma, B.C. Makhubela, L. Öhrström, S.A. Bourne, N. Chatterjee, I.N. Beas, J. Darkwa, G. Mehlana, RSC Adv. 10 (2020) 3593–3605.
[209] S. Wang, S. Hou, C. Wu, Y. Zhao, X. Ma, Chin. Chem. Lett. 30 (2019) 398–402.
[210] Z. Li, T.M. Rayder, L. Luo, J.A. Byers, C.-K. Tsung, J. Am. Chem. Soc. 140 (2018) 8082–8085.
[211] C. Wu, F. Irshad, M. Luo, Y. Zhao, X. Ma, S. Wang, ChemCatChem 11 (2019) 1256–1263.
[212] X. Weiwei, X. Zhang, D. Mengyue, Z. Jing, D. Lanbo, Plasma Sci. Technol. 21 (2019), 044004.
[213] X. Cui, S. Shyshkanov, T.N. Nguyen, A. Chidambaram, Z. Fei, K.C. Stylianou, P. J. Dyson, Angew. Chem. Int. Ed. 59 (2020) 16371–16375.
[214] L. Li, X. Pan, D. Lan, H. Xu, J. Ge, H. Zhang, Z. Zheng, J. Liu, Z. Xu, J. Liu, Mater. Today Energy 19 (2021), 100585.
[215] L.L. Ling, W. Yang, P. Yan, M. Wang, H.L. Jiang, Angew. Chem. Int. Ed. 61 (2022) e202116396.
[216] E.S. Gutterød, A. Lazzarini, T. Fjermestad, G. Kaur, M. Manzoli, S. Bordiga, S. Svelle, K.P. Lillerud, E. Skúlason, S. Øien-Ødegaard, J. Am. Chem. Soc. 142 (2019) 999–1009.
[217] N. Makuve, J. Darkwa, G. Mehlana, B.C. Makhubela, Inorganics 10 (2022) 30.
[218] H. Jiang, Q. Gao, S. Wang, Y. Chen, M. Zhang, J. CO2 Util. 31 (2019) 167–172.
[219] P. Tshuma, B.C. Makhubela, N. Bingwa, G. Mehlana, Inorg. Chem. 59 (2020) 6717–6728.
[220] H. Zhang, H. Xu, Y. Li, Y. Su, Appl. Mater. Today 19 (2020), 100609.
[221] M. Stawowy, R. Ciesielski, T. Maniecki, K. Matus, R. Łużny, J. Trawczynski, J. Silvestre-Albero, A. Łamacz, Catalysts 10 (2019) 39.
[222] H. Kobayashi, J.M. Taylor, Y. Mitsuka, N. Ogiwara, T. Yamamoto, T. Toriyama, S. Matsumura, H. Kitagawa, Chem. Sci. 10 (2019) 3289–3294.
[223] Y. Mitsuka, N. Ogiwara, M. Mukoyoshi, H. Kitagawa, T. Yamamoto, T. Toriyama, S. Matsumura, M. Haneda, S. Kawaguchi, Y. Kubota, Angew. Chem. Int. Ed. 60 (2021) 22283–22288.
[224] L. Zeng, Z. Wang, Y. Wang, J. Wang, Y. Guo, H. Hu, X. He, C. Wang, W. Lin, J. Am. Chem. Soc. 142 (2019) 75–79.
[225] Q. Jiang, D. Lan, G. Zhao, H. Xu, X. Gong, J. Liu, Y. Shi, L. Zhang, H. Fang, D. Cheng, ACS Catal. 12 (2022) 5894–5902.
[226] B. An, L. Zeng, M. Jia, Z. Li, Z. Lin, Y. Song, Y. Zhou, J. Cheng, C. Wang, W. Lin, J. Am. Chem. Soc. 139 (2017) 17747–17750.
[227] J. Zhang, B. An, Y. Cao, Z. Li, J. Chen, X. He, C. Wang, ACS Appl. Energy Mater. 4 (2021) 13567–13574.
[228] X. Li, G. Liu, D. Xu, X. Hong, S.C.E. Tsang, J. Mater. Chem. A 7 (2019) 23878–23885.
[229] A. Tarasov, V. Isaeva, O. Tkachenko, V. Chernyshev, L. Kustov, Fuel Process. Technol. 176 (2018) 101–106.